UNIVERSIDAD NACIONAL AUTÓNOMA DE MÉXICO

PROGRAMA DE MAESTRÍA Y DOCTORADO EN INGENIERÍA
INGENIERÍA ELÉCTRICA – SISTEMAS ELÉCTRICOS DE POTENCIA

ESTIMACIÓN DE ESTADO DINÁMICA DE SISTEMAS FLEXIBLES DE TRANSMISIÓN EN CORRIENTE ALTERNA

TESIS
QUE PARA OPTAR POR EL GRADO DE:
DOCTOR EN INGENIERÍA

PRESENTA:
ISAAC LEVI ORTEGA RIVERA

TUTOR PRINCIPAL
DR. CLAUDIO RUBÉN FUERTE ESQUIVEL, UMSNH

COMITÉ TUTOR
DR. GERARDO RENÉ ESPINOSA PÉREZ, FACULTAD DE INGENIERÍA, UNAM
DR. CÉSAR ANGELES CAMACHO, II-UNAM
DR. ARTURO ROMÁN MESSINA, CINVESTAV
Dr. GERALD THOMAS HEYDT, ARIZONA STATE UNIVERSITY

CIUDAD DE MÉXICO, SEPTIEMBRE 2018

UNIVERSIDAD NACIONAL AUTÓNOMA DE MÉXICO

MASTER AND DOCTORATE PROGRAM IN ENGINEERING
ELECTRIC ENGINEER – POWER ELECTRIC SYSTEMS

DYNAMIC STATE ESTIMATION OF FLEXIBLE AC TRANSMISSION SYSTEMS

DISSERTATION IN FULFILLMENT OF THE REQUIREMENTS
FOR THE DEGREE OF
DOCTOR OF PHILOSOPHY IN ENGINEERING

PRESENTED BY:
ISAAC LEVI ORTEGA RIVERA

THESIS ADVISOR
DR. CLAUDIO RUBÉN FUERTE ESQUIVEL, UMSNH

COMMITTE MEMBERS
DR. GERARDO RENÉ ESPINOSA PÉREZ, FACULTAD DE INGENIERÍA, UNAM
DR. CÉSAR ANGELES CAMACHO, II-UNAM
DR. ARTURO ROMÁN MESSINA, CINVESTAV
Dr. GERALD THOMAS HEYDT, ARIZONA STATE UNIVERSITY

MEXICO CITY, MEXICO. SEPTEMBER 2018

C O M M I T T E M E M B E R S :

President:	Dr. GERARDO RENE ESPINOSA PEREZ
Secretary:	Dr. CESAR ANGELES CAMACHO
1st vocal:	Dr. CLAUDIO RUBÉN FUERTE ESQUIVEL
2nd vocal:	Dr. ARTURO ROMAN MESSINA
3rd vocal:	Dr. GERALD THOMAS HEYDT

This dissertation was made in the Engineering Institute, UNAM.

THESIS ADVISOR:

Dr. Claudio Rubén Fuerte Esquivel

Signature

Abstract

The stabilizing control for inter-area power oscillations in large interconnected power systems is often accomplished by using a supplementary damping control (SDC) at the synchronous machines as well as flexible AC transmission system (FACTS) devices. The effectiveness of these controllers is based primarily on the use of appropriate remote signals. In some cases, these signals deteriorated in the presence of noise and bad data, or even worse, the signal may not be available.

This thesis proposes a novel control scheme to damp out the inter-area modes of oscillations by means of a static VARs compensator, which is assisted by an estimated wide-area signal and a local signal from a phasor measurements unit (PMU). A PMU-based tracking state estimator is employed to provide the estimated wide-area signal to a robust SDC, which uses the local signal to maintain the control function in case the communication of the estimated remote signal is lost.

The details of the procedure for obtaining the stabilizing signals candidates for the SDC as well as the formulation for obtaining the state-space representation of the power system are given. The small-signal analysis is employed to improve the damping of critical electromechanical modes. Furthermore, a strategy for obtaining an alternative control signal based on the information of the mode shape is presented.

To illustrate the feasibility of the proposed centralized control scheme, the IEEE 50-generator power system is utilized. Different noise levels in the PMUs' measurements, a large disturbance, and several operating conditions, as well as the execution time of the estimator, are analyzed through time-domain simulations to evaluate the proposed concept.

In addition to the test bed system, the Mexican interconnected system is analyzed in this work; furthermore, the proposed method is employed to damp out the power oscillations by exploiting the capacity of installed SVCs.

Resumen

El control de estabilización para las oscilaciones de potencia inter-área presentes en grandes sistemas eléctricos de potencia interconectados, a menudo se lleva a cabo utilizando un control suplementario (SDC por sus siglas en inglés) en las máquinas síncronas, y con el uso de los dispositivos de sistemas flexibles de transmisión en corriente alterna (FACTS). La efectividad de estos controladores se basa principalmente en el uso de señales remotas apropiadas. En algunos casos, estas señales pueden corromperse por la presencia de ruido y datos erróneos, o peor aún, la señal puede no estar disponible.

Esta tesis propone un novedoso esquema de control para amortiguar los modos de oscilación inter-área por medio de un compensador estático de Var, el cual es asistido por una señal estimada de área amplia, y una señal local proveniente de una unidad de medición fasorial (PMU). Se utiliza un estimador de rastreo basado en PMUs para proporcionar la señal estimada a un SDC robusto, el cual utiliza la señal local para mantener la función de control en caso de que se pierda la comunicación de la señal remota estimada.

Se proporcionan los detalles del procedimiento para obtener señales de estabilización candidatas para el SDC, así como la formulación para obtener la representación en el espacio de estados del sistema de potencia. El análisis de señal pequeña se emplea para evaluar la mejora del amortiguamiento de los modos electromecánicos críticos utilizando el método propuesto. Además, se presenta una estrategia para obtener una señal de control alternativa basada en la información de la forma de modo.

Para ilustrar la viabilidad del esquema de control centralizado propuesto, se utiliza el sistema IEEE 50-generadores. Diferentes niveles de ruido en las mediciones PMUs, grandes perturbaciones, y varias condiciones de operación, así como el tiempo de ejecución del estimador, se analizan a través de simulaciones en el dominio del tiempo para evaluar el concepto propuesto.

Además del sistema de pruebas se analiza el sistema mexicano interconectado, y el método propuesto se emplea para amortiguar las oscilaciones de potencia al explotar la capacidad de los SVCs instalados

Dedication

"To my wife, my children Aisha and Kaled,

my mother and brother,

my grandmother"

For their love, endless support, encouragement and sacrifices.

Acknowledgements

To Dr. Claudio Fuerte Esquivel and Dr. Cesar Angeles Camacho for their support, guidance, and friendship.

To Dr. Gerald Heydt and Dr. Vijay Vittal for allowing me to undertake part of my PhD studies at the Arizona State University in Tempe, AZ, USA.

To Dr. Gerardo René Espinosa Pérez and Dr. Arturo Roman Messina for their invaluable suggestions and supervision of my PhD studies.

Contents

List of Figures

List of Tables

Abbreviations

BDD	Bad data detector
C	Central
COI	Center of inertia
DLL	Dynamic-link library
DSE	Dynamic state estimator
EKF	Extended Kalman filter
EMS	Energy management system
FACTS	Flexible AC transmission system
FASE	Forecasting-aided state estimator
GPS	Global Positioning System
HSE	Hybrid state estimator
HVDC	High-voltage direct current
KF	Kalman filter
LFOs	Low-frequency oscillations
LQG	Linear quadratic Gaussian
MAE	Mean absolute error
MAPE	Mean absolute percentage error
MIS	Mexican interconnected system
N	North

NE	Northeastern
NW	Northwestern
PMU	Phasor measurement unit
PSS	Power system stabilizer
SCADA	Supervisory control and data acquisition
SDC	Supplementary damping controller
SE	State estimator
SE	Southeastern
SM	Synchronous machine
SSAT	Small-signal analysis tool
SVC	Static VAR compensator
TISO	Two-input single-output
TSAT	Transient security assessment tool
TSE	Tracking state estimator
UDM	User-defined model
UKF	Unscented Kalman filter
W	Western
WGN	White Gaussian noise
WLS	Weighted least square

Nomenclature

$\boldsymbol{A}$	State space matrix for the open-loop system
$\boldsymbol{A_D}$	Block diagonal matrix composed of $\boldsymbol{A_i}$
$\boldsymbol{A_i}$	Matrix related to the state vector of the individual device
$\boldsymbol{B}$	State space matrix for the open-loop system
$\boldsymbol{B_D}$	Matrix composed of $\boldsymbol{B_i}$
$\boldsymbol{B_i}$	Matrix related to the terminal voltages of the individual device
B_L	Unconstrained equivalent susceptance of the SVC
B_{SVC}	Equivalent admittance of the static VAR compensator
$\boldsymbol{C}$	State space matrix for the open-loop system
$\boldsymbol{C_D}$	Block diagonal matrix composed of $\boldsymbol{C_i}$
$\boldsymbol{C_i}$	Matrix related to the state vector of the individual device for the injection current expression
E_{fd}	Constrained excitation voltage
E'_{qi}, E'_{di}	Direct axis and quadrature axis transient electromagnetic fields of the ith generator
$\boldsymbol{F}_{k-1}, \boldsymbol{g}_{k-1}$	Matrices for calculating predicted state vector
$\boldsymbol{H}_k$	Jacobian matrix of the measurements models
$\boldsymbol{h}_k$	Vector of measurement models
H_i	Inertia constant of the ith generator
$\boldsymbol{i}$	Vector of device terminals currents

i_d, i_q	Currents in the d- and q- axis of the ith device
I_{Di}, I_{Qi}	Direct axis and quadrature axis current injection of bus i with respect to the network reference frame
θ_I	Phase angle of the branch current phasor provided by the PMU
$I_{PMU\ k\text{-}m}$	Magnitude of the branch current phasor between buses k and m
$\boldsymbol{K}_k$	Gain matrix
K_{di}	Damping coefficient of the ith generator
K_{SVC}	Regulator gain of the SVC
m	Number of generators represented by the two-axis model
n	Number of generators
$\boldsymbol{P}_k$	Covariance matrix of the state vector
$\boldsymbol{P}_k^-$	Covariance matrix of the predicted state vector
$\boldsymbol{Q}_{k-1}$	Covariance matrix of the dynamic model of the system
Q_C	The maximum reactive power the SVC could produce
Q_L	The maximum reactive power the SVC could absorb
$\boldsymbol{R}_k$	Covariance matrix of measurements
r_a	Stator resistance of synchronous generator
t	Time
$T_1 \ldots T_5$	Time constants in the lead-lag blocks of the SVC
T'_{d0i}, T'_{q0i}	Open-circuit direct and quadrature axis transient time constants
$T_{e\mathrm{i}}$	Air-gap torque of the ith generator
T_{mi}	Mechanical torque of the ith generator
T_s	Time step
u	Control signals in a power system network
$\boldsymbol{v}$	Vector of device terminals voltages

v_{di}, v_{qi}	Projection of the ith generator terminal voltage on the synchronous reference frame d- and q- axis
V_{Di}, V_{Qi}	Direct and quadrature axis voltage of bus i in the network reference frame
V_{PMU}	Magnitude of bus voltage phasor provided by the PMU
V_{ref}	Reference voltage
V_{si}	Constrained output voltage of the PSS
V_{sup}	Constrained output of the SDC
V_{svc}	Voltage magnitude of the static VAR compensator
V_t	Terminal voltage of the ith generator
w_k	Vector of model's errors
$\boldsymbol{x}$	State vector
x_{di}, x_{qi}	Direct and quadrature axis synchronous reactance
x'_{di} , x'_{qi}	Direct and quadrature axis transient reactance
X_{E1i}, X_{E2i}, E_{Li}	State variables of the excitation system for the ith generator
$\boldsymbol{x}_m^{g1}$	State vector of the mth generator represented by the two-axis model
$\boldsymbol{x}_{(n-m)}^{g2}$	State vector of the $(m\text{-}n)$th generator represented by the classical model
$\tilde{\boldsymbol{x}}_k$	predicted state vector of the system
X_{p1i}, X_{p2i}, X_{p3i}	State variables of the PSS for the ith generator
X_{s1}, X_{s2}	State variables for representing the SVC
$\boldsymbol{x}^{SVC}$	State vector of the SVC
$\hat{\boldsymbol{x}}_k$	Estimated state vector
$\boldsymbol{Y_D}$	Matrix composed of $\boldsymbol{Y_i}$
$\boldsymbol{Y_i}$	Matrix related to the voltage of the individual device for the injection current expression
$\boldsymbol{Y_N}$	Nodal admittance matrix of the reduced network

$\boldsymbol{z_k}$	Vector of PMU measurements
α, β	Parameters of the Holt's exponential method
δ_i	Rotor angle of *i*th generator
$\boldsymbol{\varepsilon}_k$	Vector of measurements' errors
σ	Standard deviation
$\lambda_{k,i}$	Innovation process for the *i*th measurement
$\lambda_{\max,i}$	Threshold value for the *i*th measurement in the bad data detector
I_{PMU}	Magnitude of the phasor of current provided by the PMU
$I_{branch,r}$, $I_{branchir}$	Rectangular components of the branch current phasor provided by the PMU
θ_{PMU}	Phase angle of bus voltage phasor provided by the PMU
$\Delta\omega$	Rotor speed deviation of the *i*th generator

Chapter 1

Introduction

1.1 Overview of power oscillations in power systems

The synchronous machine (SM) is one of the major components of power systems since it is the element responsible for maintaining the energy balance by satisfying the electric demand as well as the losses. At steady-state operation, the SM interconnected to the system are in synchronism: their rotors' angular velocity is constant at a rated frequency (60 Hz in North America). When a small perturbation occurs, such as a variation between load and generation, the angular velocity and the rotor angle of the machines are modified. Consequently, the rotor masses accelerate or decelerate in order to reach a new equilibrium and finally to hold their speed constant; otherwise, the system becomes unstable. These changes in the rotor angle of machines appear as power oscillations in a power system. Because of the electromechanical nature, these oscillations are also known as low-frequency oscillations (LFOs), and they lie in the range 0.1-2.0 Hz.

Commonly, LFOs experienced in power systems are classified as (i) Local and (ii) inter-area [1]. The first ones are within the frequency interval of 0.8-1.5 Hz and represent the oscillation of a generator against the rest of the system, while the second ones are within 0.2-0.7 Hz and involve large geographical zones, where the oscillations involve two coherent groups of generators located at different geographic areas. These power oscillations can affect system components and trigger some protections, which may result in cascading events

leading to a blackout[2]. The causes of this phenomenon have been extensively studied in [3], [4], [1], [5]. Factors, however, such as the incorporation of non-conventional energy sources, increasing electrical energy demands coupled with limited investment in transmission infrastructure, and energy market deregulation have pushed power system to operate closer to their stability limits [6], [7]. In this sense, the inter-area modes have become a source of concern in today's energy management system (EMS). Appropriate damping of these oscillations is a prerequisite in securing the operation of the system.

1.2 Research motivation

Traditionally, the use of a supplementary damping controller (SDC) or a power system stabilizer (PSS) is the first measure in enhancing small-signal stability by mitigating LFOs. Adequate control of local plant mode oscillations can be readily achieved by using PSSs to modulate generator excitation controls [8]. Controls based on local signals, however, may not always be effective in damping inter-area mode because of the lack of observability of the system modal characteristics. In such cases, remote signals are employed [9]; however, the time delay in data communication can have a negative impact on the efficiency of the control mechanism [10]. Furthermore, sometimes this required remote signal is not available, or the signal quality can degrade the performance of damping controllers [11].

Currently, with the development and placement of the phasor measurement units (PMUs) in power systems, data can be available at a high sampling rate with high speed communication channels. The typical PMU sample rate of 30 to 120 samples per second has allowed capturing the dynamics of electromechanical oscillations in near real time. These technological advantages have paved the way for new monitoring and control applications in the EMS [12], [13]. The essential part of these control schemes is based on wide-area or remote signals to deal with the critical LFOs.

In the literature, the dynamic state estimation (DSE) method based on PMUs has been utilized to ensure the required signals. In other words, the dynamic states of the SM as a rotor angle or rotor speed deviation are estimated. In [14], the DSE with the Kalman filter (KF) theory is applied to one generator in order to damp the local modes by using an estimated

signal for the SDC of a static VAR compensator (SVC) connected in the infinite bus system. The rotor speed deviation is calculated

The algorithm proposed in [15] by Ghahremani and Kamwa is utilized in a multi-machine system. The inter-area mode is mitigated by the coordination of local PSSs with wide-area PSS controllers. This approach requires applying the DSE to the remote generators to obtain the control signals; the damping control is tested on the Kundur four-machine system at one operation condition. A centralized control scheme to enhance the small-signal stability of a large-scale system may need a fast and robust communication network. In this case, a decentralized linear quadratic Gaussian (LQG) technique is proposed in [16]: the DSE method and the linear quadratic regulator for optimal control are applied to those controllable generators using local measurements.

The control for inter-area oscillations of the above approaches is accomplished through an excitation system of generators. In the industry, some of the installed PSSs are already tuned for local modes or specific operating conditions [17]. Thus, the SDCs required may not be available or modified.

Flexible AC transmission system (FACTS) controllers can be used to damp out the power oscillations. In addition to controlling the power flow at steady state, the appropriate tuning of the way in which high power electronics' components of these devices operate and of the control laws used in these controllers allows improving the transient stability [18], [19]. In this context, the SDC is designed to extend the damping afforded by the PSSs of SMs. In practice, critical inter-area modes must be controllable for the location of FACTS controllers. Because of the significative cost of these flexible systems, at the planning stage they are also optimally placed in the network to exploit their versatility for performing specific control actions [20].

In the global context, the oscillatory stability issue in a power system is related to the voltage stability problem [21]. In this sense, FACTS devices provide a recommended solution. For instance, the SVC can increase the system's loadability by locally controlling the voltage magnitude at a specified bus and at the same time contributes to the system's

power oscillation damping, while the PSS controller does not play a significant role in the integral solution of these two problems.

A common solution adopted by operators in EMS to solve the LFOs identified in long transmission corridors during peak demand consists of reducing the active power flows through these corridors by using a remedial action scheme. Currently, utility companies take advantage of the FACTS controllers installed in their transmission networks, as the ones employed by the Bonneville Power Administration [22], [23], USA. By way of example, the high-voltage direct current (HVDC) device enhances the small-signal stability by modulating the power flow on the 850-mile DC transmission line. Since the SDC use wide-area signals from PMUs located in remote areas, a built-in supervisory system verifies the integrity of these remote data as well as their time delay.

Based on the information mentioned above, the motivation for this research lies on the way in which power oscillations in large-scale power systems can be damped by an SVC that uses remote control signals supplied by a PMU-based state estimator. For such a purpose, a tracking state estimation method, based on a KF technique for nonlinear systems, is utilized to obtain and ensure the stabilizing control signal in real-time for a robust SDC that considers the time delay associated with the communication data for this remote signal. This new control scheme tackles the small-signal stability and the state estimation method for power systems. Thus, eigenanalysis and time domain simulations are carried out to evaluate the proposal under different operating conditions and fault locations, as well as the high level of noise for the measurements.

1.3 Research objectives

The general objective of this research is to develop a SVC's control scheme that uses remote PMU measurements provided by a state estimator to damp out power oscillations in electric power systems.

The specific objectives of the dissertation are stated as follows.

- To analyze the electromechanical modes of a large-scale system with an SVC installed to find optimal control input signals for the robust SDC associated with FACTS device.
- To develop a tracking state estimator based on PMUs in order to obtain bus voltage phasors or algebraic variables of the system in real-time.
- To establish the framework for the system damping enhancement by using the estimated signals as feedback in the SDC for SVC connected in the multi-machine system.
- To validate the performance of the proposal applied to a test-bed under different operating conditions by means of time domain simulations.
- To evaluate the proposed method as a feasible tool for real-time application.

1.4 Contributions

The main contributions of this dissertation are listed as follows.

1. The proposed solution for the large-scale power system is implemented in an SVC and derives the wide-area control input using the estimator in a robust SDC.
2. The controller does not require any modification in the PSS settings.
3. Communication failures and transmission delay for the stabilizing signal from the estimator are taken into account in the robust controller employed.
4. An alternative control signal to the required remote signal can be obtained in order to improve the LFOs damping.

1.5 Methodology

The following research methodology has been adopted to achieve the objectives set for this research work.

1. To develop mathematical models of a power system with an SVC installed, as its linearized representation in the state-space form.

2. To apply a small-signal analysis to the linearized system to calculate the critical oscillatory modes for several operating conditions.
3. To identify candidate wide-area control signals for the damping controller by means of the controllability-observability characteristics of the model. The two-input single-output (TISO) damping controller proposed in [24] is utilized for the FACTS device engaged in this proposal.
4. To develop the estimation method based on PMUs in order to estimate the system's state (bus voltage magnitudes and phase angles) in real-time. Consequently, to provide control signals composed of the estimated algebraic state variables. The extended Kalman filter (EKF) formulation with bad data detection is utilized in the estimator.
5. To apply a modal study to the closed-loop system through the use of a small-signal analysis tool (SSAT) program to evaluate the appropriate dynamic interaction between the SDC and controllers of SMs. According to the information about critical electromechanical modes, an alternative stabilizing signal is established.
6. To assess and validate the proposed method on a large-scale system via time domain simulations with a transient security assessment tool (TSAT) program. Because of the linear approaches utilized, different scenarios are defined that encompass the following key aspects: damping effectiveness under several operating conditions associated with the location of the disturbance, and the impact of high levels of noise in PMUs considering the correlated noise effect.
7. To compare the results between the proposed control-scheme and the conventional solution employed for LFOs.

1.6 Thesis outline

The remainder of this thesis is organized into five Chapters. A brief overview of each one is giving below.

Chapter 2 describes the mathematical foundation for performing the small-signal analysis. In addition, the IEEE 50-generator system is introduced as the test-bed for this

research. Thus, the electric power system's modeling and the method for the selection of the stabilizing signals for the utilized SDC is presented in this chapter.

Chapter 3 details the mathematical formulation of TSE based on PMUs. The EKF algorithm with bad data identification is applied to the test-bed system. The prerequisites and assumptions to accomplish the estimation process are listed in this chapter. Furthermore, this section highlight key features when dynamic state estimation (DSE) or TSE methods are used as potential applications to assist the damping controllers.

Chapter 4 presents the results of the novel control scheme applied to the test-bed. Hence, in this chapter, several studies cases are set up to assess the proposal through time domain simulations.

Chapter 5 gives the general conclusions of this research and makes suggestions regarding those topics that require further investigation.

1.7 Research visits

A research visit to Engineering Research Center at Arizona State University (ASU) was conducted during this dissertation, under the supervision of Professors Gerald Heydt and Vijay Vittal.

1.8 Publications

As a result of this research, the following international conference paper and journal paper have been published.

I. I. L. Ortega Rivera, V. Vittal, G. T. Heydt, C. R. Fuerte-Esquivel, and C. Angeles-Camacho, “A Dynamic State Estimator Based Control for Power System Damping,” IEEE Trans. Power Syst., vol., pp. 1–1, 2018. (early access) DOI: 10.1109/TPWRS.2018.2825301

II. I. L. Ortega Rivera, C. R. Fuerte Esquivel, C. Angeles Camacho, G. T. Heydt, and V. Vittal, “A dynamic state estimator for the development of a control signal for power system damping enhancement,” in 2017 IEEE Power & Energy Society Innovative Smart Grid Technologies Conference (ISGT), 2017, pp. 1–5.

Chapter 2

Theoretical concepts of small-signal stability

2.1 Introduction

Electric power systems consist of various kinds of dynamic components such as generators, exciters, PSSs and FACTS devices. The mathematical models of these components must represent their nonlinear operational characteristics. In this sense, proper energy functions have been constructed to analyze the nonlinear behavior of the power system; however, the construction of these functions for large-scale systems may become a difficult task [8]. In practice, time domain-based transient stability programs are used to assess the dynamics of power systems described by a set of nonlinear differential algebraic equations.

Immediately following a small disturbance, or after the system has survived to a large disturbance and has entered a state of oscillation, the system nonlinearities do not play a major role. Under these operational scenarios, the power system can be linearized about the equilibrium point and useful information on the system's small-disturbance performance can be obtained from the linearized model. In this context, the presence of electromechanical oscillations are associated with small disturbances such as the random fluctuation of

generation and load. This fact has enabled considering if the perturbations are small enough such that the linearization of system equations is permissible for purposes of the power oscillation analysis [25]. Even though powerful analytical methods have been developed in linear control theory for the analysis of the linearized dynamic system, the state-space approach is the one used in practice because, in addition to providing all the information obtainable from other approaches, this method can handle complex systems with sufficient ease. After the linearization of the equations representing the power system dynamics around an operating point, which will retain the behavior of the system under small disturbances, their corresponding state-space form is obtained. The solution of the set of state-space equations is similarly obtained to that used for solving first-order ordinary differential equations. Furthermore, the stability of the system represented by that set of equations is determined by an eigenanalysis of the state matrix. This eigenanalysis corresponds to the small-signal stability analysis in the power systems' field [26].

On the other hand, a well-designed control system can damp out power oscillations and extend the feasible operation region in which the system remains stable under small disturbances. The stabilizing control generally is designed under a specific range of perturbations around a specified point of equilibrium.

In practical power systems, the number of dominant inter-area modes is larger than the number of control devices available [9]; furthermore, in large-scale systems adverse interactions among power system controls may occur [27]. In this context, a centralized control scheme employing wide-area signals for the SDC is utilized in this work. Besides, the complete eigenvalues of the system are computed for assessing the interaction of the dynamic devices of the power system.

2.2 Linearized state-space model of power system

The system considered in this work is composed of n generators, from which m of these are represented by the two-axis model equipped with an IEEE AC-4 exciter [28], while the remaining $(n - m)$ generators are described by the classical model [25]. As the first measure

in enhancing the small-signal stability, the IEEE standard speed-based PSS model [29] is employed for the SMs.

The SVC defined by the TSAT Type-1 model [30] is used to extend power oscillations' damping control in the system. The block diagram of this model is shown in Figure 2.1, where the modulation of the equivalent admittance of the SVC (B_{SVC}) allows the voltage control at its terminals. Note that this control is achieved by comparing the SVC reference voltage (V_{ref}) to the voltage magnitude of the SVC (V_{SVC}). For the controller purposes, the supplementary control signal V_{sup} is responsible for damping out the presence of low frequency oscillations in the system; later in this chapter, the SDC utilized in this work will be introduced in order to provide this signal.

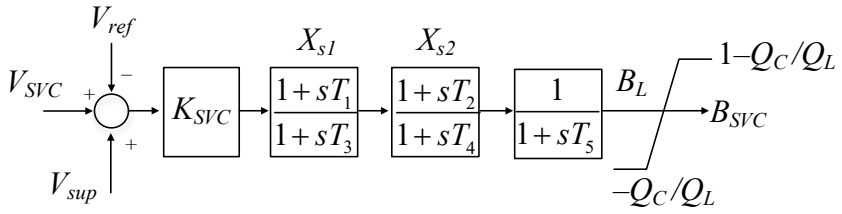

Figure 2.1 TSAT Type-1 Model for SVC

The behavior of the dynamic devices of the power system may be described by a set of first-order nonlinear ordinary differential-algebraic equations of the following form [25].

$$\dot{\boldsymbol{x}} = \boldsymbol{f}\left(\boldsymbol{x}, \boldsymbol{v}, u\right) \tag{2.1}$$

$$\boldsymbol{i} = \boldsymbol{g}\left(\boldsymbol{x}, \boldsymbol{v}\right), \tag{2.2}$$

where

$$\boldsymbol{x} = \left[\, \boldsymbol{x}_1^{g1}, \cdots, \boldsymbol{x}_m^{g1}, \boldsymbol{x}_1^{g2}, \cdots, \boldsymbol{x}_{(n-m)}^{g2}, \boldsymbol{x}^{SVC} \,\right]^T_{1\times(10m+2n-2m+3)}$$

$$\boldsymbol{v} = \left[V_{D1}, V_{Q1}, \cdots, V_{Dn+1}, V_{Qn+1} \right]^T_{1\times 2(n+1)}$$

$$u = V_{\text{sup}}$$

$$\boldsymbol{i} = \left[I_{D1}, I_{Q1}, \cdots, I_{Dn+1}, I_{Qn+1} \right]^T_{1\times 2(n+1)}.$$

The state vector $\boldsymbol{x}$ is composed of the state variables defined in the following column vectors

$\boldsymbol{x}_m^{g1}$ represents the m^{th} generator equipped with the excitation system and PSS,

$$\boldsymbol{x}_m^{g1} = \left[\Delta\omega_m, \delta_m, E'_{qm}, E'_{dm}, X_{E1m}, X_{E2m}, E_{Lm}, X_{p1}, X_{p2}, X_{p3}\right]_{1\times 10}^T;$$

$\boldsymbol{x}_{(n-m)}^{g2}$ is the $(n\text{-}m)^{\text{th}}$ generator represented by the classical model,

$$\boldsymbol{x}_{(n-m)}^{g2} = \left[\omega_{n-m}, \delta_{n-m}\right]_{1\times 2}^T;$$

$\boldsymbol{x}^{SVC}$ is composed of the state variables of the SVC,

$$\boldsymbol{x}^{SVC} = \left[X_{s1}, X_{s2}, B_L\right]_{1\times 3}^T.$$

The vectors $\boldsymbol{i}$ and $\boldsymbol{v}$ are composed of currents and voltages at the devices' terminals, respectively. These vectors are expressed in the network's reference frame (D-Q axis). Lastly, u is the control input to the system. The equations for the components mentioned above are presented in Appendix A.

The size of the power system network can be reduced by eliminating all zero injection nodes in such a way that the voltages and current injections at the remaining nodes are unaffected. This will result in a nodal network equation with smaller dimensions, which enables a lower computational burden during power system simulations. The interconnected transmission network is then represented by the nodal equation [25]:

$$\boldsymbol{i} = \boldsymbol{Y}_N \boldsymbol{v}, \tag{2.3}$$

where $\boldsymbol{Y}_N$ is the nodal admittance matrix of the reduced network. The effects of the static loads are included in this matrix.

Linearization of (2.1) and (2.2) around an equilibrium point of the system leads to

$$\Delta\dot{\boldsymbol{x}} = \boldsymbol{A}_D\Delta\boldsymbol{x} + \boldsymbol{B}_D\Delta\boldsymbol{v} + \boldsymbol{B}\Delta u \tag{2.4}$$

$$\Delta \boldsymbol{i} = \boldsymbol{C}_D \Delta \boldsymbol{x} - \boldsymbol{Y}_D \Delta \boldsymbol{v} \,, \tag{2.5}$$

where $\Delta \boldsymbol{x}$ is the vector of increments in state variables, Δu is the change in the control signal, and $\Delta \boldsymbol{v}$ is the vector of increments in bus voltages.

Similarly, the linearization of (2.3) results in

$$\Delta \boldsymbol{i} = Y_N \Delta \boldsymbol{v} \quad . \tag{2.6}$$

Using (2.6) and (2.5), the terminal voltages can be expressed in terms of state variables,

$$\Delta \boldsymbol{v} = \left(\boldsymbol{Y}_N + \boldsymbol{Y}_D \right)^{-1} \boldsymbol{C}_D \Delta \boldsymbol{x} \quad . \tag{2.7}$$

Finally, substituting this last expression in (2.4) yields the overall state space representation:

$$\Delta \dot{\boldsymbol{x}} = \boldsymbol{A} \Delta \boldsymbol{x} + \boldsymbol{B} \Delta u \,, \tag{2.8}$$

where the state matrix $\boldsymbol{A}$ of the complete system is given by

$$\begin{aligned} \boldsymbol{A} &= \boldsymbol{A}_D + \boldsymbol{B}_D \left(\boldsymbol{Y}_N + \boldsymbol{Y}_D \right)^{-1} \boldsymbol{C}_D \\ &= \left[\boldsymbol{A} \right]_{(10m+2n-2m+3) \times (10m+2n-2m+3)} \end{aligned} \quad . \tag{2.9}$$

2.3 Modal analysis

In order to identify oscillatory modes of the linear system expressed in (2.9), an eigenanalysis is applied to the l by l state matrix $\boldsymbol{A}$.

The eigenvalues $\boldsymbol{\lambda}$ of $\boldsymbol{A}$ are obtained by solving the characteristic equation:

$$\det\left(\boldsymbol{A} - \lambda \boldsymbol{I} \right) = 0 \quad . \tag{2.10}$$

The l solutions of $\boldsymbol{\lambda} = \{\lambda_1, \lambda_2, \ldots, \lambda_l\}$ are eigenvalues of $\boldsymbol{A}$.

For a complex pair of eigenvalues $\lambda = \sigma \pm j\omega$, the real component provides the damping of the dynamic response, while the imaginary component gives the frequency of oscillation of this dynamic response. Thus, the damping ratio is given by

$$\zeta = \frac{-\sigma}{\sqrt{\sigma^2 + \omega^2}} \quad . \tag{2.11}$$

Additionally, the frequency of oscillation in Hz is given by

$$f = \frac{\omega}{2\pi} \quad . \tag{2.12}$$

In the context of small-signal stability, the oscillatory modes that have a damping ratio less than 3% are known as critical modes [25]. When designing stabilizing controls, however, a damping ratio of at least 5% should be one objective of control design [3].

For every eigenvalue λ_i there is an eigenvector ϕ_i which satisfies the equation

$$\boldsymbol{A}\phi_i = \lambda_i \phi_i \quad , \tag{2.13}$$

where the l-column vector ϕ_i is called the right eigenvector of $\boldsymbol{A}$ associated with the eigenvalue λ_i.

Similarly, the left eigenvector ψ_i associated with the eigenvalue λ_i is the l-row vector which satisfies

$$\psi_i \boldsymbol{A} = \lambda_i \psi_i \quad . \tag{2.14}$$

In the power systems' literature, the right eigenvector is known as the mode shape, and it reflects the relative distribution of a mode of oscillation throughout the system's dynamic states: information such as observability of an oscillatory mode across system states can be obtained from the corresponding components of the right eigenvector. The information given by the right eigenvector also permits classifying electromechanical modes in local and inter-area modes based on their frequency characteristics and on the participation of an individual machine or group of machines in one particular mode of oscillation. By way of example, power oscillations arising from local modes have only a slight fraction of generators participating in the oscillation. On the other hand, a large number of generators composing two or more groups oscillate against each other to produce inter-area power oscillations.

On the other hand, the left eigenvector serves as a measure of the participation of a specific input in the amplitude of the oscillation of a mode. Information such as the reachability of an oscillatory mode across system's dynamic states can be obtained by the corresponding components of the left eigenvector.

Note that the eigenvectors are dependent on the units of state variables, meaning that measuring the degree of activity of a different kind of variable (e.g., the rotor speed deviation $\Delta\omega$ and the SVC's equivalent admittance B_{SVC}) in a particular mode is affected by a scale factor. It is a common practice, however, to treat the right and left eigenvectors as normalized values such that $\psi_i \phi_i = 1$.

To measure the relative participation of the k^{th} dynamic state variable in the i^{th} system mode $\lambda_i = \sigma_i \pm j\omega_i$, and vice versa, the participation factor is calculated based on [25]:

$$\begin{aligned} p_{ki} &= \phi_{ki}\psi_{ik} \\ &= \frac{\partial \lambda_i}{\partial a_{kk}} \end{aligned}, \tag{2.15}$$

where ϕ_{ki} and ψ_{ki} are the k^{th} entries of the eigenvectors ϕ_i and ψ_i, respectively. This equation also indicates that the participation factor is equivalent to the sensitivity of the eigenvalue λ_i to the diagonal element a_{kk} of the state matrix $\boldsymbol{A}$. In addition, the value of this factor is dimensionless.

Lastly, and from a physical standpoint, the value of ϕ_{ki} measures the degree of activity of the k^{th} state variable in the i^{th} mode, whereas the value of ψ_{ki} weights the contribution of this activity to the i^{th} mode. Note also that by using the eigenvector normalization $\psi_i \phi_i = 1$ the sum of all participation factors associated with a system mode or with a state variable is equal to unity.

2.4 IEEE 50-generator test bed system

To illustrate the bases for the proposed method, the IEEE 50-generator system [31], [24] is considered as the test bed in this dissertation. This system includes all the modeling features and operational complexities of a large-scale power system. The representative diagram of the system is shown in Figure 2.2.

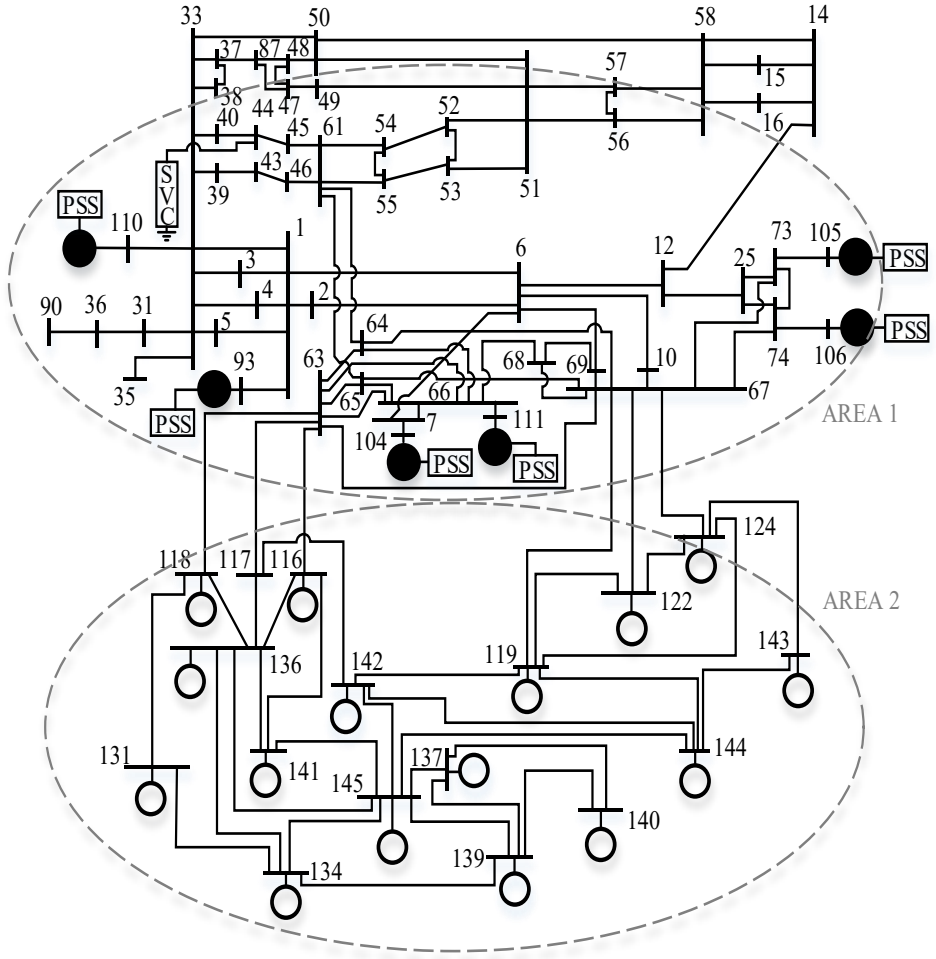

Figure 2.2 One-line diagram of the IEEE 50-generator system with areas of interest encircled [32]

This power system is composed of 145 buses and 50 synchronous machines. Six machines are mathematically represented by the two-axis model with the IEEE AC-4 excitation system and the speed-based PSS model, while the rest of the generators are described by the classical

model. The nominal capacity of the SVC installed at bus #44 is Q_{SVC} = ±400 MVAr. The network data and dynamic parameters can be found in [33].

Modes of oscillation of the test bed system

The operating conditions of the IEEE 50-generator system reported in [24] are considered to assess the small-signal stability analysis of the system without the damping controller installed for the SVC. Different operating points of the system are characterized by changing the active power at bus #93 and bus #110. This generation is varied from 2x1400 MW to 2x1900 MW.

A complete eigenvalue analysis is performed for each system operating point by using the small-signal analysis tool (SSAT) [34]. The presence of two poorly damped inter-area modes are found in the system. The results for the most critical mode are shown in Table 2.1, where the damping ratio and the frequency of oscillation, $\zeta @ f$, are reported in the second column. These results clearly show that the system with installed PSSs reaches its stability limit at around 2×1700 MW.

Table 2.1 Poorly damped inter-area mode of system with PSS

G93 and G110 (MW)	Mode
2 x 1400	8.11% @ 0.285 Hz
2 x 1500	6.48% @ 0.279 Hz
2 x 1600	4.14% @ 0.272 Hz
2 x 1700	1.16% @ 0.266 Hz
2 x 1800	-3.00% @ 0.260 Hz
2 x 1900	-7.91% @ 0.253 Hz

The mode shape of the critical mode at the operating point 2x1400 MW is plotted in Figure 2.3, and corresponds to an inter-area mode because of the oscillation between Area 1 (with main generators: 93, 104, 105, 110, 11) and Area 2 (with main generators: 137, 139, 140, 145).

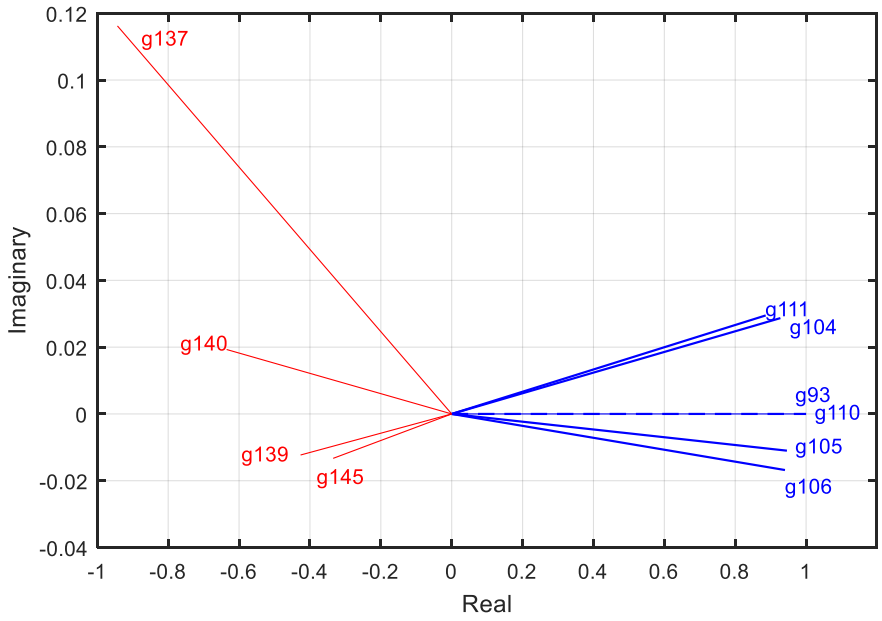

Figure 2.3 Mode shape for the critical mode at 0.28 (Hz).

2.5 Selection of stabilizing signals

The control effectiveness of a SVC to damp out a particular mode of oscillation depends on its location in the transmission system. The determination of the best location for the SVC is not within the scope of this research. Nevertheless, the bus participation factor [35] can be utilized to place the SVC efficiently.

To identify the best candidate signal for the control input Δu in the power system represented by (2.8), the approach of residue and observability factors is utilized [9]. Several stabilizing signals, such as generator rotor speed ($\Delta\omega$), frequency (Δf), active power flow through transmission lines (ΔP_{pq}), bus voltage angle difference ($\Delta\theta_{pq}$) and the difference between the center of inertia (COI) associated with different control areas have been utilized for the SDC [36].

An important factor for choosing the control input is the availability of infrastructure that permits the measurement of this input in real time and permits sending it to the controller from a remote point. In this context, the signals measured by PMUs in the network may be potential candidates for being control input signals. In practice, the magnitude of line current

is employed as a control signal because of its modal characteristics (observability) under all system's operating conditions [37]. This signal then needs to be expressed in terms of state variables.

The vector of the current of the transmission line *p*-*q* is defined in the reference frame *D*-*Q* axis by

$$\begin{aligned}\bar{I}_{pq} &= \left(g_{pq} + jb_{pq}\right)\left(\bar{V}_p - \bar{V}_q\right) \\ &= I_{pq,D} + jI_{pq,Q}\end{aligned}, \tag{2.16}$$

where $g_{pq} + jb_{pq}$ is the primitive admittance of the line *p*-*q*, whereas $\bar{V}_p$ and $\bar{V}_q$ are the vectors of voltages at buses *p* and *q*, respectively.

It is known from (2.16) that

$$\left|\bar{I}_{pq}\right|^2 = I_{pq,D}^2 + jI_{pq,Q}^2 \ . \tag{2.17}$$

By linearizing the above equation around the nominal point of the system,

$$\Delta I_{pq} = \frac{I_{pqD0}}{\left|\bar{I}_{pq0}\right|}\Delta I_{pq,D} + \frac{I_{pqQ0}}{\left|\bar{I}_{pq0}\right|}\Delta I_{pq,Q} \tag{2.18}$$

where the subscript 0 of the variables indicates the initial values at the systems' nominal point of operation.

By using (2.16) in (2.18) results in

$$\begin{aligned}\Delta I_{pq} &= \begin{bmatrix} \dfrac{I_{pqD0}}{\left|\bar{I}_{pq0}\right|} & \dfrac{I_{pqQ0}}{\left|\bar{I}_{pq0}\right|} \end{bmatrix}\begin{bmatrix} g_{pq} & -b_{pq} \\ b_{pq} & g_{pq} \end{bmatrix}\begin{bmatrix} \Delta V_{pD} - \Delta V_{qD} \\ \Delta V_{pQ} - \Delta V_{qQ} \end{bmatrix} \\ &= \boldsymbol{I}_{\boldsymbol{pq0}}\boldsymbol{y}_{pq}\Delta\boldsymbol{v}_{pq}\end{aligned} . \tag{2.19}$$

If the bus voltages *p* and *q* are not included in the vector of incremental bus voltages $\Delta\boldsymbol{v}$ in (2.7), the augmented vector of incremental bus voltages $\Delta\boldsymbol{v}_{\boldsymbol{A}}$ are defined in terms of ΔV_{pD}, ΔV_{pQ}, ΔV_{qD} and ΔV_{qQ} by

$$\begin{aligned}\Delta \boldsymbol{v}_A &= \left[\Delta V_{D1}, \Delta V_{Q1}, \cdots, \Delta V_{Dn+1}, \Delta V_{Qn+1}, \Delta V_{pD}, \Delta V_{pQ}, \Delta V_{qD}, \Delta V_{qQ}\right]^T \\ &= \left[\Delta \boldsymbol{v}^T \;\vdots\; \Delta V_{pD} \quad \Delta V_{pQ} \quad \Delta V_{qD} \quad \Delta V_{qQ}\right]^T\end{aligned} . \tag{2.20}$$

Modifying (2.5) and (2.6) to express the currents' injection equation in terms of $\Delta \boldsymbol{v}_A$ instead of $\Delta \boldsymbol{v}$ and using (2.7) result in

$$\Delta \boldsymbol{v}_A = \left(\boldsymbol{Y}_{NA} + \boldsymbol{Y}_{DA}\right)^{-1} \boldsymbol{C}_{DA} \Delta \boldsymbol{x} , \tag{2.21}$$

where $\boldsymbol{Y}_{NA}$ is the augmented matrix of the admittance matrix of the reduced network. $\boldsymbol{Y}_{DA}$ and $\boldsymbol{C}_{DA}$ are conformable matrices for the expression (2.5).

The vector of incremental bus voltages *p* and *q* are represented by

$$\begin{aligned}\Delta \boldsymbol{v}_{pq} &= \begin{bmatrix} 0 & \cdots & 0 & 1 & 0 & -1 & 0 \\ 0 & \cdots & 0 & 0 & 1 & 0 & -1 \end{bmatrix}_{2\times 2(n+3)} \left[\Delta \boldsymbol{v}_A\right]_{2(n+3)\times 1} \\ &= \boldsymbol{b} \Delta \boldsymbol{v}_A\end{aligned} . \tag{2.22}$$

Combining (2.22) and (2.19) leads to

$$\Delta I_{pq} = \boldsymbol{I}_{\boldsymbol{pq0}} \boldsymbol{y}_{pq} \boldsymbol{b} \Delta \boldsymbol{v}_{\boldsymbol{A}} . \tag{2.23}$$

Finally, by substituting (2.21) into (2.23), the representation of the line current is

$$\begin{aligned}\Delta I_{pq} &= \boldsymbol{I}_{\boldsymbol{pq0}} \boldsymbol{y}_{pq} \boldsymbol{b} \left(\boldsymbol{Y}_{NA} + \boldsymbol{Y}_{DA}\right)^{-1} \boldsymbol{C}_{DA} \Delta \boldsymbol{x} \\ &= \boldsymbol{C} \Delta \boldsymbol{x}\end{aligned} , \tag{2.24}$$

where $\boldsymbol{C}$ is called the output matrix of the system represented in (2.8).

Modal observability, controllability and residues

For evaluating the control for a particular mode of oscillation in the system by means of a stabilizing signal, the relation between the output ΔI_{pq} and input Δu of the system is analyzed. The transfer function equivalent *G(s)* of (2.8) and (2.9) is the following [8],

$$G(s) = \boldsymbol{C}\left(s - \boldsymbol{A}\right)^{-1}\boldsymbol{B} = \sum_{i=1}^{l} \frac{\boldsymbol{C}\phi_i \psi_i \boldsymbol{B}}{s - \lambda_i} = \sum_{i=1}^{l} \frac{R_i}{s - \lambda_i} \quad , \tag{2.25}$$

where R_i is known as a modal residue, as it is the product or factor of modal observability ($\boldsymbol{C}\phi_i$) and modal controllability ($\psi_i \boldsymbol{B}$). For a particular eigenvalue λ_i, the higher the magnitude of the residue the less control effort (gain) is needed, and the higher the phase lag, the more phase compensation blocks are required in the feedback path. In this sense, the higher magnitude of the modal observability's product, the higher observability of the particular oscillation mode is in the signal represented by the output ΔI_{pq}. The product of the modal controllability measures the controllability of the specified mode by means of the input Δu; thus, this value is influenced by the location of the SVC in the transmission network.

Based on the information mentioned above, the selection of the candidate signals for the control input Δu is based on those signals with higher values of the residues and the magnitude of modal observability.

Candidate control signals for the test-bed system

Regarding the critical mode around 0.28 Hz (results presented in Section 2.4) of the test bed system, the candidate control signals (for the SVC) with relatively large values of residue and observability factors are listed in Table 2.2. The wide-area signal $\Delta I_{63\text{-}66}$ presents the higher modal residue and the higher modal observability, while the signal $\Delta I_{44\text{-}45}$ is the best candidate for a local signal. From the results, the remote signals are better candidate signals for the control input of the system than the local signals.

Table 2.2 Modal residues and observability with regard to the critical mode

Signals	Residue	Observability (absolute value)
$\Delta I_{63\text{-}66}$	0.0111 + *j* 0.0113	0.3286
$\Delta I_{61\text{-}63}$	0.0094 + *j* 0.0096	0.2783
$\Delta I_{1\text{-}6}$	0.0053 + *j* 0.0057	0.0150
$\Delta I_{44\text{-}45}$ (local)	0.0015 + *j* 0.0015	0.0445
$\Delta I_{44\text{-}42}$ (local)	0.0003 + *j* 0.0003	0.0096

2.6 SDC utilized for the proposal

Comprehensive research about the methods for designing damping controllers using wide-area signals has been conducted in [8], [38]. The effect of time delay associated with the remote control inputs, as well as the variation of nominal operating conditions, may affect the performance of the controller negatively. The use of multiple global signals for the SDC has been proposed in [9] and [39] to enhance the small-signal stability of the system, which can present several critical inter-area modes. These centralized designs give support to the control afforded by the PSSs. In practical power systems, however, the communications' infrastructure for remote signals can suffer failures. Therefore, the effectiveness of SDC is also affected.

The robust SDC proposed in [24] is employed in this dissertation. The two-input single-output (TISO) controller utilizes both a wide-area signal . and a local signal z to assure that the system is stabilized if the remote signal is lost. The block diagram of the SVC with the SDC is shown in Figure 2.4. The washout block with a limiter secures that the supplementary signal V_{sup} only operates in the transient state. The controller employs the H_∞ optimization approach to deal with the uncertainties caused by changes in operating conditions of the power system. In addition, the second-order Padé approximation [40] is used for the communication delay modeling.

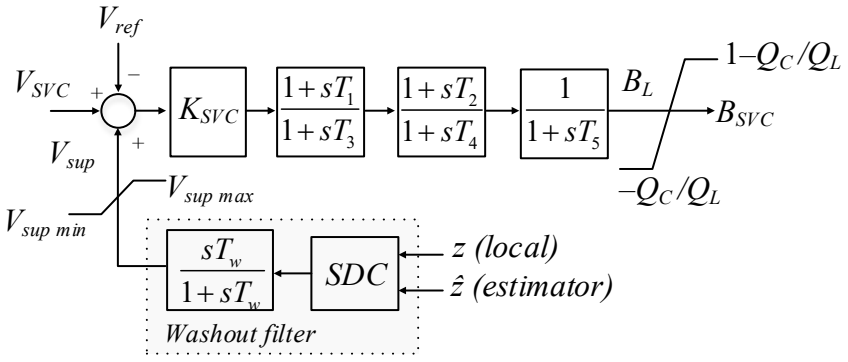

Figure 2.4 SVC model with SDC utilized

For the novel control scheme proposed in this work, the wide-area measurement signal $\hat{z}$ is ensured by using a state estimator, while the local signal z is obtained from a PMU installed

at the SVC bus. The method for estimating the control signal will be introduced in the following chapter.

Small-signal stability analysis of the test bed system with a SDC installed in the SVC

From the results for the best candidate control signals presented in the previous section, the signals $\Delta I_{63\text{-}66}$ and $\Delta I_{44\text{-}45}$ are selected as the wide-area signal and the local signal, respectively, to be utilized in the robust SDC. To establish the control for the critical mode of oscillation around 0.28 Hz, the parameters reported in [24] for the SDC associated with the SVC are used. The SDC's limit bounds are set at $V_{sup\_max} = 0.1$ and $V_{sup\_min} = -0.1$ p.u., and the nominal transmission delay is considered to be 100 ms.

A complete eigenanalysis is performed at different operating points of the closed-loop system using the commercial software SSAT. From the results regarding the critical mode, shown in Table 2.3, the use of the SDC extends the small-signal stability limits of the system at the operating point 2x1800 MW. Note that even for the case when the communication of the remote signal is lost, the local control input signal provides strength for the damping control.

Table 2.3 Comparison of damping ratio of the critical mode of the IEEE 50-generator test system utilizing SDC to control a SVC

G93 & G110 (MW)	PSS (no SDC)	PSS+SDC (loss of communication)	PSS+SDC
2×1600	4.13%@0.272 Hz	8.00%@0.271 Hz	17.09%@0.294 Hz
2×1700	1.15%@0.266 Hz	4.93%@0.262 Hz	19.68%@0.281 Hz
2×1800	-3.01%@0.260 Hz	0.11%@0.253 Hz	15.73%@0.215 Hz

2.7 Selection of unconventional stabilizing signals

In line with the proposed method, special attention has been paid to obtain an alternative wide-area signal for the SDC installed for the SVC.

The new control signal is selected based on a modal analysis as follows.

1. An eigenanalysis of the system is performed by not considering any SDC embedded in the network, meaning that the open-loop system is analyzed following the procedure discussed in Section 2.3.

2. From the information regarding the mode shape associated with the critical mode, the new signals are selected. Based on the mode shape shown in Figure 2.3, the state variables of generators #93, #110, #137 and #140 have the higher participation in the critical inter-area mode. Hence, the new control signals contained in $\hat{z}$ correspond to the voltage phase angles θ_i at nodes at which these generators are connected:

$$\hat{z} = \theta_{93} + \theta_{110} - \theta_{137} - \theta_{140} . \tag{2.26}$$

   It will be shown later that the value of each voltage phase angle can be directly obtained from the state estimation of the power system.

3. In order to verify the suitability of this selection, a new eigenanalysis is carried out by considering that the SDC is embedded in the system and that the control signals are supplied to the controller.

   The closed-loop system of the previous section is evaluated by employing the new signal $\hat{z}$. The results obtained by using the SSAT software are shown in Figure 2.4. The new control signal slightly improved the damping in comparison to the SDC that uses the wide-area control input $I_{63\text{-}66}$.

Table 2.4 Comparison of damping ratio of the critical mode using an alternative wide-area signal in the SDC of a utilized SVC

G93 & G110 (MW)	**PSS + SDC** ***($I_{63\text{-}66}$)***	**PSS+SDC** ***(new signal)***
2×1600	17.09%@0.294 Hz	21.38%@0.296 Hz
2×1700	19.68%@0.281 Hz	24.52%@0.278 Hz
2×1800	15.73%@0.215 Hz	16.18%@0.217 Hz

2.8 Summary

In this chapter, the foundations for the small-signal stability analysis are established through the computing of modal characteristics of the test bed system represented by the IEEE 50-generator system. The procedure for obtaining the state-space representation of the system is also reported. The best candidate control input signals for the SDC associated with the SVC are derived from first principles employing the modal residues and observability factor. The magnitude of the current flowing through a transmission line is chosen as the control input signals. Furthermore, a new wide-area control signal based on the mode shape of the critical mode is proposed.

The robust SDC utilized in the proposed method is introduced in this chapter, and its performance in the test bed system is carried out by applying a complete eigenanalysis to the system using the commercial software SSAT. The results for the critical mode shows that the SDC improves the damping control afforded by the PSSs. Consequently, the stability limit for the small signal is extended, even when the remote signal for the damping controller is lost.

Chapter 3

Tracking state estimation based on PMUs

3.1 Introduction

The state estimator (SE) is one of the key components in modern energy management systems (EMS) because it is a vital module for validating the raw measurements from the supervisory control and data acquisition (SCADA) system, and it provides accurate information about the power system state (i.e. bus voltages and angles) at a specific point of time. This critical information at regular intervals is used for downstream applications in EMS, such as on-line power flow, economic power dispatch, as well as contingency analysis, voltage stability analysis, transient stability analysis and system alarms processing [41], [42].

An SE basically comprises the following functions [43]:

1. **Measurement prefiltering**: A set of rudimentary consistency checks is implemented to detect and discard measurements that are clearly wrong (negative voltage magnitudes, power flows out of operative ranges, etc.).
2. **Topology processor**: On the basis of the status of switching devices and the physical layout of substations, electrical network model (current connectivity of the system) is built.

3. **Observability analysis**: This determines if the system state can be estimated by using the available measurements for the entire network. If only a subset of nodes is observable, then it identifies the observable islands.
4. **State estimation**: This computes the statistically optimal network state or the state that best fits the remotely captured measurements for a given set of network parameters and network connectivity.
5. **Bad data processor:** This function detects the presence of potential Gaussian and non-Gaussian gross errors in the set of measurements. If the redundancy is adequate, those undesirable measurements can be identified and removed.

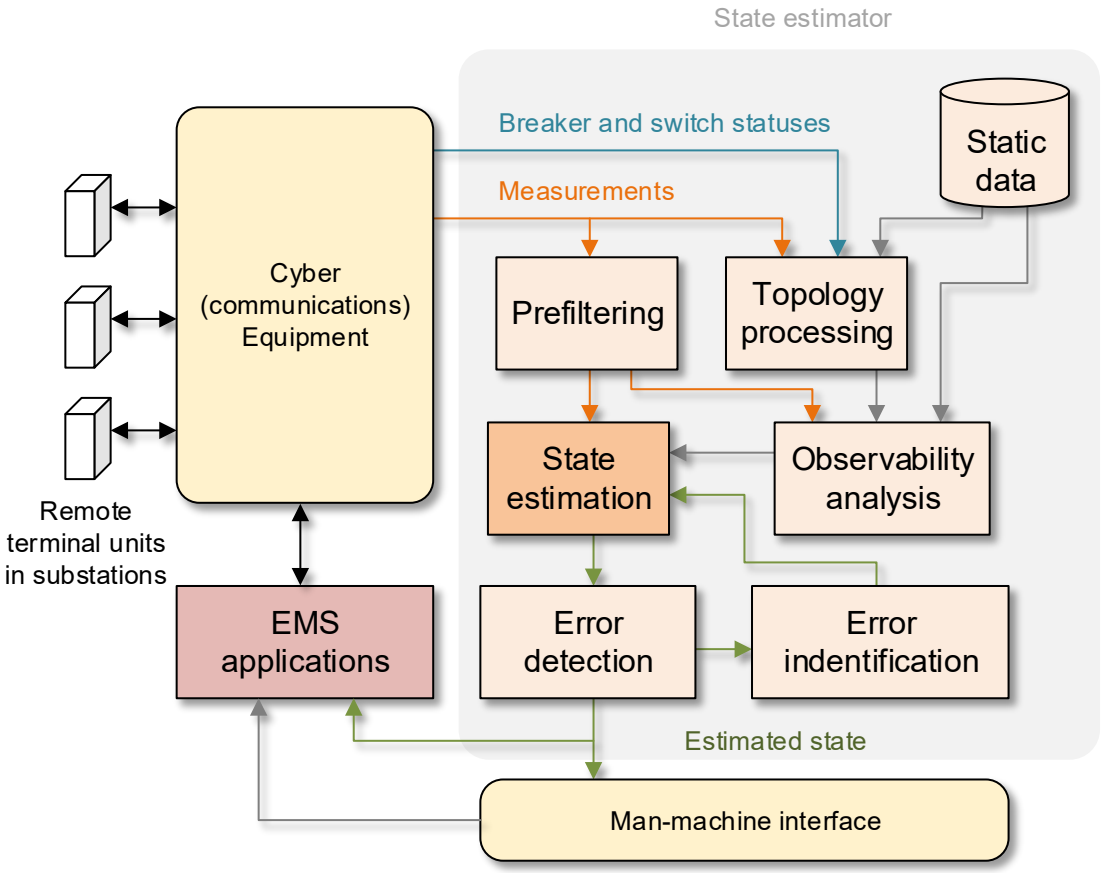

Figure 3.1 shows a basic schematic diagram of the SE [43], [44].

The weighted least square (WLS) method is the most common technique used in the SE for estimating the system state at a given point of time. The mathematical formulation for the WLS using nonlinear models associated with the measurements is iteratively solved. The conventional measurements, such as active/reactive power flows, active/reactive power injections and magnitudes of bus voltages, have an inherently slow reporting rate (3 to 5 s), and thus, the conventional SE is suitable for monitoring a power system in a quasi-steady state of operation [45].

The advent of the PMUs in the transmission system has opened up the opportunities for developing new SEs. An estimator that considers conventional and synchronized phasor measurements is called a hybrid state estimator (HSE) [46]–[48], which provides a better accuracy for the estimated values. In addition, the use of the synchronized measurements has allowed predicting and reconstructing pseudo-measurements to ensure the observability in the estimation process [49], [50]. The dependency on the conventional measurements, however, results in the HSE being performed at a sampling rate of seconds. Furthermore, the implementation of this type of estimator to obtain the operation state of large-scale power systems may have a high computational burden.

The Kalman filter (KF) theory has been utilized for tracking the dynamics of the system's states in real time since the 1970s [51]. The extended Kalman filter (EKF) and unscented Kalman filter (UKF) are the most common techniques employed for tracking state estimators (TSE) [52], [53]. In this context, the values estimated by using the KF approach are obtained recursively; furthermore, an additional estimation process is not required when the bad data detector (BDD) identifies a gross error at a given discrete instant of time, as occurs in the case of the chi-square test method for BDD utilized in the formulation of the WLS [54]. Since the KF requires a dynamic model of the system under analysis, as well as the nonlinear models of the measurements used to perform the estimation, the complexity of these models can compromise the computational burden of this approach. This drawback can be overcome, however, by implementing a KF-based state estimator by using parallel computing and graphics processing units (GPUs) as reported in [55]. In this proposal, the state estimation is performed based on measurements provided from PMUs, with a number of measurements that assures the power network’s observability. It is also assumed that the performance of the

instruments is not adversely affected during electromechanical transients [56]. Although the measurements of some systems consist mainly of conventional measurements, the actual cost of PMUs has fallen considerably which has facilitated their growing installation in the transmission network [57].

3.2 Mathematical formulation of the estimator

The model of the power system is represented by Holt's exponential smoothing technique [52] as

$$\tilde{\boldsymbol{x}}_k = \boldsymbol{F}_{k-1}\boldsymbol{x}_{k-1} + \boldsymbol{g}_{k-1} + \boldsymbol{w}_{k-1}\,, \tag{3.1}$$

where the subscripts k and $k-1$ denote two successive discrete-time instants separated by T_s seconds, $\tilde{\boldsymbol{x}}_k$ is the predicted state vector, and $\boldsymbol{x}_{k-1}$ is the n-dimensional vector of the true states' values composed of phase angles θ_{k-1} (in radians) and voltage magnitudes V_{k-1} (p.u.). The model error $\boldsymbol{w}_{k-1}$ is represented by a Gaussian noise with zero mean and covariance matrix $\boldsymbol{Q}_{k-1}$. Matrix $\boldsymbol{F}_{k-1}$ and vector $\boldsymbol{g}_{k-1}$ are calculated as

$$\boldsymbol{F}_{k-1} = \alpha(1+\beta)\,\boldsymbol{I} \tag{3.2}$$

$$\boldsymbol{g}_{k-1} = (1+\beta)(1-\alpha)\,\boldsymbol{x}_{k-1} - \beta\boldsymbol{a}_{k-2} + (1-\beta)\,\boldsymbol{b}_{k-2} \tag{3.3}$$

$$\boldsymbol{a}_{k-1} = \alpha\boldsymbol{x}_{k-1} + (1-\alpha)\,\tilde{\boldsymbol{x}}_{k-1} \tag{3.4}$$

$$\boldsymbol{b}_{k-1} = \beta\left(\boldsymbol{a}_{k-1} - \boldsymbol{a}_{k-2}\right) + (1-\beta)\,\boldsymbol{b}_{k-2}\,, \tag{3.5}$$

where $\boldsymbol{I}$ is the identity matrix, while α and β are the parameters lying in the range from 0 to 1. These values are found by performing off-line simulations to attain the minimum mean absolute errors (MAE) [49]. In this formulation, boldface denotes vectors and matrices. The measurement model is given by

$$\begin{aligned} \boldsymbol{z}_k &= \begin{bmatrix} \theta_{PMU} \\ V_{PMU} \\ I_{brach,r} \\ I_{branch,i} \end{bmatrix} + \begin{bmatrix} \varepsilon_1 \\ \varepsilon_2 \\ \vdots \\ \varepsilon_m \end{bmatrix}, \\ &= \boldsymbol{h}_k\left(\boldsymbol{x}_k\right) + \boldsymbol{\varepsilon}_k \end{aligned} \tag{3.6}$$

where $\boldsymbol{z}_k$ is the m-measurement vector related to state variables through the nonlinear functions $\boldsymbol{h}_k$. The set of measurements given by PMUs includes the bus voltage phasor quantities V_{PMU} (p.u.) and phase angle θ_{PMU} (rad), as well as the branch current phasor for the transmission components $I_{branch,r}$ (p.u.) and $I_{branch,i}$ (p.u.). The voltage and current measurements are represented in polar and rectangular coordinates, respectively. The mathematical models of these measurements are presented in Appendix B. The measurement error $\boldsymbol{\varepsilon}_k$ is represented by a Gaussian noise with zero mean and covariance matrix $\boldsymbol{R}_k$.

The noise sequences $\boldsymbol{w}_{k-1}$ and $\boldsymbol{\varepsilon}_k$ are considered to be white Gaussian with the following characteristics:

$$E\left[\boldsymbol{w}_k \boldsymbol{w}_k^T\right] = \boldsymbol{Q}_k = diag\left\{\sigma_{w1}^2, \sigma_{w2}^2, \ldots, \sigma_{wn}^2\right\} \tag{3.7}$$

$$E\left[\boldsymbol{\varepsilon}_k \boldsymbol{\varepsilon}_k^T\right] = \boldsymbol{R}_k = diag\left\{\sigma_{\varepsilon 1}^2, \sigma_{\varepsilon 2}^2, \ldots, \sigma_{\varepsilon m}^2\right\} \tag{3.8}$$

$$\begin{cases} E\left[\boldsymbol{w}_k \boldsymbol{w}_j^T\right] = 0 \\ E\left[\boldsymbol{\varepsilon}_k \boldsymbol{\varepsilon}_j^T\right] = 0 \end{cases} \qquad j \neq k \tag{3.9}$$

$$E\left[\boldsymbol{w}_k \boldsymbol{\varepsilon}_j^T\right] = 0, \tag{3.10}$$

where E indicates the expected values.

Because the signals from commercial PMUs are commonly expressed in polar coordinates (I_{PMU}, θ_I), the standard deviations of the current phasor measurements in (3.6) are thus calculated as [47]:

$$\sigma_{Ibranch,r} = \sqrt{\left(\sigma_{IPMU} \cos\theta_I\right)^2 + \left(\sigma_{\theta I} I_{PMU} \sin\theta_I\right)^2} \tag{3.11}$$

$$\sigma_{Ibranch,i} = \sqrt{\left(\sigma_{IPMU}\sin\theta_I\right)^2 + \left(\sigma_{\theta I} I_{PMU}\cos\theta_I\right)^2}\,. \tag{3.12}$$

By using the dynamic model of the system (3.1) and the measurements' model (3.6), the EKF formulation is employed through the prediction and update steps [58] defined as follows.

1) Initialization: the initialization of the filter at $k = 0$, the estimated state vector $\hat{\boldsymbol{x}}_0$ and the covariance matrix $\boldsymbol{P}_0$ are computed as

$$\hat{\boldsymbol{x}}_0 = E\left[\boldsymbol{x}_0\right] \tag{3.13}$$

$$\boldsymbol{P}_0 = E\left[\left(\boldsymbol{x}_0 - \hat{\boldsymbol{x}}_0\right)\left(\boldsymbol{x}_0 - \hat{\boldsymbol{x}}_0\right)^T\right]. \tag{3.14}$$

2) Prediction: the predicted state vector $\tilde{\boldsymbol{x}}_k$ and predicted covariance $\boldsymbol{P}_k^-$ are calculated as

$$\tilde{\boldsymbol{x}}_k = \boldsymbol{F}_{k-1}\hat{\boldsymbol{x}}_{k-1} + \boldsymbol{g}_{k-1} + \boldsymbol{w}_{k-1} \tag{3.15}$$

$$\boldsymbol{P}_k^- = \boldsymbol{F}_{k-1}\boldsymbol{P}_{k-1}\boldsymbol{F}_{k-1}^T + \boldsymbol{Q}_{k-1}\,. \tag{3.16}$$

3) Update: the estimated state vector $\hat{\boldsymbol{x}}_k$ and the covariance matrix $\boldsymbol{P}_k$ are given by

$$\hat{\boldsymbol{x}}_k = \tilde{\boldsymbol{x}}_k + \boldsymbol{K}_k\left[\boldsymbol{z}_k - \boldsymbol{h}_k\left(\tilde{\boldsymbol{x}}_k\right)\right] \tag{3.17}$$

$$\boldsymbol{P}_k = \left(\boldsymbol{I} - \boldsymbol{K}_k\boldsymbol{H}_k\right)\boldsymbol{P}_k^-\,, \tag{3.18}$$

where the gain $\boldsymbol{K}_k$ and $\boldsymbol{H}_k$ are expressed as

$$\boldsymbol{K}_k = \boldsymbol{P}_k^-\boldsymbol{H}_k^T\left(\boldsymbol{H}_k\boldsymbol{P}_k^-\boldsymbol{H}_k^T + \boldsymbol{R}_k\right)^{-1} \tag{3.19}$$

$$\boldsymbol{H}_k = \begin{bmatrix} \boldsymbol{I} & 0 \\ 0 & \boldsymbol{I} \\ \left.\frac{\partial I_{branch,r}}{\partial \theta_{PMU}}\right|_{\tilde{\boldsymbol{x}}_k} & \left.\frac{\partial I_{branch,r}}{\partial V_{PMU}}\right|_{\tilde{\boldsymbol{x}}_k} \\ \left.\frac{\partial I_{branch,i}}{\partial \theta_{PMU}}\right|_{\tilde{\boldsymbol{x}}_k} & \left.\frac{\partial I_{branch,i}}{\partial V_{PMU}}\right|_{\tilde{\boldsymbol{x}}_k} \end{bmatrix}_{m \times n} = \left.\frac{\partial \boldsymbol{h}_k}{\partial \boldsymbol{x}}\right|_{\tilde{\boldsymbol{x}}_k} . \tag{3.20}$$

A unique solution of $\hat{\boldsymbol{x}}_k$ can be calculated if the gain matrix $\boldsymbol{K}_k$ is nonsingular or equivalently if $\boldsymbol{H}_k$ has a full column rank [59], i.e. rank($\boldsymbol{H}_k$) = n; in this case, the system is observable. The lack of measurements in the estimation process may lead the system to become unobservable. Fortunately, the predicted states in the KF formulation can be utilized to obtain pseudo-measurements to restore the observability.

The estimator may use a reference angle from a PMU to reduce the number of states to be estimated to n-1 state variables. The reference measurement can be corrupted, however, such that all bus phase angles are measured with respect to the reference dictated by the Global Positioning System (GPS) [47].

3.3 Bad data analysis

The measurements obtained from instruments may be corrupted, and consequently, the estimation accuracy is affected. Hence, the detection, identification and removal/correction of measurements with gross errors are vital for ensuring an accurate estimation of the system's state. From a conventional perspective of static-state estimation, some sort of test, e.g. chi-square test, is applied to detect whether a bad data is contained in the set of measurements. If this test is positive, a process of identification is performed for determining which of all the data are bad. Lastly, the identified measurements with gross errors are suppressed or corrected to newly perform a state estimate utilizing only the good measurements. [60]. The use of this conventional analysis can fail, however, when applied to the PMU's measurements because their errors have non-Gaussian distribution [61], [62].

Hence, an accurate identification of gross errors in measurements can be performed by defining an innovation process vector in the EKF algorithm:

$$\boldsymbol{v_k} = \boldsymbol{z_k} - \boldsymbol{h_k}\left(\tilde{\boldsymbol{x}}_{\boldsymbol{k}}\right), \tag{3.21}$$

and the *i*-th measurement is normalized in the innovation process [63] as

$$\lambda_{k,i} = v_{k,i} / \rho_{k,i}, \qquad i = 1, 2, \ldots, m, \tag{3.22}$$

where

$$\rho_{k,i}^2 = \boldsymbol{H}_{k,i}\boldsymbol{P}_{k,i}^{-}\boldsymbol{H}_{k,i}^{T} + \sigma_i^2, \tag{3.23}$$

In this case, $\boldsymbol{H}_{k,i}$ is the *i*-th row of $\boldsymbol{H}_k$ and also corresponds to the i^{th} diagonal element of $\boldsymbol{R}_k$.

In this work, the criterion for bad data detection is defined by

$$\left|\lambda_{k,i}\right| > \lambda_{\max,i} \qquad i = 1, 2, \ldots, m, \tag{3.24}$$

where the threshold values $\lambda_{\max}$ are system dependent and are determined by using off-line simulations. The measurement value with bad data is replaced by the predicted value.

The power system model in (3.1) has been reported in [52], [64], [53] by assuming a quasi-steady state behavior of the system that is monitored in time steps of few seconds. Taking these facts into account, a time step of *Ts* =10 ms is considered in this work. When a significant variation in the system's operation state is caused by the occurrence of a large disturbance, the performance of the dyamic state estimator (DSE) could be affected because the value of the state prediction in (3.15) is predicted based on the values of the system's state prior to the disturbance. To handle this issue, a bad data detection (BDD) analysis is utilized. A large disturbance is detected in the EKF algorithm when measurements of voltage magnitude V_{PMU} at different buses of the network are simultaneously identified with a gross error in (3.24). In this case, the existence of bad data is not considered, and the values of the covariance matrix $\boldsymbol{Q}$ related to the bad measurements are modified instead of replacing the bad data with predicted values. This means that the model prediction is not weighted in the estimation process during large variations in the power system's operation state.

3.4 TSE on IEEE 50-generator system

In order to numerically illustrate the effectiveness of the proposed approach to tracking the system's state, the test bed system described in Section 2.4 is considered in the simulations reported in this section. The measurements are obtained by conducting nonlinear time-domain simulations by using the commercial software TSAT, and the following scenario is considered.

- It is considered that the system operating in its nominal condition (2x1700 MW) is subjected to the contingency scenario defined by a solid three-phase fault, incepted at time t = 5 seconds at bus 7 and cleared after six cycles (0.1s). The electrical frequency of the system is 60 Hz.
- The system is observable through the set of 304 measurements composed of PMUs (multichannel) located at the following buses: 1, 7, 13, 22, 25, 28, 29, 33, 36, 43, 44, 47, 51, 58, 59, 60, 61, 69, 76, 81, 84, 85, 88, 96, 102, 105, 106, 111, 113, 114, 121, 126, 140, and 142. Measurements of branch currents flowing from PMU buses to the adjacent buses are also obtained.
- A Gaussian white noise with a zero mean and a standard deviation σ = 0.001 (pu) is inserted in the measurements. The initial covariance matrix is $\boldsymbol{P}_0 = [0.001^2 \times \boldsymbol{I}_{290}]$, and the covariance matrix of the process is $\boldsymbol{Q} = [0.001^2 \times \boldsymbol{I}_{290}]$, where $\boldsymbol{I}_{290}$ is an identity matrix of order 290.

The accuracy of the estimator at time k and over the whole simulation is quantified by using the following indices [49].

The mean absolute percentage error (MAPE) evaluates the voltage magnitude in percent:

$$\mathrm{MAPE}(k) = \frac{1}{N}\sum_{i=1}^{N}\left|\frac{V_{i,k} - \hat{V}_{PMUi,k}}{V_{i,k}}\right| 100\% \tag{3.25}$$

$$\mathrm{MAPE} = \frac{1}{T}\sum_{k=1}^{T}\frac{1}{N}\sum_{i=1}^{N}\left|\frac{V_{i,k} - \hat{V}_{PMUi,k}}{V_{i,k}}\right| 100\%, \tag{3.26}$$

where N is the number of buses, T is the total number of the successive TSE executions, and $V_{i,k}$ as well as $\hat{V}_{PMUi,k}$ are the exact value of voltage magnitude and the estimated value, respectively.

The mean absolute error (MAE) index assesses the accuracy of the estimated voltages' phase angles $\hat{\theta}_{PMUi,k}$ (in rad):

$$\mathrm{MAE}(k) = \frac{1}{N}\sum_{i=1}^{N}\left|\theta_{i,k} - \hat{\theta}_{PMUi,k}\right| \tag{3.27}$$

$$\mathrm{MAE} = \frac{1}{T}\sum_{k=1}^{T}\frac{1}{N}\sum_{i=1}^{N}\left|\theta_{i,k} - \hat{\theta}_{PMUi,k}\right|. \tag{3.28}$$

In order to obtain the appropriate α and β parameters of the prediction state equation in (3.15), the minimum MAPE and MAE indices are computed by varying the values of these parameters for several simulations. The summary of the results is shown in Table 3.1; the smallest MAPE and MAE values were identified by using $\alpha = 0.8$ and $\beta = 1$.

Table 3.1 MAPE and MAE indices by using different parameters α and β

α	β	MAPE (%)	MAE (rad)
0.8	0.1	0.0601	0.0012
0.9	0.9	0.0723	0.0019
0.5	0.5	0.0994	0.0059
0.1	0.1	0.7245	0.0460
0.1	0.9	6.39	0.1934

The performance of the TSE with the parameters selected before is evaluated over the time using the MAPE (k) and MAE (k) indices. The accuracy of the estimated magnitude and phase angle for the voltages is relatively low, except at $t = 5$ s when the fault is applied as shown in Figure 3.2 and Figure 3.3. Nevertheless, the estimated values are very similar to the true values as shown in Figure 3.4 and Figure 3.5 for the phase angle and magnitude of the voltage at bus 6, which is near to the bus where the fault was applied.

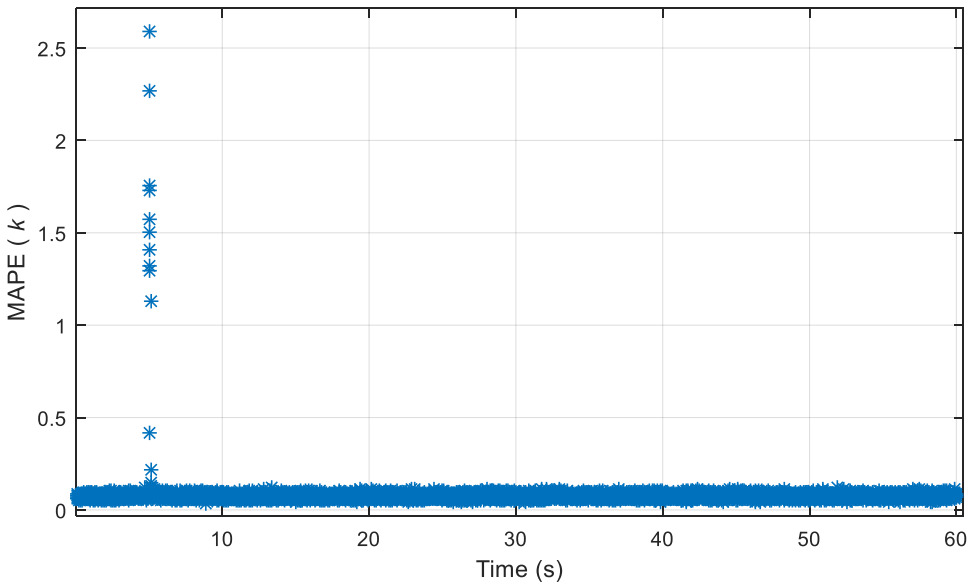

Figure 3.2 MAPE (k) index for the estimated magnitude of the voltages in the test bed system.

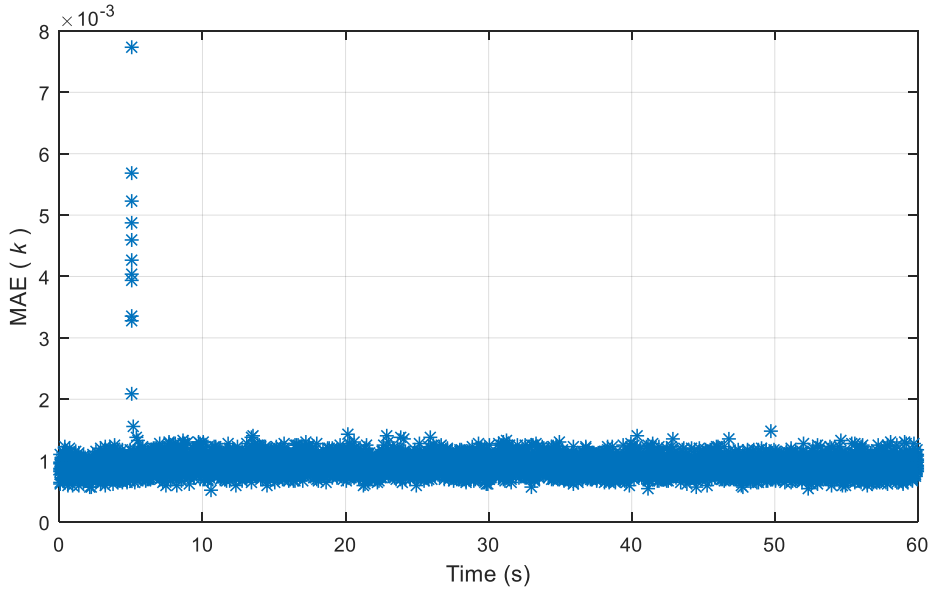

Figure 3.3 MAE (k) index for the estimated magnitude of the voltages in the test bed system.

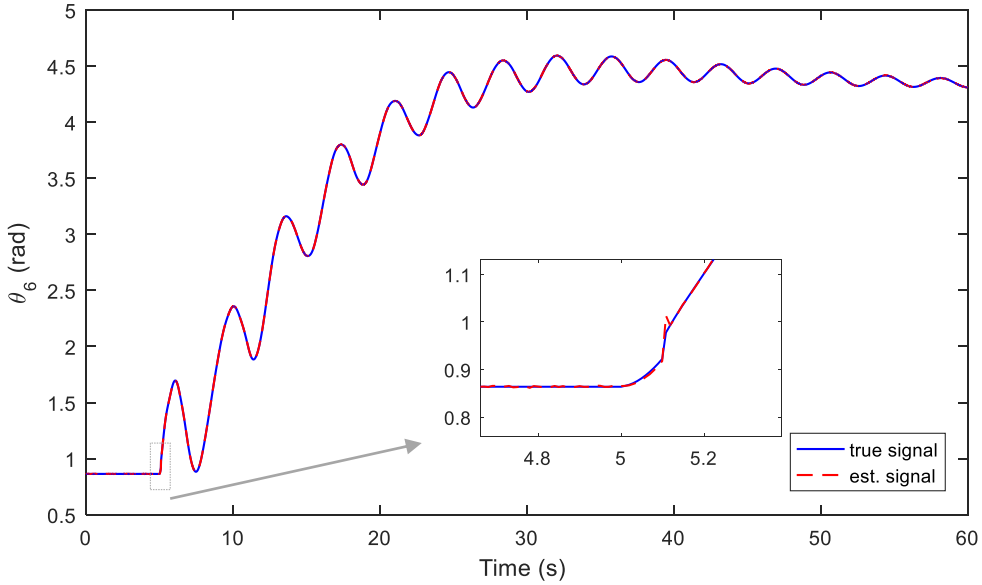

Figure 3.4 True and estimated signal for the phase angle of the voltage at bus 6

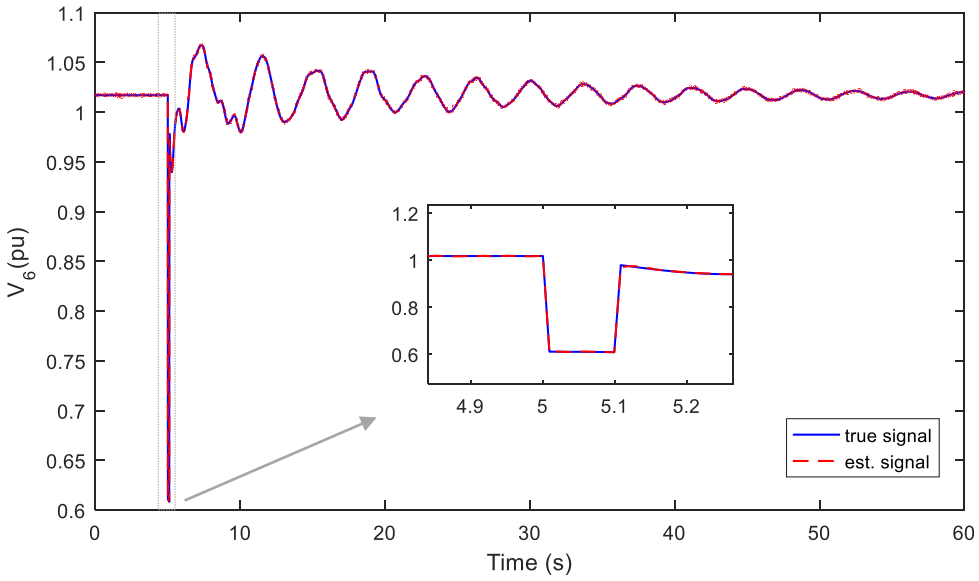

Figure 3.5 True and estimated signal for the magnitude of the voltage at bus 6

The matrices involved in the EKF algorithm for the test bed system are quite sparse as shown in Figure 3.6 and Figure 3.7, where the matrices $\boldsymbol{H}_k$ and $\left(\boldsymbol{H}_k \boldsymbol{P}_k^- \boldsymbol{H}_k^T + \boldsymbol{R}_k\right)$ are plotted, respectively, by way of example.

$[\boldsymbol{H}_k]_{304\times290}$

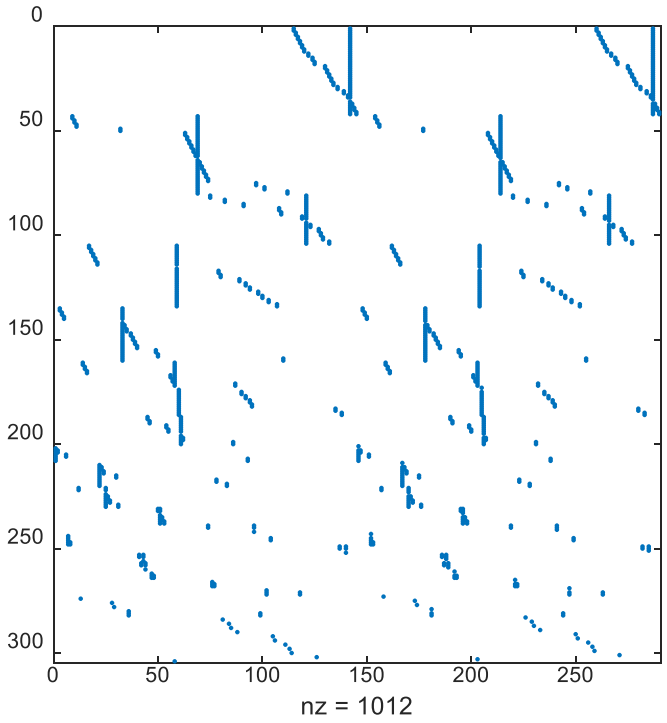

Figure 3.6 Sparse matrix $\boldsymbol{H}_k$ involved in the Kalman filter algorithm

$\left[\boldsymbol{H}_k\boldsymbol{P}_k^{-}\boldsymbol{H}_k^{T}+\boldsymbol{R}_k\right]_{304\times304}$

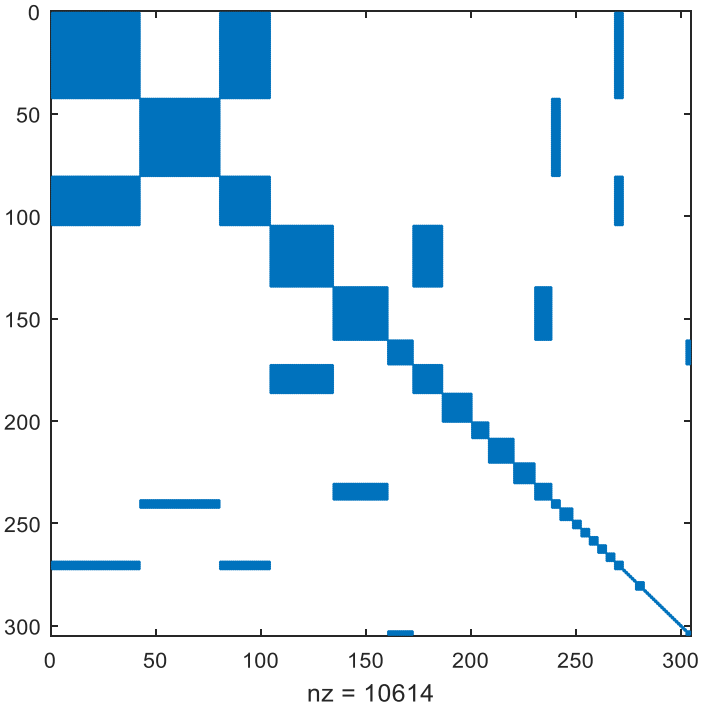

Figure 3.7 Sparse matrix before to applying its matrix inverse operation required for the computation of gain matrix of the Kalman filter algorithm

To assess the BDD represented in (3.26), a bad datum of magnitude +0.01 p.u. is introduced in the measurement $I_{PMU\ 69\text{-}63}$, at time t = 20 s, as illustrated in Figure 3.8. The threshold value associated with this measurement is set to be $\lambda_{\max} = 2$. From Figure 3.9, the BDD handles the bad datum appropriately under 500 Monte Carlo simulations. The bad datum identified at t = 5 s is considered a large disturbance because of the additional simultaneous presence of bad data in other measurements, e.g. the PMU signal $\theta_{PMU,\ 7}$ shown in Figure 3.10.

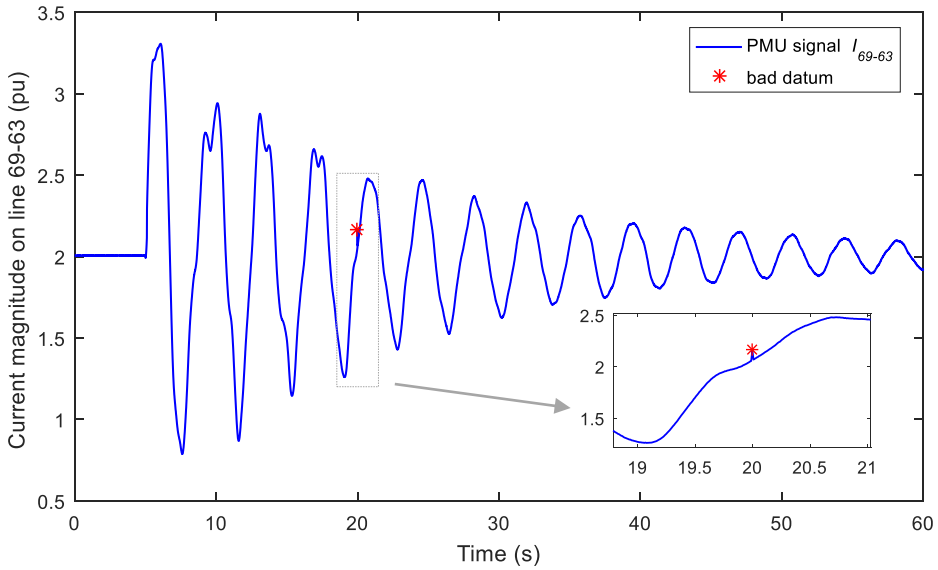

Figure 3.8 Measurement $I_{PMU\ 69\text{-}63}$ with bad datum

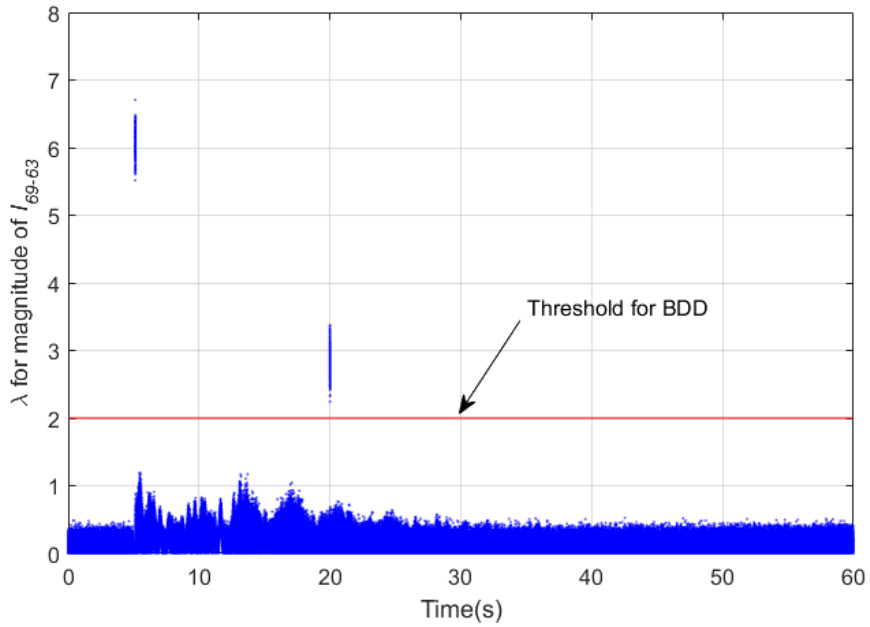

Figure 3.9 Identification of a bad datum in the signal $I_{PMU\ 69\text{-}63}$ by the BDD at t =20 s under 500 simulations.

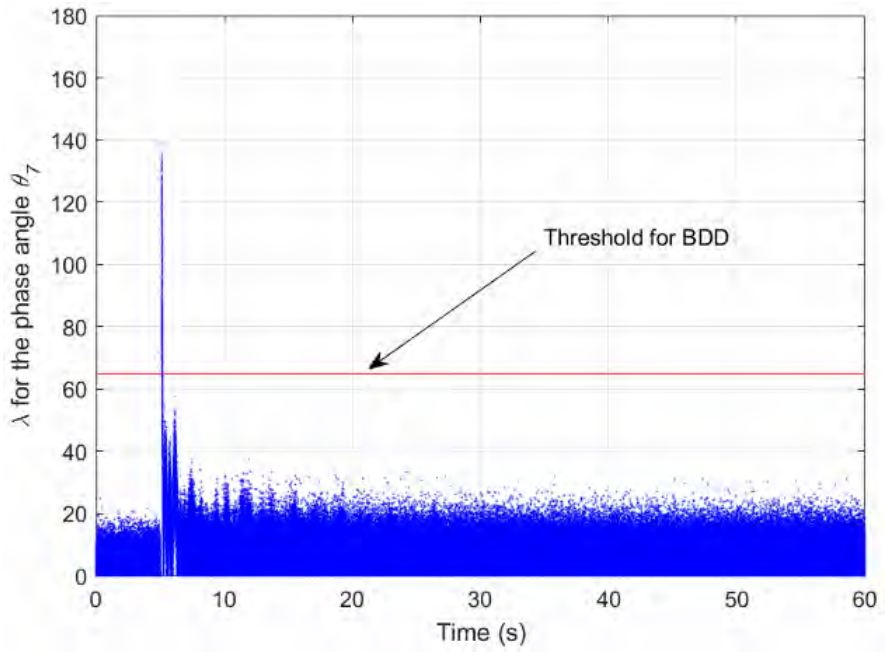

Figure 3.10 Identification of a large disturbance in the signal $\theta_{\text{PMU }7}$ at t=5 s under 500 simulations.

3.5 DSE versus TSE

Since the introduction of the SE in the late 1960s, several kinds of estimators suitable for following the system's dynamic changes were proposed in the power system literature [51], [65], [66], [67] . These estimators can be broadly categorized as dynamic state estimators (DSE), TSE and forecasting-aided state estimators (FASE). Because of the dynamic model utilized in the SE or the types of variables to be estimated [68], researchers sometimes have used these terms interchangeably. In this work, these estimators are classified according to state variables (quantities) to be estimated. Hence, dynamic variables such as the rotor angle or speed deviation of the synchronous machine are estimated by the DSE; on the other hand, the dynamic changes of algebraic variables such as the magnitude and phase angle of nodal voltages are estimated over time by the TSE.

A basic classification of the main estimators based on the PMUs measurements is shown in Figure 3.11. The states of several dynamic devices of the power system can be estimated by a centralized DSE [69], which requires the network transmission's model, the models of dynamic devices, as well as measurements from the PMUs located at different buses of the system. In a large-scale power system, the implementation of this estimator is infeasible because of the computational burden. The states of a dynamic device can be estimated by means of a decentralized DSE [70] that uses a dynamic model associated with the physical component and the PMUs' signals at the bus connected to the network. A linear state estimation [71] may be used as a TSE by employing a linear model for the synchronized measurements; in this case, the algorithm is similar to WLS method.

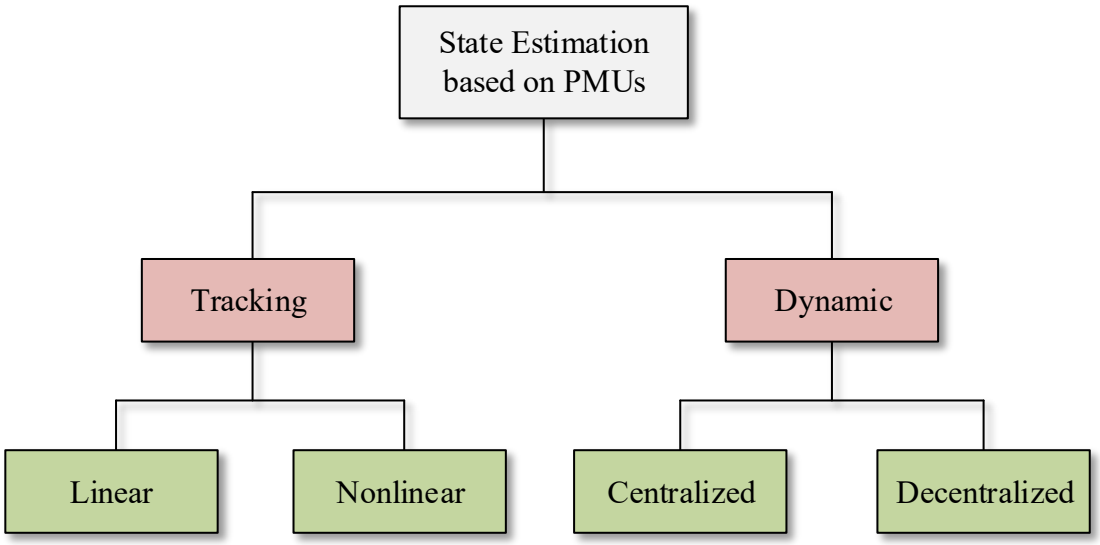

Figure 3.11 Basic classification of estimators based on the PMUs measurements

To complement the information mentioned in this chapter's introduction regarding the SE's vital role in the modern EMS, the tracking of the network state at levels of milliseconds may open up possibilities of extending and/or ensuring the operation of the typical applications based on PMUs [41], [72], including those below.

- Wide-area situational awareness
- Phase angle and grid stress monitoring
- Ambient oscillations' analysis
- Oscillation detection
- Islanding detection
- Generation and load trip detection
- Automated event analyzer
- Intelligent alarming

In the context of the critical low frequency oscillations (LFOs), the determination of SDCs by using estimated generator's dynamic variables from a decentralized DSE has been proposed in [15], [16], and [14]. Based on the analysis presented in the previous chapter about modal characteristics of the inter-area oscillations, a stabilizing signal based on the estimated algebraic variables by the nonlinear TSE using the EKF method is employed in this dissertation.

3.6 TSE-based control signal

Based on the information mentioned above, the fundamental concept of the proposal for the power oscillations' control is shown in Figure 3.12. In this case, the dynamic behavior of algebraic variables is obtained by a TSE, which is also used to obtain the value of the supplementary damping control signal as presented in Section 2.6. To achieve the latter goal, the transmission system parameters as well as the phasor measurements of nodal voltages and branch currents are used in the TSE to obtain the control signal $\hat{z}$. This wide-area signal together with a local signal z (PMU measurement at SVC bus) are applied to the supplementary control of an SVC.

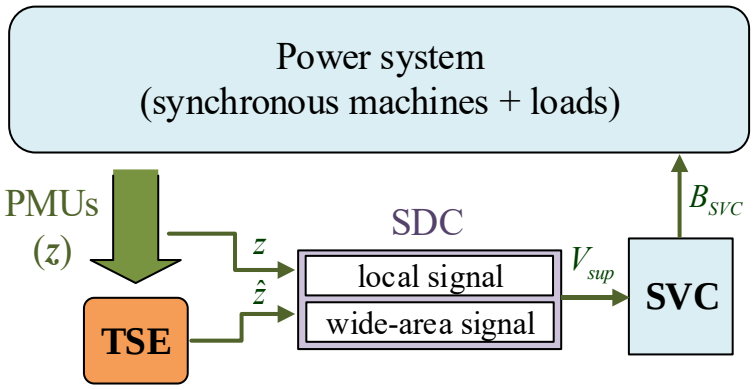

Figure 3.12 A simplified conceptual diagram of the stability enhancement, using an SVC with a robust SDC assisted by the TSE

Large communication delays, as well as synchronization errors in the wide-area signals [10], may have a negative impact on the efficiency of the proposed method. In this sense, a fixed communication delay of 100 ms is assumed in the application of the SDC. Note that the implementation of the TSE in practical systems may require dedicated communications' links to diminish the delays of measurements.

By following the procedure for selecting the required control signal for the SDC, as prevously described, and by applying the EKF method mathematically represented for each discrete time k by the set of equations (3.13) through (3.18), the magnitude of branch current $\hat{I}_{pq,k}$ is computed as

$$\hat{I}_{pq,k}(\hat{\boldsymbol{x}}_k) = \left| \frac{\hat{V}_{p,k}\angle\hat{\theta}_{p,k} - \hat{V}_{q,k}\angle\hat{\theta}_{q,k}}{z_{pq}} \right|, \\ = \hat{z}_k(\hat{\boldsymbol{x}}_k) \tag{3.29}$$

where z_{pq} is the primitive series impedance of the element between the buses p and q.

Control signal for the IEEE 50-generator system

Before applying the proposed method to the test bed system, the identified best signal for the wide-area control signal $I_{63\text{-}66}$ is estimated by using the expression (3.29) while considering the previous scenario of the test bed system. Figure 3.13 clearly shows that the dynamic behavior of the estimated signal $\hat{I}_{63-66}$ is very similar to the true signal I_{63-66} that has been obtained from a time-domain simulation.

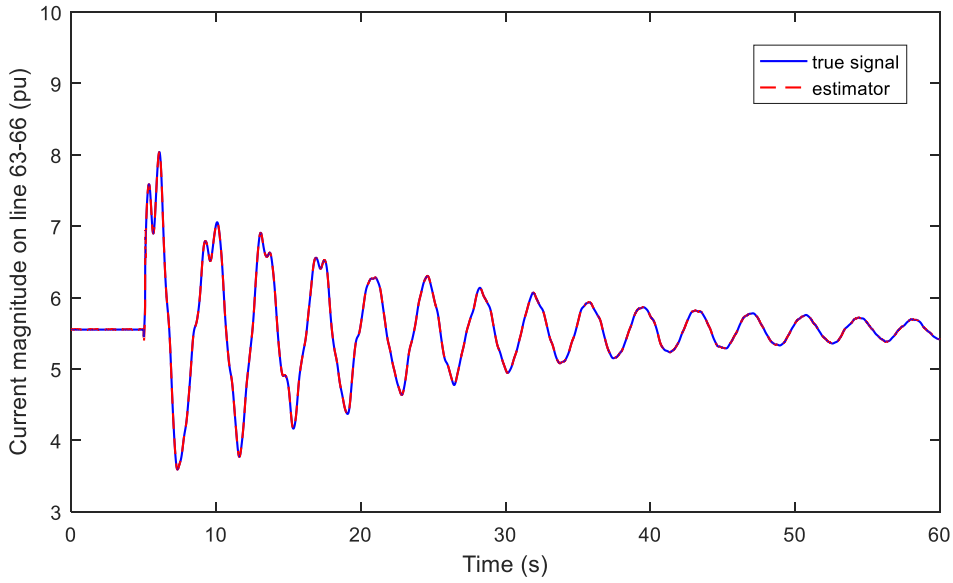

Figure 3.13 Comparison of the estimated and true control signal $I_{63\text{-}66}$

3.7 Summary

The mathematical formulation of the TSE based on PMUs has been presented in this chapter. The EKF technique for the state estimation of a nonlinear system was applied to the IEEE 50-generator system considering 304 synchronized measurements. The dynamic model of the system employed in the estimator, which has been utilized in power systems' literature

for the estimation of quasi-stationary systems, was used as the prediction model. The estimated state obtained by the TSE for the test bed system under a large disturbance was very similar to the true state over time. The relatively low value for the MAPE and MAE indices regarding the scenario analyzed confirms the performance of the estimator.

Regarding the presence of a corrupted value in the measurements, the BDD identified the bad datum in the 500 Monte Carlo simulations.

The description of the novel control scheme for power oscillations' damping by means of the TSE and SDC has been presented in this chapter. A stabilizing signal was obtained by the estimator; the dynamic behavior of the estimated signal is very similar to that associated with the true signal.

Chapter 4

Case studies

4.1 Introduction

To implement the proposed closed-loop control scheme, the PMU-based TSE approach is first coded as a dynamic-link library (DLL) file by using C/C++ programming. This file is then included as a user defined model (UDM) function in the DSATools software [73]. Based on this development, the proposed method is applied to the test bed system, and its performance is evaluated by conducting nonlinear time-domain simulations considering several scenarios by using the TSAT software. An exponential function is adopted in the UDM to model the time delay associated with the estimated signal in the SDC in the simulations.

4.2 Results of the proposed method for IEEE 50-generator system

The procedures presented in previous chapters are used to identify the best candidate stabilizing signals for the SDC and to estimate the selected wide-area signal. In this context, the wide-area signal $\hat{z}= \hat{I}_{63\text{-}66}$ estimated from the TSE and the local signal $z = I_{44\text{-}45}$ obtained from the PMU are added to the SVC of the test bed system considering the scenario described in Section 2.4. To compare the results, the following cases are considered: (A) a SVC

"without SDC" is utilized; (B) the SDC uses the required wide-area signal or "true signal;" and (C) the proposed TSE-based method is used as previously outlined.

Two variables related to the generators that participate the most in the critical mode are monitored to show the damping enhancement. The two monitored variables are the relative rotor angle of generator #93 , with the rotor #145 is the reference angle, and the active power output of generator #139.

The results of damping control for cases A, B and C are illustrated in Figure 4.1 and Figure 4.2. The proposed method shows a satisfactory performance. The SDC significantly improves the damping afforded by the PSS in the critical mode. The trajectories of the monitored variables for the cases B and C are very similar even when the dynamic system is different in both cases because of the control signal not being the same. The error of the estimated signal in the time evolution does not affect the controller performance.

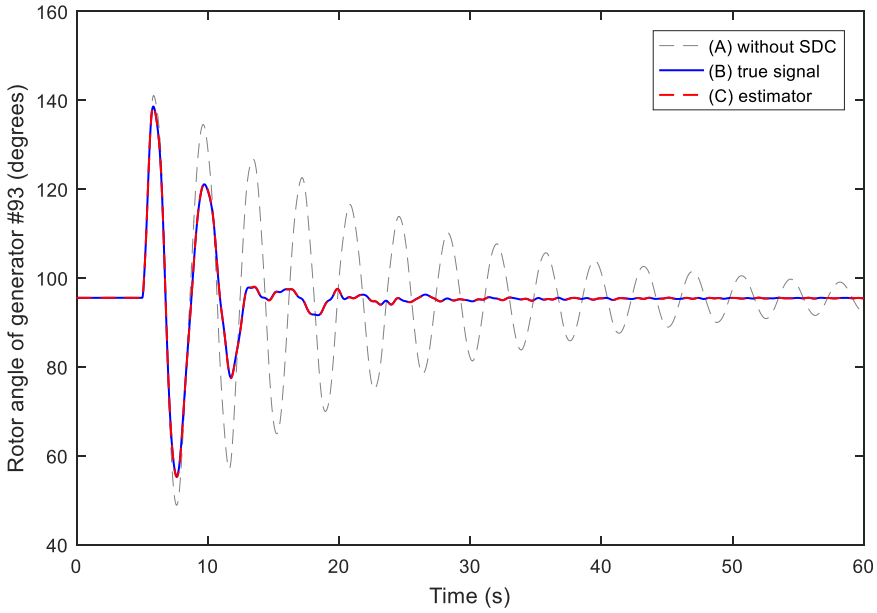

Figure 4.1 Response of rotor angle of generator #93 (Area 1) to the large disturbance (2×1700 MW) for the cases A, B and C.

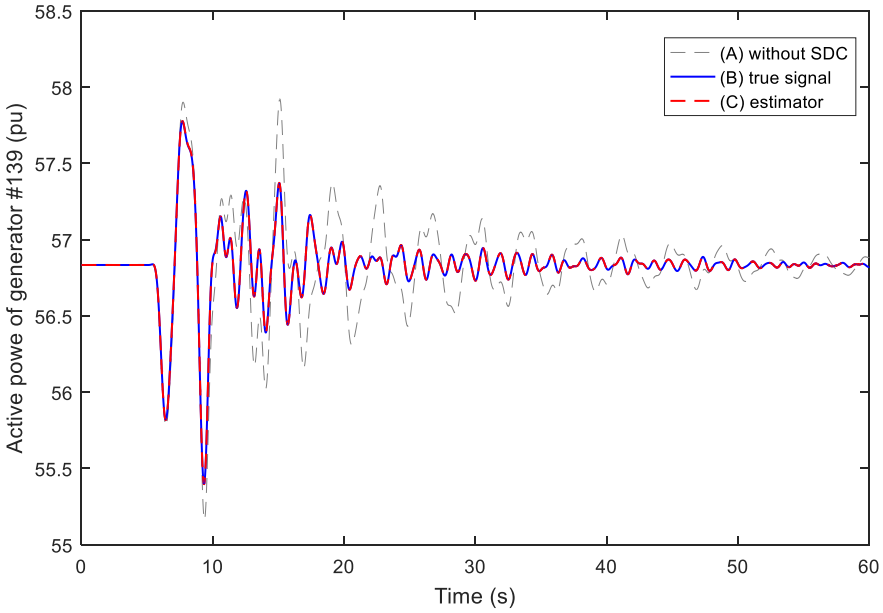

Figure 4.2 Response of active power of generator #139 (Area 2) to the large disturbance (2×1700 MW) for cases A, B and C.

The TSE provides the wide-area signal required by the controller as shown in Figure 4.3. The estimated current line magnitude at line 63-66 is similar to the true signal; however, there is a small difference of a few milliseconds after the fault is cleared. Note that this error in the estimated signal does not significantly affect the response of the SDC. The dynamics of the monitored variable in case A reflect the lack of damping control provided by the SVC alone.

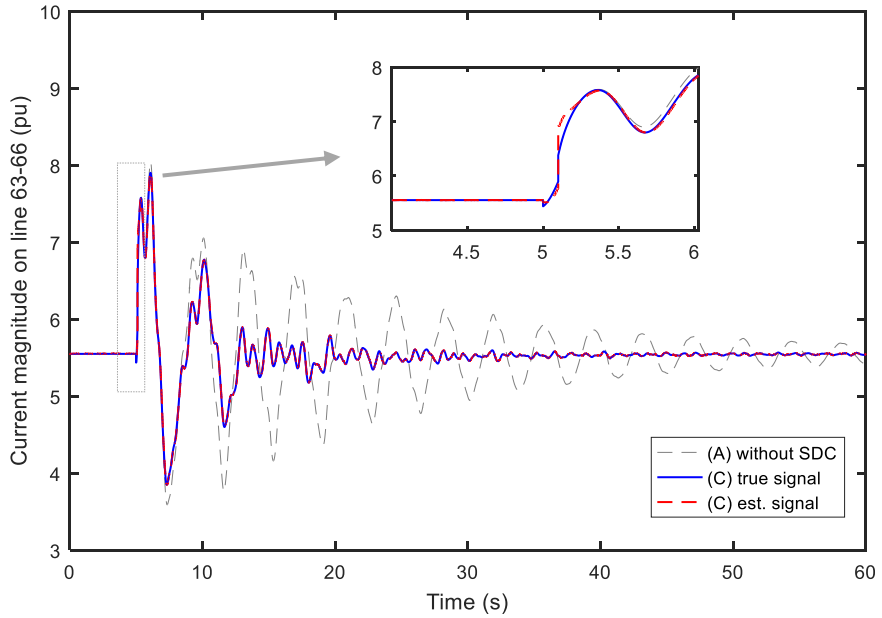

Figure 4.3 . Response of the SDC's control signal | $I_{63\text{-}66}$ | to the large disturbance (2×1700 MW) for cases A and C.

Figure 4.4 shows the output of the supplementary controller of the SVC and reflects the control effort during the disturbance. The dynamics of the bounded output signal for cases B and C are very similar. The estimator and the SDC provide the adequate supplementary signal V_{sup} to the SVC for damping system oscillations for large disturbances.

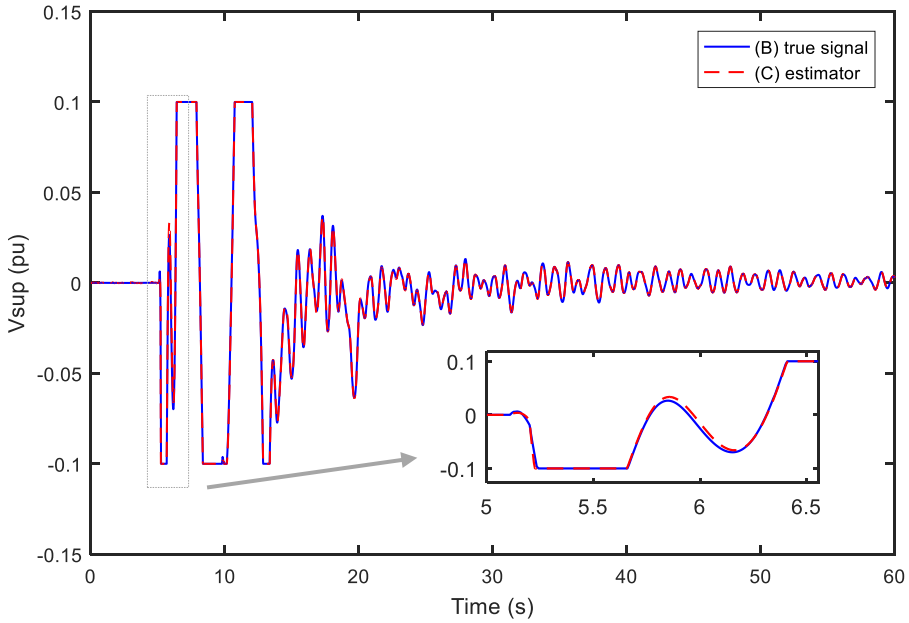

Figure 4.4 . Response of the output signal of SDC to the large disturbance (2×1700 MW) for cases B and C.

4.3 Robustness of the proposed method to different operating conditions

To illustrate the effectiveness of the proposed control scheme under different operating conditions, in addition to the fault location, a new scenario is considered. At the operating condition (2x1800 MW), a three-phase fault is applied to bus #33 for six cycles (0.1s) and then removed. The PMU configuration of the previous scenario is considered as well as the parameters and initial conditions of the estimator.

The response of the system to the large disturbance for cases A, B and C is illustrated in Figure 4.5 and Figure 4.6. The trajectory of the monitored variables shows similar behavior

for cases B and C. The SDC with the estimator extends the stability limit beyond that obtained with only PSSs included.

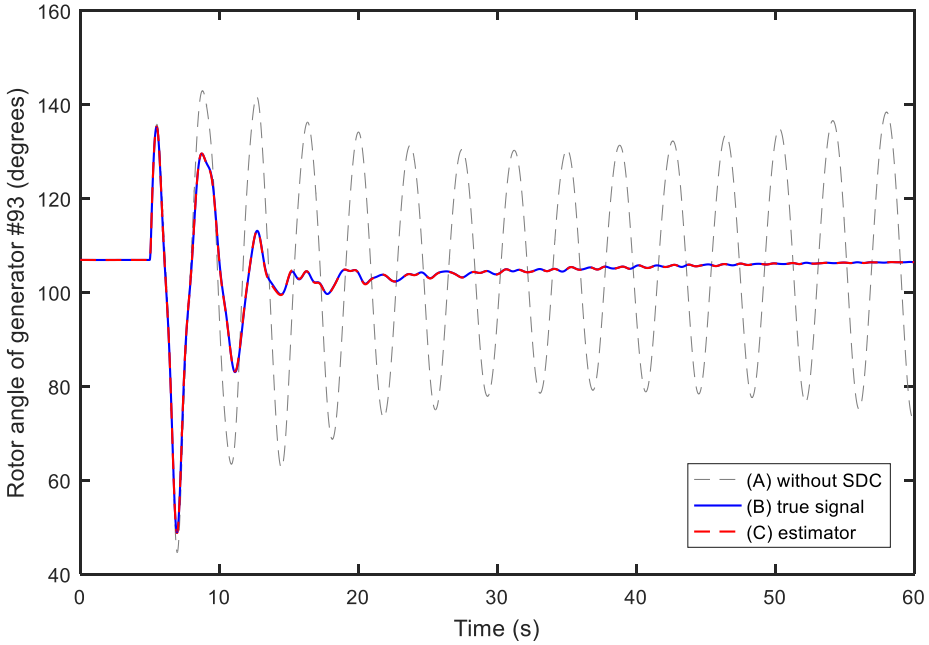

Figure 4.5 . Response of rotor angle of generator #93 (Area 1) to the large disturbance (2×1800 MW) for cases A, B and C.

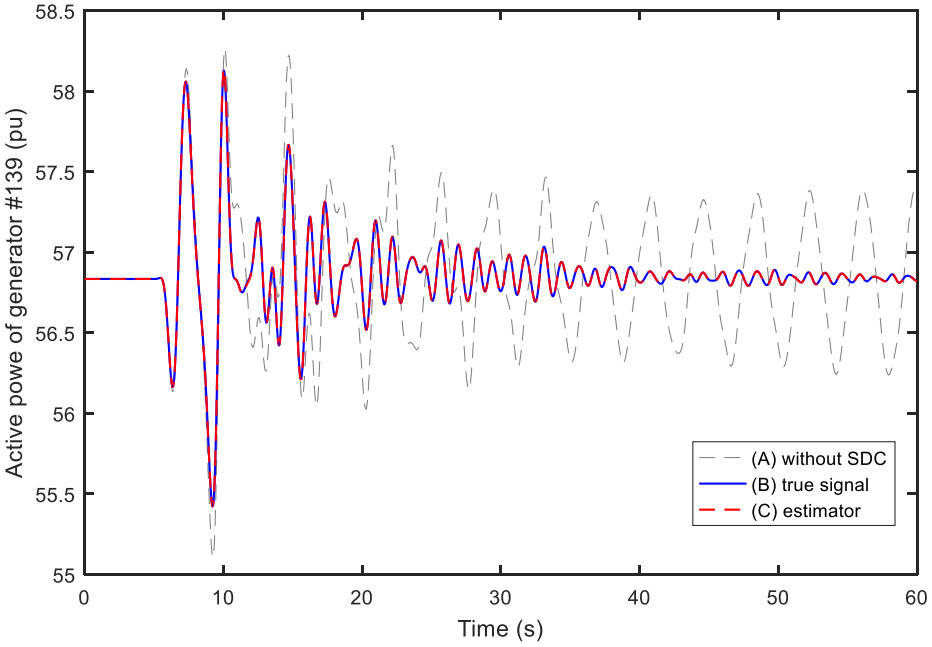

Figure 4.6 . Response of active power of generator #139 (Area 2) to the large disturbance (2×1800 MW) for cases A, B and C.

As shown in Figure 4.7, the estimated control signal follows the actual signal in case C quite closely to the response of the system during the event except during the fault. Nevertheless, this estimation error does not affect the performance of the damping control.

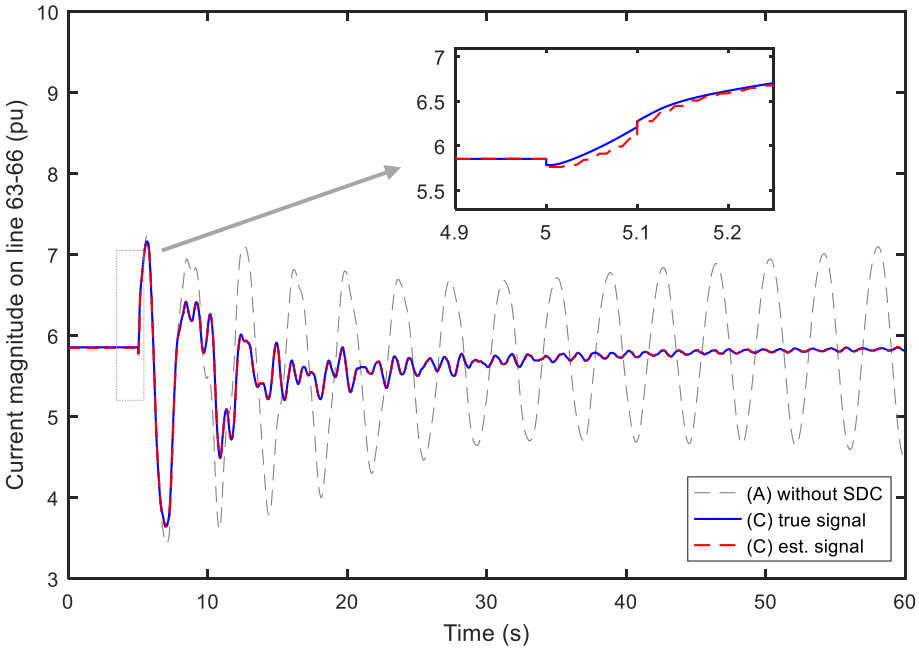

Figure 4.7 . Response of SDC's control signal | $I_{63\text{-}66}$ | to the disturbance (2×1800 MW) for cases A and C.

Lastly, the performance of the proposed approach is newly quantified by considering two operative scenarios where a three phase fault is applied at buses #67 and #142, respectively. In both scenarios, the fault is cleared after six cycles of its occurrence without tripping transmission lines. The oscillations associated with the rotor angle of generator #93 are shown in Figure 4.8 and Figure 4.9 for each scenario, respectively. The results clearly show the effectiveness of the proposed approach for damping out the rotor angle oscillations, which is not the case when the SDC is not considered in the case studies.

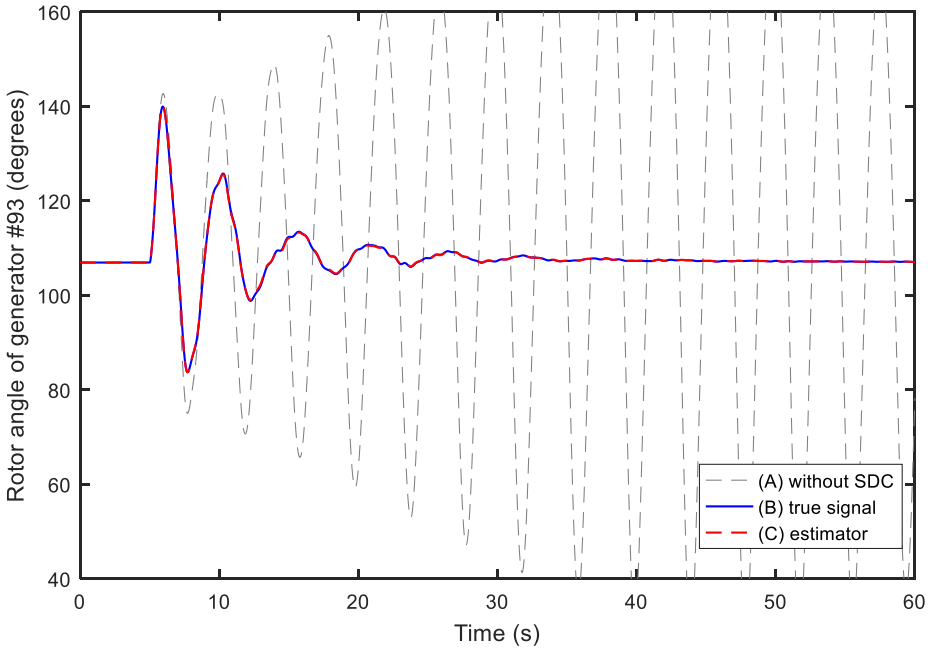

Figure 4.8 Rotor angle oscillations of generator #93 (Area 1) for a three-phase fault at bus #67.

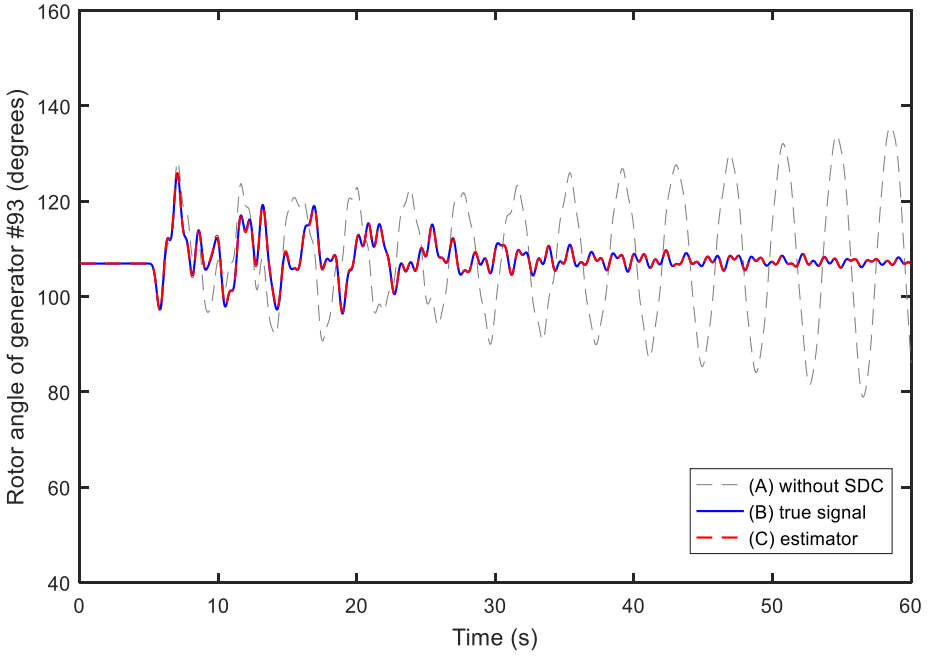

Figure 4.9 Rotor angle oscillations of generator #93 (Area 1) for a three-phase fault at bus #142.

4.4 Sensitivity to noise

To assess the impact of PMU quality in the proposed method, the white Gaussian noise in the set of measurements is increased. The system of the previous scenario is compared when $\sigma = 0.01$ (p.u.) and $\sigma = 0.05$ (p.u.). The simulation results for case C are shown in Figure 4.10. Furthermore, the power system damping enhancement is not affected by the level of noise in the measurements, and the estimator is still able to provide a control signal with acceptable accuracy. As is shown in Figure 4.11, the plot of estimated signals for case C almost coincides with the true signal in case B.

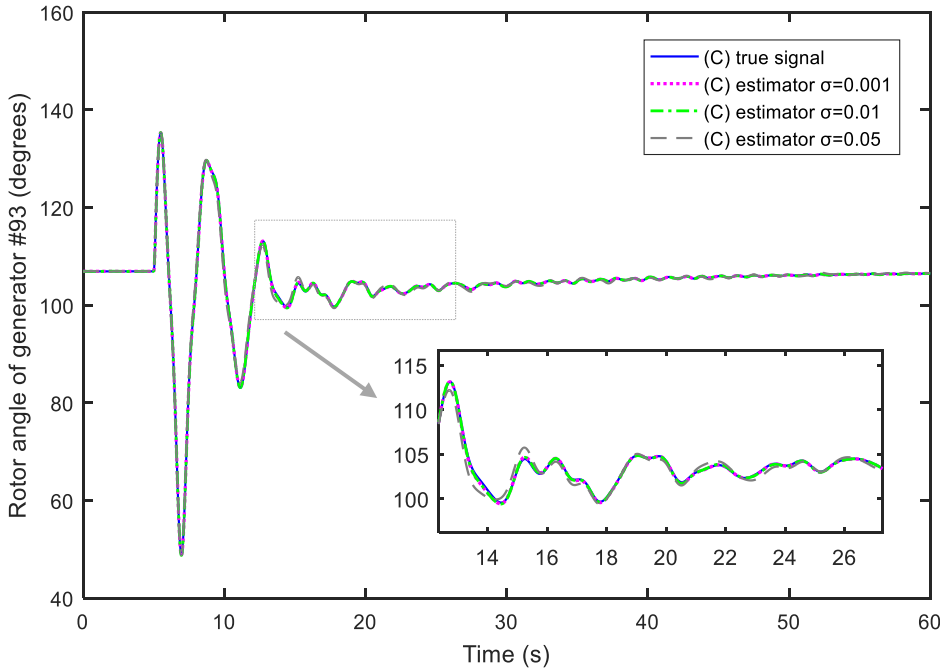

Figure 4.10 Response of rotor angle of generator #93 (Area 1) to the large disturbance (2×1800 MW) for case C, by considering different levels of noise in PMU signals.

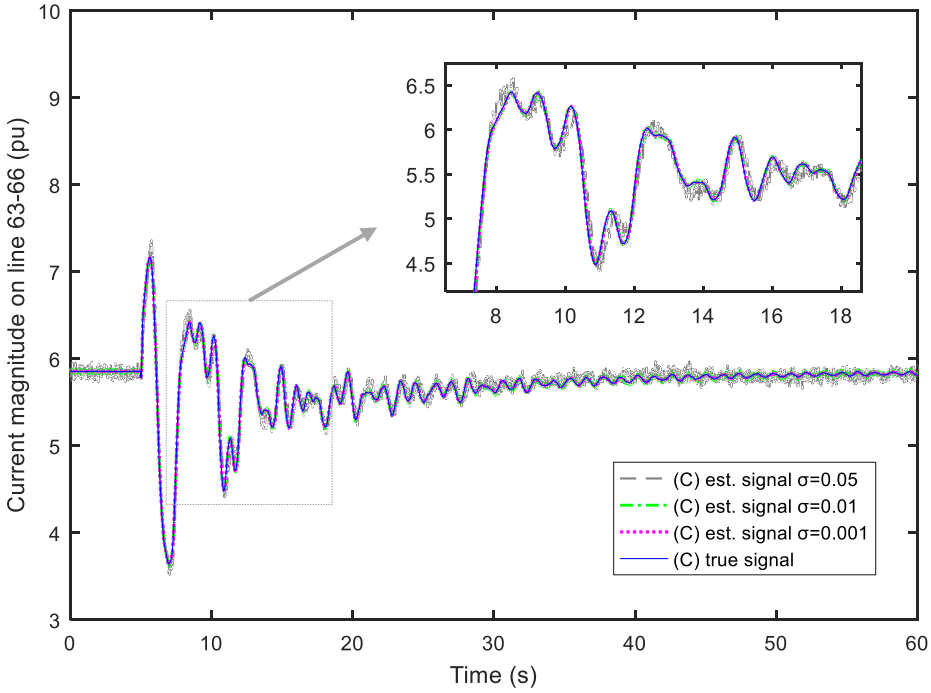

Figure 4.11 Response of SDC's control signal | $I_{63\text{-}66}$ | to the disturbance (2×1800 MW) for case C by considering different levels of noise in PMU signals.

The TSE formulation given by (3.13) to (3.18) utilizes the previous information of the state vector and covariance matrix in order to estimate the current system state. In this context, the EKF is formulated by assuming that the sequences $\boldsymbol{w}_{k-1}$ and $\boldsymbol{\varepsilon}_k$ are Gaussian noise independent between each other. In a real power system, however, the behavior of the dynamic model is highly correlated. Thus, the correlated noise can impact the proposed method. To illustrate the difference between white Gaussian noise (WGN) and pink noise (correlated noise), sequences of these noises are shown in Figure 4.12.

The simulation reported in this section has been repeated by considering the correlation in the noise. In this case, a pink noise with a standard deviation of σ = 0.01 p.u. has been added to all measurements. The resulting dynamic profiles for the rotor angle oscillations of generator #93 and for the estimated control signal $I_{63\text{-}66}$ are shown in Figure 4.13 and Figure 4.14, respectively. Note that the dynamic behavior of these variables follows that obtained by using the true signal, case B, and the one computed by using measurements with WGN, case C.

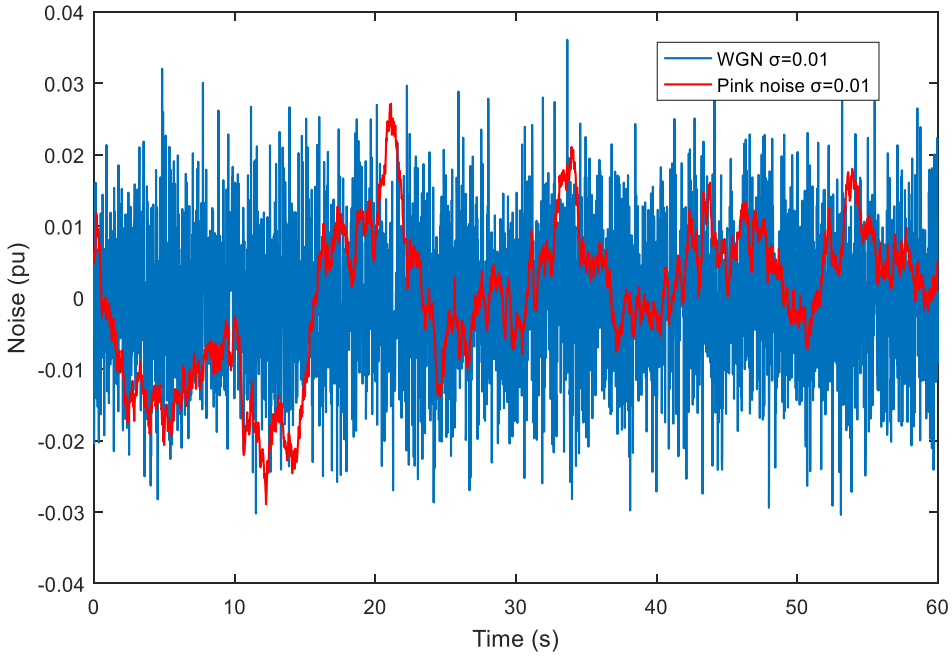

Figure 4.12 WGN sequence and pink noise sequence with standard deviation $\sigma = 0.01$ (p.u.).

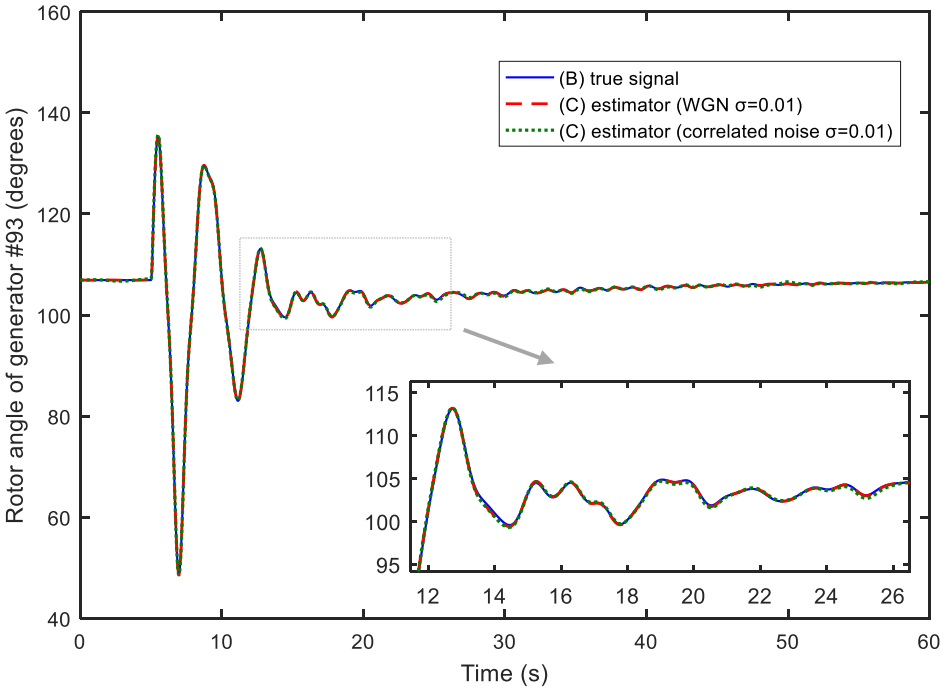

Figure 4.13 Response of rotor angle of generator #93 (Area 1) to the large disturbance (2×1800 MW) for cases B and C, by considering correlated noise in PMU signals.

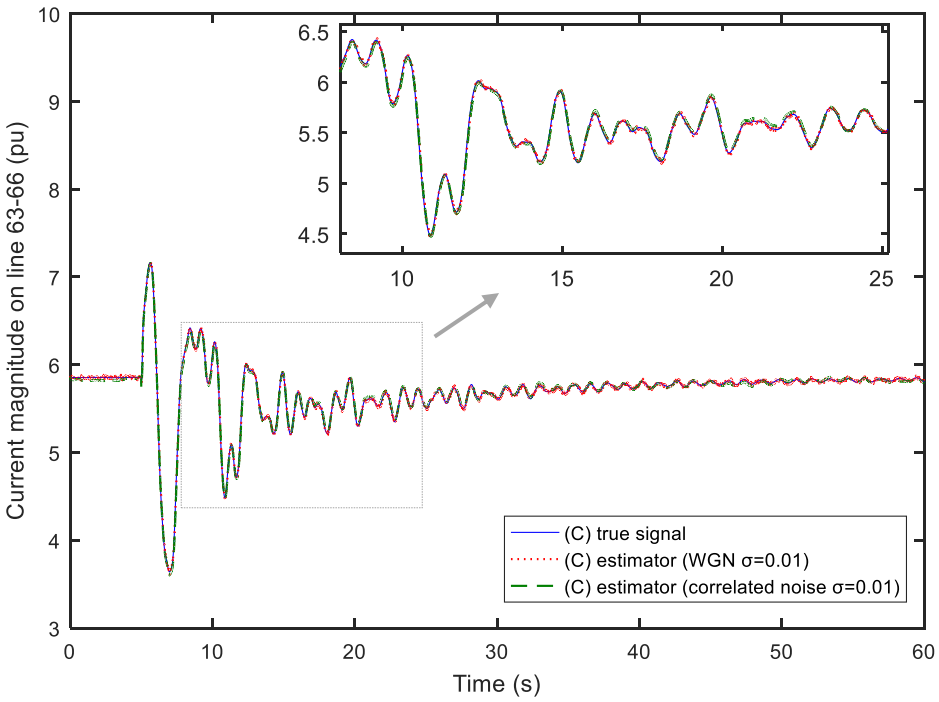

Figure 4.14 Response of SDC's control signal | $I_{63\text{-}66}$ | to the disturbance (2×1800 MW) for case C by considering correlated noise in PMU signals.

4.5 An alternative control signal

By following the procedure presented in Chapter 2 to find an unconventional stabilizing signal for the SDC, the identified signal $\hat{z} = \theta_{93}+\theta_{110}-\theta_{137}-\theta_{140}$ is employed as the wide-area signal to extend the damping control of the power system.

To validate the results of the small-signal analysis presented in Section 2.4, a time-domain simulation is applied to the previous scenario by considering WGN with a zero mean and a standard deviation $\sigma = 0.01$ (p.u.) in PMUs. The response of the system for cases A, B and C is illustrated in Figure 4.15 and Figure 4.16; the trajectory of the dynamic system in case C using an alternative control signal shows a satisfactory damping control that is very similar to the system in case B. The output of the supplementary controller for cases B and C are shown in Figure 4.17. A similar behavior for the two cases can be observed at the beginning of the disturbance, and less control effort is required with the proposed supplementary damping signal at the end of system stabilization.

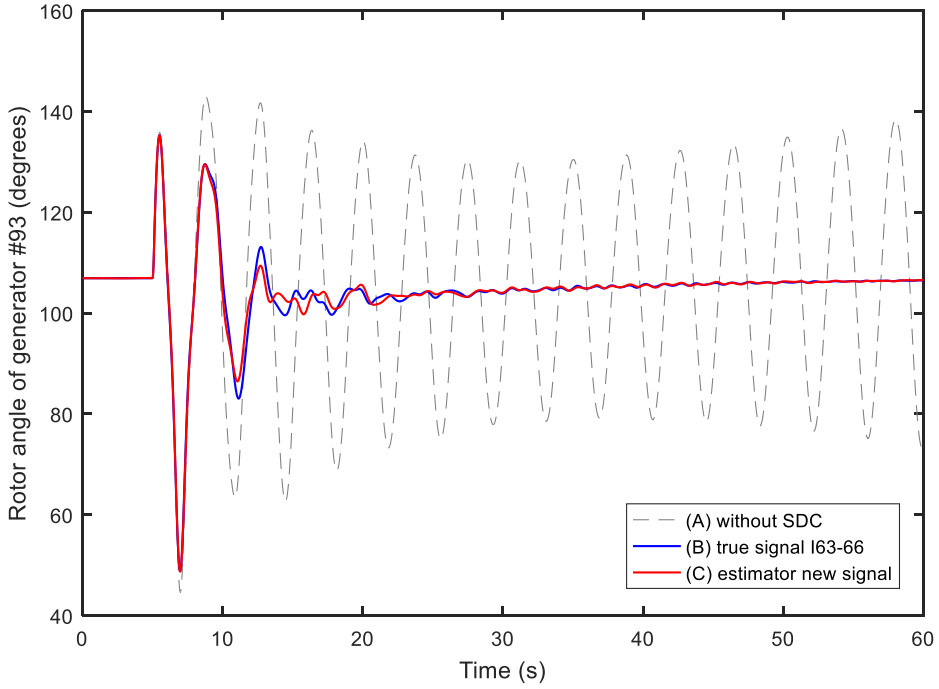

Figure 4.15 Response of rotor angle of generator #93 (Area 1) to the large disturbance (2×1800 MW) for cases A, B and C.

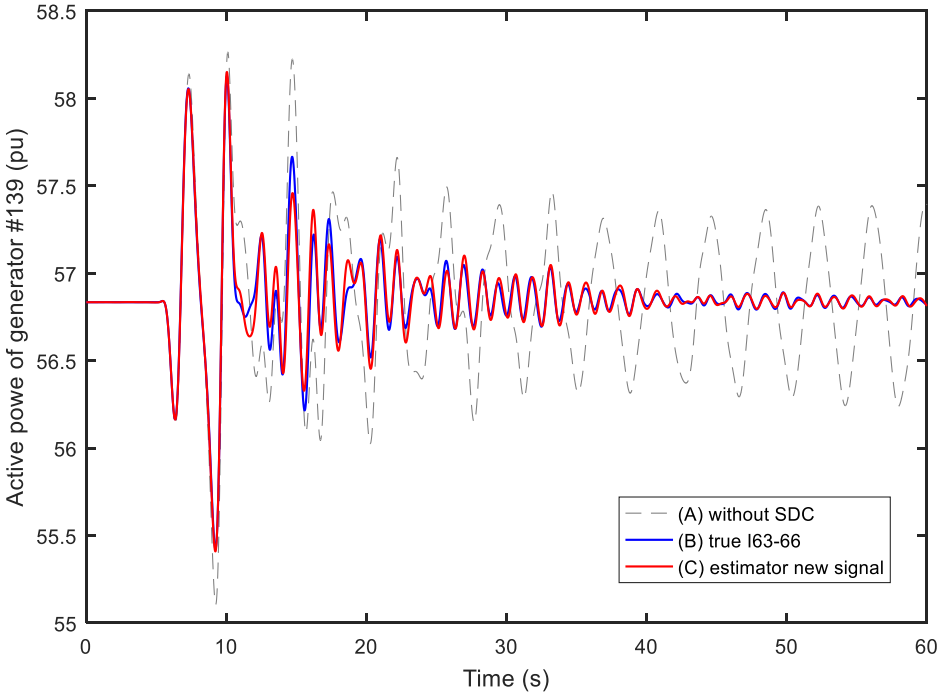

Figure 4.16 Response of active power of generator #139 (Area 2) to the large disturbance (2×1800 MW) for cases A, B and C.

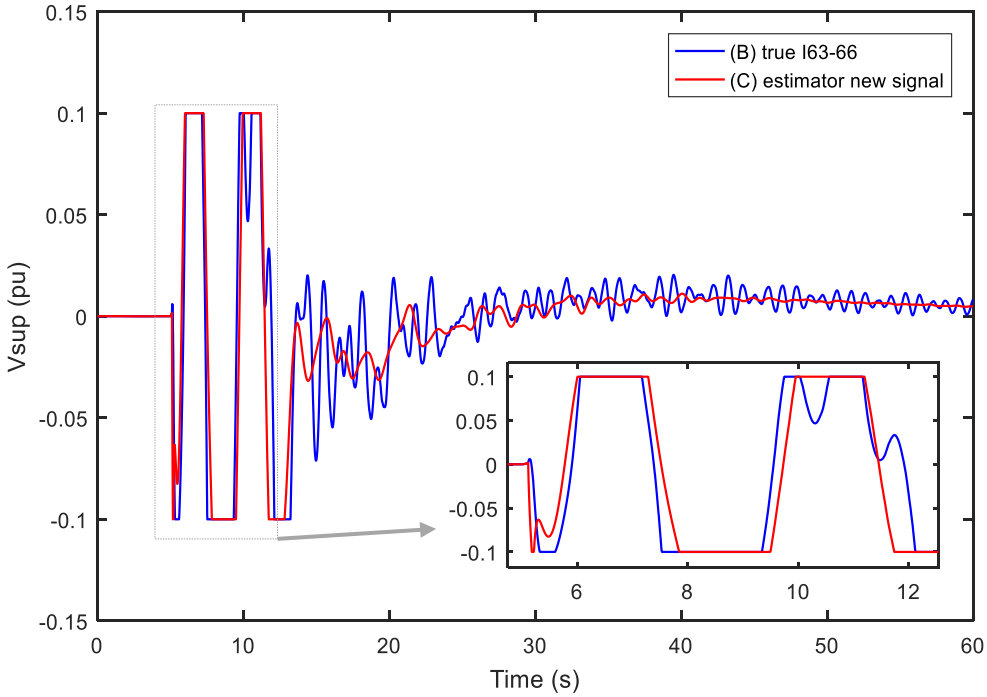

Figure 4.17 Response of output signal of SDC to the large disturbance (2×1800 MW) for cases B and C.

As the supplementary signal V_{sup} in the FACTS device stabilizes the disturbance, the primary control is not neglected. The response of the SVC terminal voltage for cases A, B and C is illustrated in Figure 4.18, where the performance of the SVC with the proposed scheme is accomplished satisfactorily. The lack of supplementary control by the SVC in response to the disturbance is illustrated by the trajectory of case A.

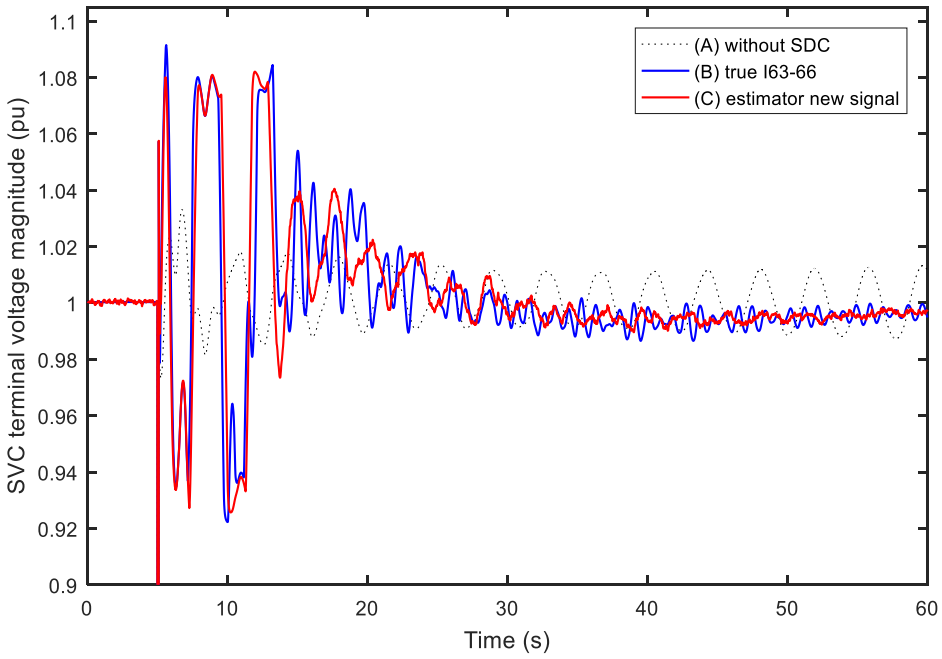

Figure 4.18 Response of SVC terminal voltage magnitude to the large disturbance (2×1800 MW) for cases A, B and C.

In this scenario, an alternative control signal based on different variables of the power system is estimated, opening the possibility of using this control scheme when the original required signal cannot be obtained because of a change in the PMU configuration (e.g., by tripping the line 63-66 of the test bed system. In addition, the original required signal $I_{63\text{-}66}$ cannot be employed in the SDC).

4.6 Proposed approach vs conventional SDC

The results of the above section are compared to the ones obtained when the SVC uses a conventional damping controller, which employs the local signal z in a lag-lead phase compensation network. In the operating conditions of the test bed system, the optimal parameters of this controller are adjusted to smooth out the critical mode using SSAT. The model of the tuned SDC is shown in Figure 4.19. The eigenvalues associated with the critical mode are presented in Table 4.1.

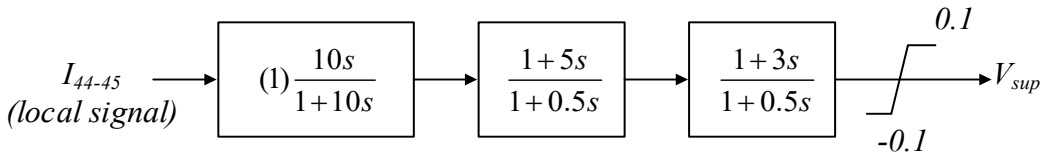

Figure 4.19 Model of conventional SDC tuned for the test bed system at the operating conditions 2x1800 MW.

Table 4.1 Comparison of damping ratio of the critical mode using the SVC without SDC utilized, the proposed method and a conventional SDC for the SVC

G93 & G110 (MW)	**PSS (no SDC)**	**PSS + SDC *(local and new signal)***	**PSS + conventional SDC *(local signal)***
2×1800	-3.01%@0.260 Hz	15.73%@0.215 Hz	9.64%@0.26 Hz

The results of the time-domain simulations are presented in Figure 4.20 and Figure 4.21; the proposed approach has a better performance than the typical solution used in practice for damping out power oscillations. Furthermore, the conclusion of the small-signal analysis is verified.

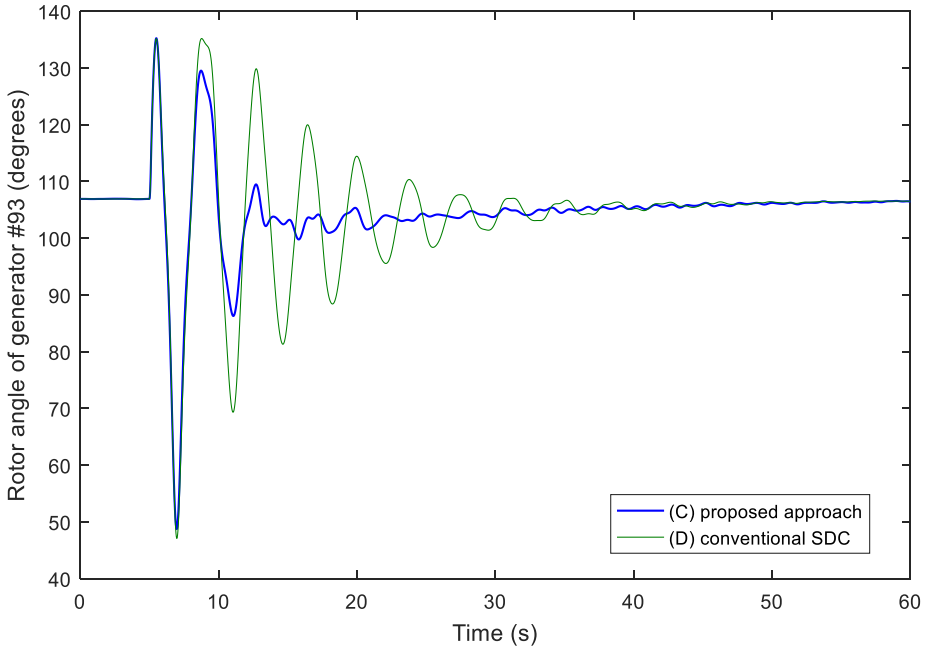

Figure 4.20 Response of rotor angle of generator #93 (Area 1) to the large disturbance (2×1800 MW) for cases C and D.

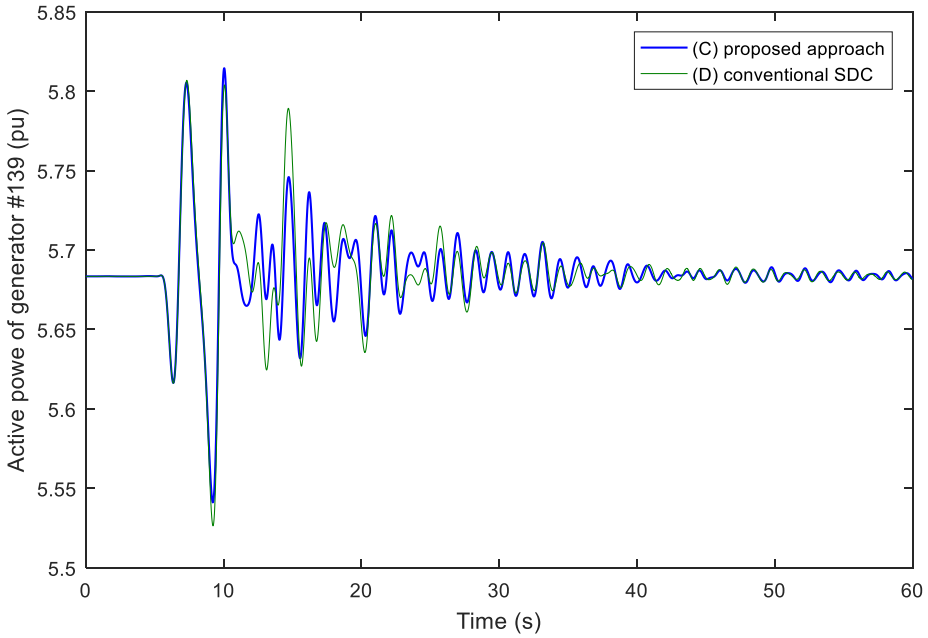

Figure 4.21 Response of active power of generator #139 (Area 2) to the large disturbance (2×1800 MW) for cases C and D.

4.7 Computational feasibility

The SDC signal of the SVC is required in real time. It is essential to examine the processing time per estimation step. Before integrating the algorithm in TSAT, it was tested in MATLAB R2015. This processing time is approximately 6 ms/step on a PC laptop with Intel Core™ i7-6820HQ CPU, 16 GB RAM and Windows 10 64-bit operating system. The software code optimization for large sparse matrices was not addressed in this work. Nevertheless, the time execution for the estimator is less than the PMU sampling time in the time simulation, thus illustrating the feasibility of scaling and applying the proposed method.

4.8 Application of the proposed method in a practical system

The results of the proposed method for the IEEE 50-generator system have been satisfactory under the analyzed scenarios. In addition to the assumption of a complete system's observability through the installed PMUs, the SVC of this test bed system was optimally located for power oscillations' damping control purposes. In practical systems,

some SVCs are installed at specific locations of the network for voltage support only, which implies that the controllability of the inter-area modes by using the proposed control scheme could not be ensured. For analyzing the feasibility of the proposal in a practical system, a representative model of the Mexican interconnected system (MIS) is analyzed in this section.

For the purpose of this work, the MIS model is composed of 5682 nodes, 349 machines, and 24 SVCs. The 400/230 kV transmission network, stretching from its interconnection with the United States of America to Central America, has a longitudinal configuration characterized by long transmission lines and remote generation sources.

The MIS is divided into seven regional transmission control areas referred to as north (N), northwest (NW), northeast (NE), southeastern (SE), western (W), central (C) and peninsular. The detailed description of this system is described in [20], [74], [75]. The operating conditions of the system are set up to satisfy a load demand of about 42000 MW.

In order to analyze the small-signal stability of the system, a complete modal analysis is performed by using the SSAT program. From the results, the main inter-area modes of oscillation are shown in Table 4.2. Note that the system presents a critical electromechanical mode at 0.381 Hz, where the machines in the north area oscillate against the machines in the southeastern area.

Table 4.2 Main inter-area modes of the MIS with its PSSs installed

Inter-area mode	Eigenvalues	Damping ratio @ frequency	Oscillation pattern
1	$-0.0929 \pm j\ 2.3990$	3.87% @ 0.381 Hz	N area vs. SE area
2	$-0.1912 \pm j\ 3.7013$	5.16% @ 0.589 Hz	Peninsular area vs. NE area
3	$-0.2895 \pm j\ 3.8641$	7.47% @ 0.615 Hz	NE vs. N

The mode shape associated with the critical oscillatory mode is presented in Figure 4.22; the largest right eigenvectors (magnitude) labeled as g1 and g2 are those vectors related to the generators involved in the inter-area mode; in this case, the machines embedded in the north area oscillate against the machines connected at the southeastern area. The vector g3 represents the dominant state (rotor angle or speed deviation of the machine) in the electromechanical mode: g3 is the state variable with major participation.

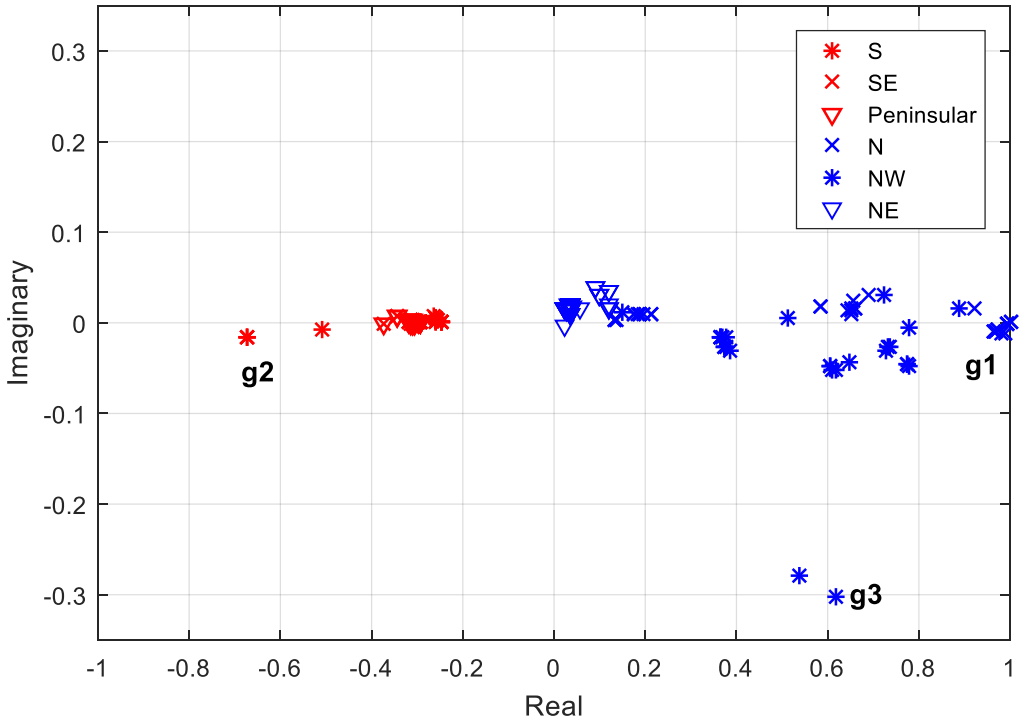

Figure 4.22 Mode shape for the critical mode at 0.381 (Hz).

To incorporate the damping control scheme based on the results provided by the TSE, the fundamental concept of the proposed method is modified to incorporate coordinated actions of multiple SVCs to improve the stability of the large-scale MIS system. For estimating the appropriate wide-area signals for the SDCs, the TSE can utilize a subset of all phasor measurements of the system as to not compromise the computational burden in the estimation process. The conceptual diagram of the new proposal is shown in Figure 4.23.

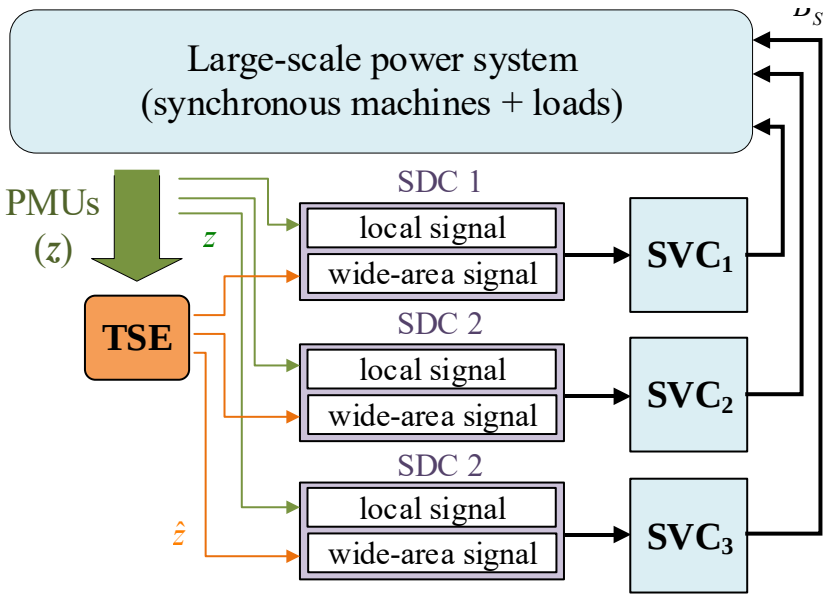

Figure 4.23 Proposal extended for stability enhancement of the large-scale power system, using multiple SVCs with their SDCs assisted by the TSE.

By following the procedure presented in Chapter 2, the SVCs available in the MIS are analyzed as candidates to extend the power oscillations' damping control. Three SVCs have been chosen to be equipped with SDCs. These compensators are located in the southeastern area and north area with nominal reactive powers of -50/150 MVAr, -300/600 MVAr, and -90/300 MVAr, respectively. On the other hand, the wide-area control signals $\hat{z}$ supplied to the SDCs of these controllers are obtained from the TSE at the north area and southeastern area. In these cases, the signal $\hat{z}$ is composed of the estimated phase angle voltages:

$$\hat{z} = \theta_{south} - \theta_{north}, \tag{4.1}$$

where θ_{south} and θ_{north} are the phase angles of voltages at nodes near generators g1 and g2, respectively. An overview of the above description is shown in Figure 4.24. For this case, the wide-area signal expressed in (4.1) is employed in the three SDCs.

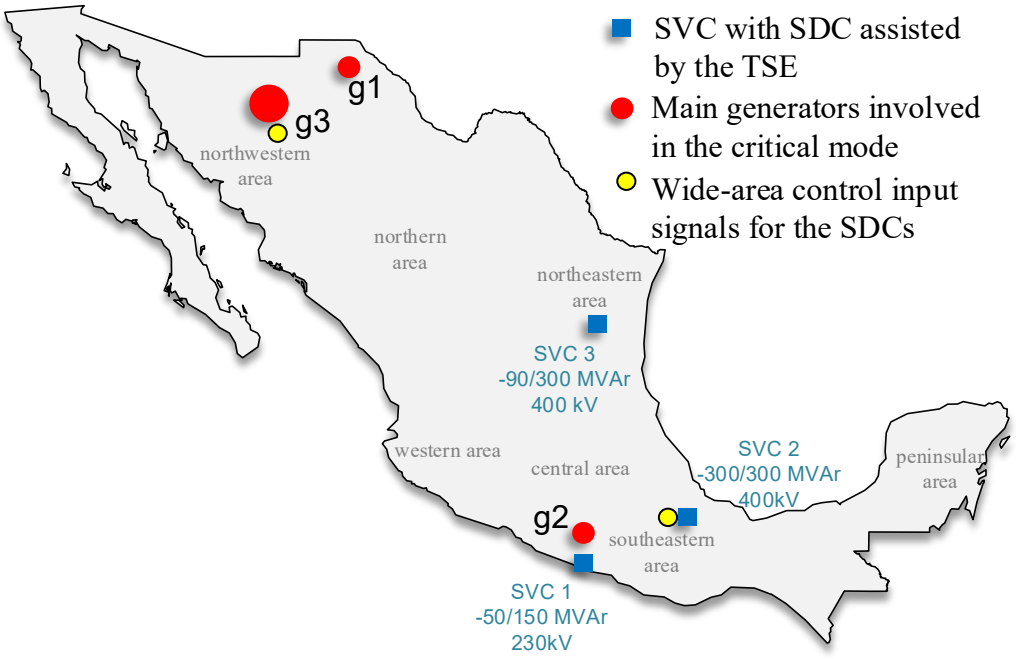

Figure 4.24 The geographic location of SVCs assisted by the TSE.

The selection of SVCs and remote signals is based on the analysis performed by using SSAT software on the closed-loop control system of these controllers. This analysis consists of utilizing different remote signals and local signals in the controllers' SDCs to evaluate their performance in the damping of oscillations. The damping controllers are composed of lead-lag phase compensation networks, with their parameters adjusted to the operating condition of the MIS. The robust controller for this system was not used because it goes beyond of the scope of this work. The block diagram of the employed SDC is shown in Figure 4.25, and the values of parameters are presented in Table 4.3. Although the delay is not modeled in the controller, a fixed delay of 100ms is considered in the UDM function used in the DSATools software.

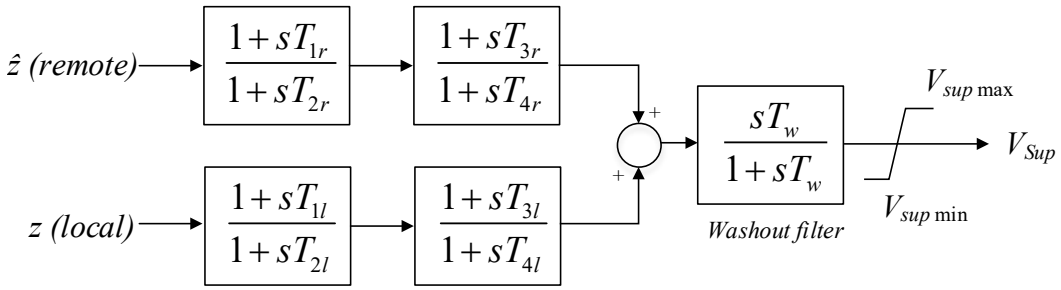

Figure 4.25 Block diagram of the SDC to control an SVC.

Table 4.3 Values of parameters for the SDCs utilized

SDC	T_{1r}	T_{2r}	T_{3r}	T_{4r}	T_{1l}	T_{2l}	T_{3l}	T_{4l}	T_w	$V_{sup\ max/min}$
SVC1	1.85	1.00	4.50	0.35	0.70	0.35	2.20	0.10	10.00	±0.10
SVC2	1.00	1.00	1.50	0.50	1.00	1.00	1.00	2.00	10.00	±0.10
SVC3	1.00	3.50	1.00	2.50	0.50	1.00	1.00	2.00	10.00	±0.10

The results obtained by using the SSAT software are shown in Table 4.4 for the critical mode. These results clearly show that the SVCs with SDCs improve the small-signal stability of the MIS. For evaluating the proposed method, a time-domain simulation is conducted by using the TSAT software. A solid three-phase fault is applied at a 400 kV bus located in the central area for six cycles (0.1s) and then cleared by tripping a tie line that interconnects the Mexico City metropolitan area to the southeastern area.

Table 4.4 Comparison of damping ratio of the critical mode of the MIS utilizing SDCs to control the respective SVCs

PSSs+SVCs (no SDCs)		**PSSs+SVCs+SDCs**	
Eigenvalue	Damping ratio @ frequency	Eigenvalue	Damping ratio @ frequency
-0.0929 ± *j* 2.3990	3.87% @ 0.381 Hz	-0.2206 ± *j* 0.3347	10.43% @ 0.334 Hz

A set of 24 signals measured by PMUs is utilized for estimating 10 state variables related to the wide-area signal $\hat{z}$. Gaussian white noise with a zero mean and a standard deviation σ = 0.001 (p.u.) is assumed for all the measurements. The initial covariance matrix is P_0 = $[0.001^2 \times I_{10}]$, and the covariance matrix of the process is $Q = [0.001^2 \times I_{10}]$.

The dynamic response of speed deviations of all generators embedded in the system is plotted in Figure 4.26 for the three-phase fault scenario, considering SVCs without SDCs. The system becomes unstable two seconds after the disturbance because generator 2 (g2) in the southeastern area loses synchronism. Furthermore, this dynamic behavior of the system is in accordance with the analysis provided by information of the system's mode shapes, where g2 has a significative participation in the critical mode.

By using the proposed method, the SVCs are responsible for providing the voltage support and the damping out of power oscillations through the modulation of reactive power in response to the SDCs and signals provided by the TSE.

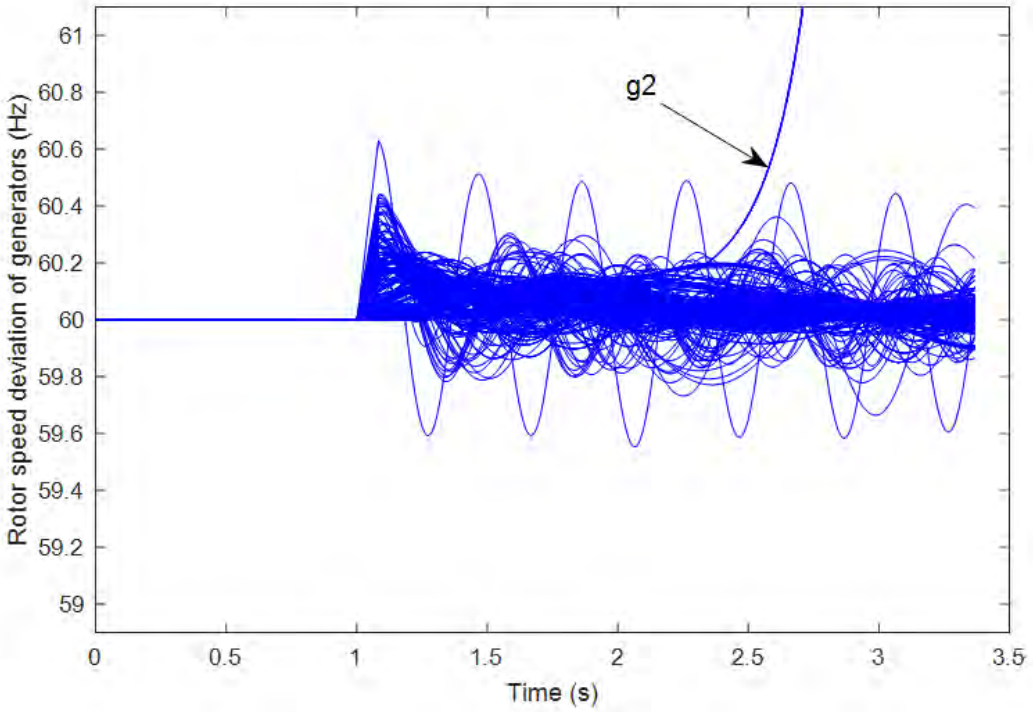

Figure 4.26 Response of speed deviation of generators to the large disturbance for the MIS without SDCs.

Figure 4.27 shows the dynamic behavior of the voltage magnitude at g2's terminals when the proposed method is employed. The coordinated control actions performed by the SVCs by using the estimated signals extends the voltage support during the disturbance such that the generator g2 reaches its stable speed as shown in Figure 4.28. Furthermore, the MIS becomes stable as illustrated in Figure 4.29, where the speed deviations of all generators are plotted.

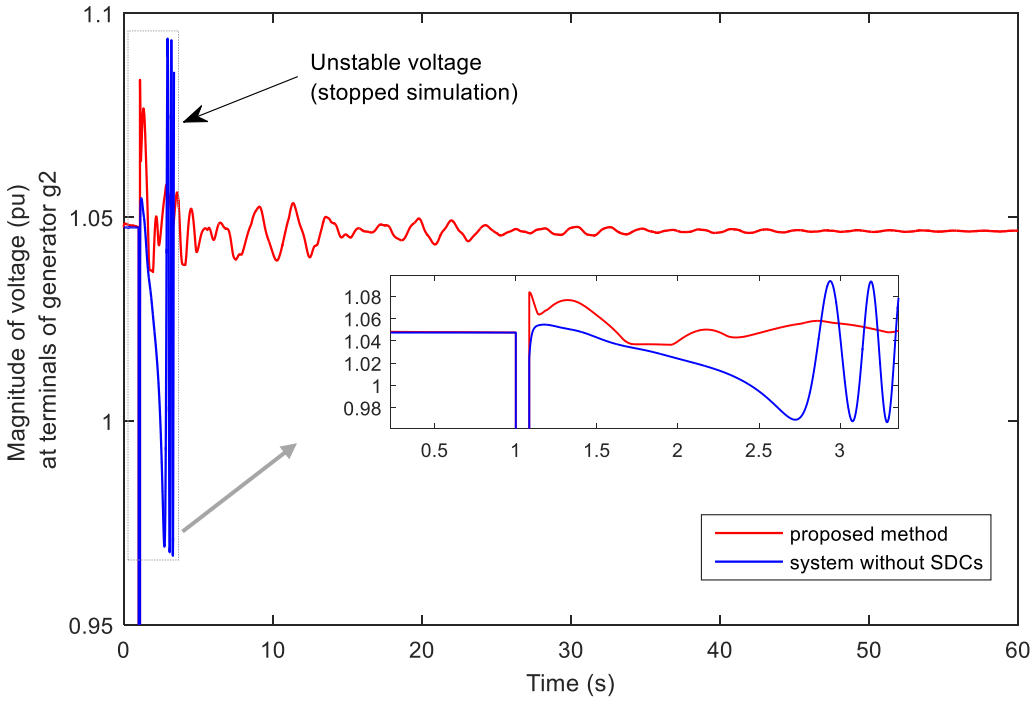

Figure 4.27 Response of voltage magnitude at terminals of generator g2 by using the proposed method.

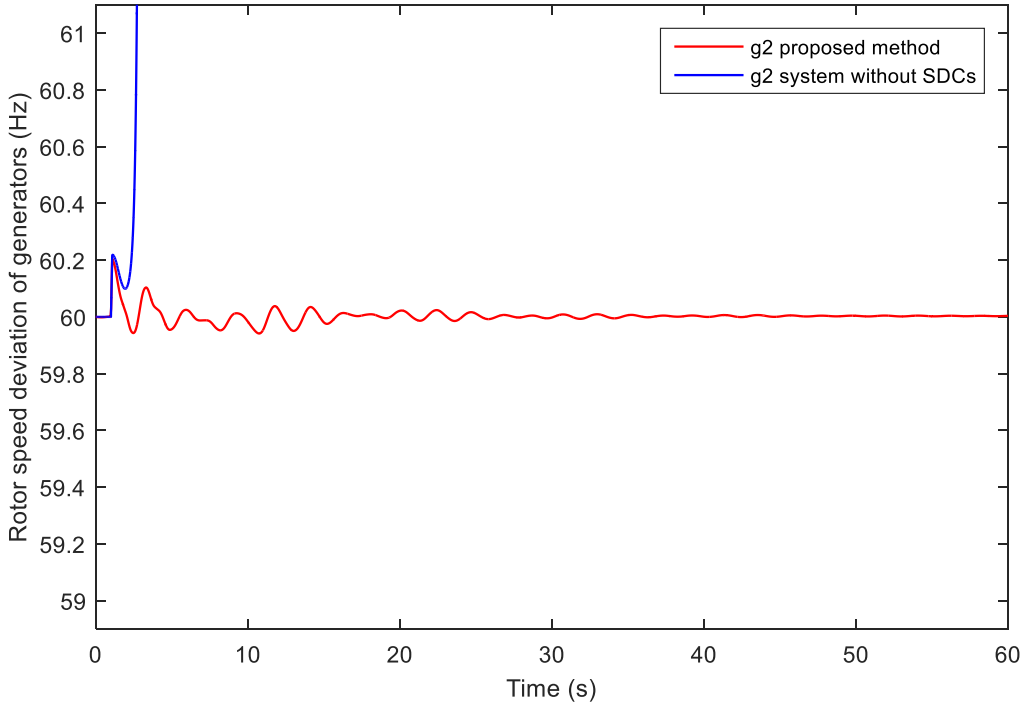

Figure 4.28 Response of speed deviation of generator g2 to the large disturbance by using the proposed method.

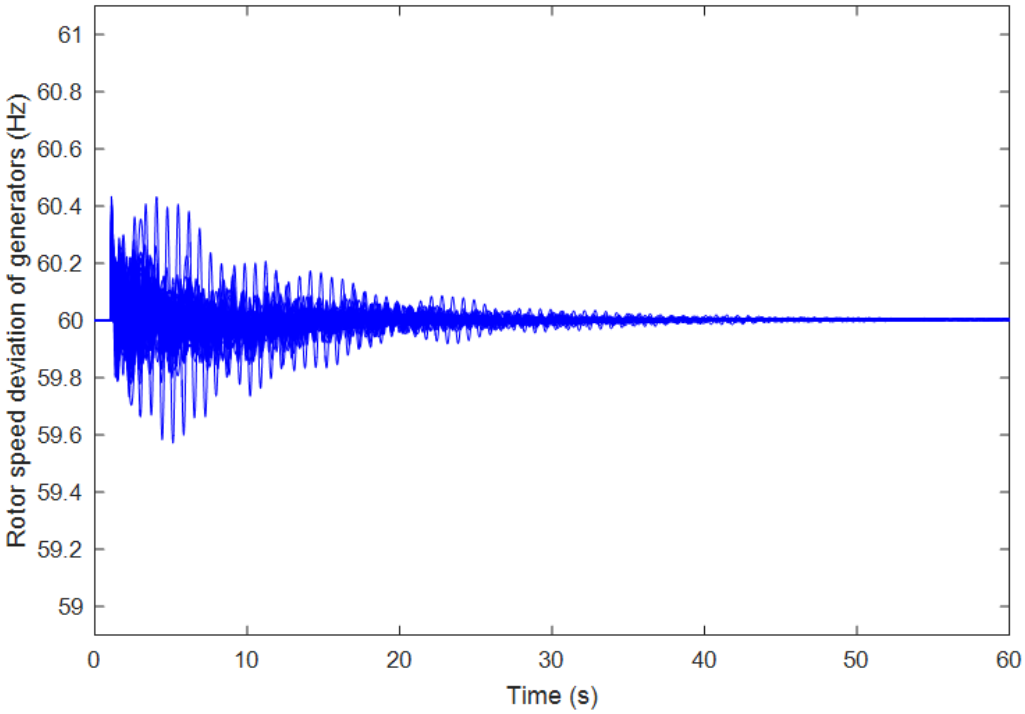

Figure 4.29 Response of speed deviation of generators to the large disturbance by using the proposed method.

Lastly, the outputs of supplementary controllers are shown in Figure 4.30. The dynamics of these voltages reflect the effort by the SVC devices to stabilize the large-scale system during the transient state.

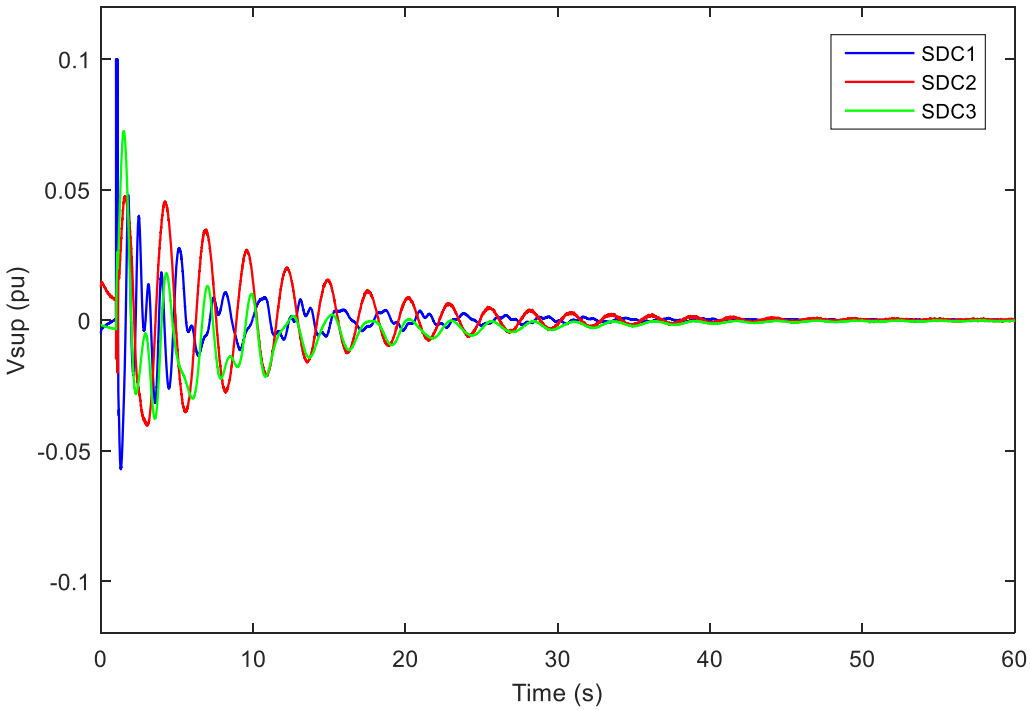

Figure 4.30 Response of output signal of SDCs to the large disturbance.

4.9 Summary

In this chapter, a new control scheme has been applied to the IEEE 50-generator system. Key aspects of the damping control using PMUs signals such as the variation of operating conditions and the three-phase fault location, as well as the level of Gaussian noise and the correlated noise, were evaluated by means of various scenarios. The performance of the estimator together with the SDC show a power oscillations' damping enhancement by extending the control afforded by the PSSs. In addition to these results, the processing time per estimation step of the TSE illustrates the possibility for the implementation of this algorithm as a real-time application.

To evaluate the feasibility of this proposal in a practical system, the MIS is analyzed, and the SVCs actually installed are exploited to improve the system’s small-signal stability. By employing the SSAT software, a critical mode is found. Furthermore, three static VARs compensators are selected to be the FACTS devices responsible for extending the power oscillation’s damping control by using SDCs assisted by the TSE. The coordinated control scheme improves the damping of the inter-area mode.

To validate the results of the linear analysis, a time-domain simulation is conducted, and the noisy PMUs signals for the TSE are included in the large-scale system. The estimator with the supplementary controllers enhances the stability of the MIS.

Chapter 5

Conclusions and future research

5.1 Conclusions

A novel control scheme for the damping of electromechanical oscillations in a multi-machine system by means of an SVC that employs both local and wide-area signals has been proposed in this thesis. Unlike other proposals reported in the literature, the wide-area stabilizing signals supplied to the SVC's supplementary damping controller are directly obtained from a PMU-based TSE program.

To damp out the LFOs, the proposal invokes two mature disciplines in power systems' fields such as small-signal analysis and tracking state estimation studies. In this sense, the linear models and the basis of modal analysis are presented in this work. Moreover, in order not to lose practicality, the state space representation of the system is formulated in compliance with the dynamic devices' output matrices provided by the SSAT software, which is one of the commercial applications most employed by the electrical industry.

The IEEE 50-generator system was used as the test bed system to illustrate the effectiveness of the proposed method. By following the experience reported in the literature regarding to the selection of an available signal for a damping controller, the magnitude of line current was utilized as the stabilizing signal. The small-signal analysis was conducted to evaluate the interaction between the SDC and the controllers of the dynamic devices in a

large-scale system. The results from the linear analysis showed that the use of a wide-area signal together with a local signal in the SDC improves the damping ratio for the critical inter-area mode.

On the other hand, the EKF formulation is employed for tracking the dynamic evolution of state variables. To achieve this goal, a set of 304 measurements from PMUs is processed by the TSE at each time step of the period of study. The BDD was also evaluated through 500 Monte Carlo simulations to handle bad data.

To analyze the proposed method on the test bed system, the TSE algorithm and noisy measurements were implemented in a UDM in TSAT. Hence, at each time step of the transient simulation is possible to estimate the system's state and supply the wide-area signal to the SDC to damp out the power oscillations. Results for the rotor angle and the active power of the generators with the larger participation in the critical mode show satisfactory performance of the new control scheme by improving the damping control afforded by the PSS. The estimator provided a control signal accurately as confirmed by the response of the supplementary controller. This confirmation is observed in comparison to the control when a true signal is utilized. To maintain a realistic scenario, a fixed time delay is considered in the estimated control signal. Furthermore, measurements at different noise levels, correlated noise, variation of system operating conditions, as well as different locations of faults were assessed, and the robustness of the damping control successfully prevailed. The CPU processing time appears to demonstrate the feasibility of using the proposed approach for real-time control applications. The development of dynamic models for the dynamic-link library (DLL) file in C language could allow scaling the project to another computing platform.

The largest residue and observability factor were employed to choose the best candidate signals for the SDC. Nevertheless, an alternative control signal based on the information provided by the mode shape associated with the critical inter-area mode may be utilized in the proposed method. The phase of the nodal voltages was employed in the test bed system. The results from the time-domain simulation show a slight improvement in the power oscillations' damping control using this new signal in comparison when the SDC uses the required control signal (magnitude of line current).

To evaluate the proposal in a practical system, the Mexican interconnected system was analyzed, and three of all installed SVCs were selected to damp out inter-area power oscillations. In accordance to the theoretical concepts on which the proposed approach is based, the estimated wide-area signals with local signals allow preserving the system's stability after a large disturbance by stabilizing the power oscillations produced by the generator involved in the critical inter-area mode.

Recognizing that processing and receiving many signals from PMUs with small time delays, as well as the error synchronization, increase the computational burden associated with the proposal, in practice these facts can be a challenge for the state estimation. Based on the mentioned above, the following future research is suggested.

5.2 Future research

Despite the effectiveness shown by the proposed schemes of stability control, the following proposals can be made as a continuation of the research in this dissertation.

1. Estimator
    - To develop a new methodology to consider the time delay associated with the measurements for the estimation process and evaluate the impact on the estimated stabilizing signal.
    - To evaluate an alternative technique for TSE in order to obtain stabilizing signals for the SDCs of FACTS devices in large-scale systems.
    - To predict the behavior of loads by using the estimated algebraic states provided by the TSE and to apply preventive control actions to avoid voltage instabilities and power oscillations.
    - To include the operation of protection schemes in the proposed method to avoid the misoperation of protection devices when an inter-area mode is being controlled by an SDC.
2. Control scheme for power oscillations' damping
    - To extend the proposed method by coordinating the SVC with the high-voltage direct current (HVDC) technology in order to smooth out the LFOs.

- To develop an adaptive SDC for several operating conditions by using the estimated algebraic variables without neglecting the interaction with all the dynamic devices.
- To implement hierarchical control based on several candidates' estimated signals when the wide-area control input does not have an impact on the SDC because of a change in the topologic network. For example, the required control signal is related to an element tripped in the transmission network.
- To implement and evaluate the proposed technique by using hardware-in-the-loop simulations

Appendix A
Power system component modelling

The linearized equations for the components of the system, as well as the state space matrices for the interconnected power system, are defined in this appendix.

A.1 Two-axis model for the synchronous machine

The *m* synchronous machines equipped with an excitation system are represented by the two-axis model [76]. The differential equations of this dynamic model that describe the electromechanical phenomenon are defined as

$$\Delta\dot{\omega}_{ri} = \frac{1}{2H}\left(T_{mi} - T_{ei} - K_{Di}\Delta\omega_{ri}\right) \tag{A.1}$$

$$\dot{\delta}_i = \omega_0 \Delta\omega_{ri} \tag{A.2}$$

$$\dot{E}'_{qi} = \frac{1}{T'_{d0i}}\left[-E'_{qi} - \left(x_{di} - x'_{di}\right)i_{di} + E_{fdi}\right] \tag{A.3}$$

$$\dot{E}'_{di} = \frac{1}{T'_{q0i}}\left[-E'_{di} + \left(x_{qi} - x'_{qi}\right)i_{qi}\right] \qquad i = 1,2,\ldots,m \quad , \tag{A.4}$$

where the state variables are composed of the rotor deviation $\Delta\omega$ (pu), the rotor angle δ in radians, and the *d*- and *q*-axis transient voltages E'_{qi}, E'_{di} (pu). E_{fdi} is the exciter output voltage; T_m is the mechanical torque. Finally, i_{di} and i_{qi} are the stator currents in the d- and q-axis, respectively. The parameters H_i and K_d are the inertia constant and the damping coefficient, respectively. T'_{d0} and T'_{q0} are the transient open-circuit time constants; x_{di} and x_{qi}

are the *d*- and *q*-axis synchronous reactances. Lastly, x'_{di} and x'_{qi} are the *d*- and *q*-axis transient reactances. The air-gap torque T_e (p.u.) is calculated as

$$T_e = E'_d i_d + E'_q i_q - \left(x'_d - x'_q\right) i_d i_q \quad . \tag{A.5}$$

The stator voltages in *d*- and *q*-axis are defined by

$$v_d = -r_a i_d + x'_q i_q + E'_d \tag{A.6}$$

$$v_q = -r_a i_q - x'_d i_d + E'_q \quad . \tag{A.7}$$

The magnitude of the generator terminal voltage is given by

$$V_t = \sqrt{v_d^2 + v_q^2} \quad . \tag{A.8}$$

Linearizing (A.1) - (A.4) around the nominal point of the system,

$$\begin{bmatrix} \Delta\dot{\omega}_{ri} \\ \Delta\dot{\delta}_i \\ \Delta\dot{E}'_{qi} \\ \Delta\dot{E}'_{di} \end{bmatrix} = \begin{bmatrix} \frac{-K_{Di}}{2H_i} & 0 & 0 & 0 \\ 0 & \omega_0 & 0 & 0 \\ 0 & 0 & -\frac{1}{T'_{d0i}} & 0 \\ 0 & 0 & 0 & -\frac{1}{T'_{q0i}} \end{bmatrix} \begin{bmatrix} \Delta\omega_{ri} \\ \Delta\delta_i \\ \Delta E'_{qi} \\ \Delta E'_{di} \end{bmatrix}$$
$$+ \begin{bmatrix} 0 & 0 & \frac{-1}{2H_i} \\ 0 & 0 & 0 \\ \frac{-\left(x_{di} - x'_{di}\right)}{T'_{d0i}} & 0 & 0 \\ 0 & \frac{\left(x_{qi} - x'_{qi}\right)}{T'_{q0i}} & 0 \end{bmatrix} \begin{bmatrix} \Delta i_{di} \\ \Delta i_{qi} \\ \Delta T_{ei} \end{bmatrix} \Delta T_{ei} + \begin{bmatrix} 0 & \frac{1}{2H_i} \\ 0 & 0 \\ \frac{1}{T'_{d0i}} & 0 \\ 0 & 0 \end{bmatrix} \begin{bmatrix} \Delta E_{fdi} \\ \Delta T_{mi} \end{bmatrix}$$
. (A.9)

Similarly, by linearizing (A.6) and (A.7), the incremental stator voltages are defined as

$$\begin{bmatrix} \Delta v_d \\ \Delta v_q \end{bmatrix} = -\begin{bmatrix} r_a & -x'_q \\ x'_d & r_a \end{bmatrix} \begin{bmatrix} \Delta i_d \\ \Delta i_q \end{bmatrix} + \begin{bmatrix} 0 & 1 \\ 1 & 0 \end{bmatrix} \begin{bmatrix} \Delta E'_q \\ \Delta E'_d \end{bmatrix} \quad . \tag{A.10}$$

The linearization of (A.5) and (A.8) results in

$$\Delta T_e = \left[E'_{d0} - \left(x'_d - x'_q \right) i_{q0} \right] \Delta i_d + \left[E'_{q0} - \left(x'_d - x'_q \right) i_{d0} \right] \Delta i_q + i_{qo} \Delta E'_q + i_{d0} \Delta E'_d \qquad \text{(A.11)}$$

$$\Delta V_t = \frac{v_{q0}}{V_{t0}} \Delta E'_q + \frac{v_{d0}}{V_{t0}} \Delta E'_d + \left(-\frac{v_{d0}}{V_{t0}} r_a - \frac{v_{q0}}{V_{t0}} x'_d \right) \Delta i_d + \left(-\frac{v_{q0}}{V_{t0}} r_a + \frac{v_{d0}}{V_{t0}} x'_q \right) \Delta i_q \qquad \text{(A.12)}$$

.

The subscript 0 indicates the initial values of the incremental variables by taking the values from the results of a power flow study.

A.2 Excitation system model

The i^{th} generator represented by the two-axis model is equipped with AC-4 exciters [28], with their block diagram shown in Figure A.1. The differential equations for this excitation system can by defined as

$$\dot{X}_{E1i} = \frac{1}{T_{Ri}} V_{Ti} - \frac{1}{T_{Ri}} X_{E1i} \qquad \text{(A.13)}$$

$$\dot{X}_{Ei2} = \frac{T_{Bi} - T_{Ci}}{T_{Bi}^2} \left(V_{REFi} + V_{si} - X_{E1i} \right) - \frac{1}{T_{Bi}} X_{E2i} \qquad \text{(A.14)}$$

$$\dot{E}_{Li} = \frac{K_{Ai}}{T_{Ai}} X_{E2i} - \frac{1}{T_{Ai}} E_{Li} + \frac{K_{Ai} T_{Ci}}{T_{Ai} T_{Bi}} \left(V_{REFi} + V_{si} - X_{E1i} \right) \qquad \text{(A.15)}$$

$$\text{Limiter: } \begin{cases} E_{Li} < E_{fd\_\min} & E_{fdi} = E_{fd\_\min} \\ E_{Li} > E_{fd\_\max} & E_{fdi} = E_{fd\_\max} \\ E_{fd\_\min} \le E_{Li} \le E_{fd\_\max} & E_{fdi} = E_{Li} \end{cases} \quad i = 1, 2, \ldots, m \quad , \qquad \text{(A.16)}$$

where X_{E1i}, X_{E2i} and E_{Li} (E_{fdi}) are the state variables. V_{REFi} is the exciter reference voltage, V_{Ti} is the generator terminal voltage, and V_s is the supplementary voltage from the PSS.

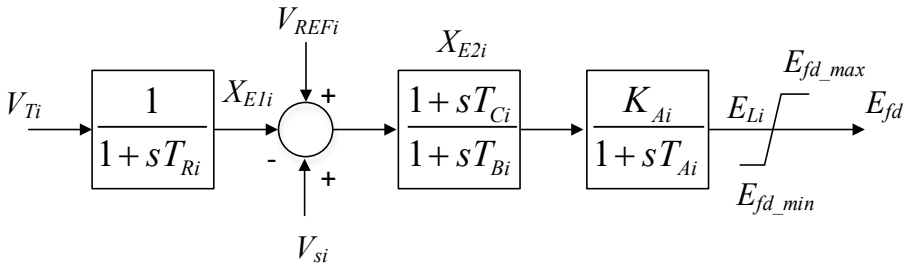

Figure A.1 IEEE AC-4 Model for the Excitation System

Linearizing (A.1) - (A.4) around the nominal point of the system leads to

$$\begin{bmatrix} \Delta\dot{X}_{E1i} \\ \Delta\dot{X}_{Ei2} \\ \Delta\dot{E}_{Li} \end{bmatrix} = \begin{bmatrix} -\frac{1}{T_{Ri}} & 0 & 0 \\ -\frac{T_{Bi}-T_{Ci}}{T_{Bi}^2} & -\frac{1}{T_{Bi}} & 0 \\ -\frac{K_{Ai}T_{Ci}}{T_{Ai}T_{Bi}} & \frac{K_{Ai}}{T_{Ai}} & -\frac{1}{T_{Ai}} \end{bmatrix} \begin{bmatrix} \Delta X_{E1i} \\ \Delta X_{Ei2} \\ \Delta E_{Li} \end{bmatrix} + \begin{bmatrix} \frac{1}{T_{Ri}} & 0 \\ 0 & \frac{T_{Bi}-T_{Ci}}{T_{Bi}^2} \\ 0 & \frac{K_{Ai}T_{Ci}}{T_{Ai}T_{Bi}} \end{bmatrix} \begin{bmatrix} \Delta V_{Ti} \\ \Delta V_{si} \end{bmatrix} \quad . \qquad \text{(A.17)}$$

A.3 PSS model

The IEEE standard speed-based PSS model [29] associated with the excitation system is considered in this work. According to the block diagram represented in Figure A.2, the dynamic equation of this PSS model are

$$\dot{X}_{P1i} = \frac{K_{Si}}{T_{5pi}}\Delta\omega_i - \frac{1}{T_{5pi}}X_{P1i} \qquad \text{(A.18)}$$

$$\dot{X}_{P2i} = \frac{T_{2pi}-T_{1pi}}{T_{2pi}^2}K_{Si}\Delta\omega_i - \frac{T_{2pi}-T_{1pi}}{T_{2pi}^2}X_{P1i} - \frac{1}{T_{2pi}}X_{P2i} \qquad \text{(A.19)}$$

$$\dot{X}_{P3i} = \frac{\left(T_{4pi}-T_{3pi}\right)T_{1pi}K_{Si}}{T_{4pi}^2T_{2pi}}\Delta\omega_i - \frac{\left(T_{4pi}-T_{3pi}\right)T_{1i}}{T_{4pi}^2T_{2pi}}X_{P1i} + \frac{T_{4pi}-T_{3pi}}{T_{4pi}^2}X_{P2i} - \frac{1}{T_{4pi}}X_{P3i} \qquad \text{(A.20)}$$

$$V_{Li} = \frac{T_{1pi}T_{3pi}K_{Si}}{T_{2pi}T_{4pi}}\Delta\omega - \frac{T_{1pi}T_{3pi}}{T_{2pi}T_{4pi}}X_{P1i} + \frac{T_{3pi}}{T_{4pi}}X_{P2i} + X_{P3i} \qquad \text{(A.21)}$$

$$\text{Limiter:}\begin{cases} V_{Li} < V_{s\min} & V_{si} = V_{s\min} \\ V_{Li} > V_{s\max} & V_{si} = V_{s\max} \\ V_{s\min} \le V_{Li} \le V_{s\max} & V_{si} = V_{Li} \end{cases} \qquad i = 1,2,\ldots,m, \tag{A.22}$$

where V_{si} is the output voltage of the PSS, which is composed of the state variables X_{P1i}, X_{P2i} and X_{P3i}.

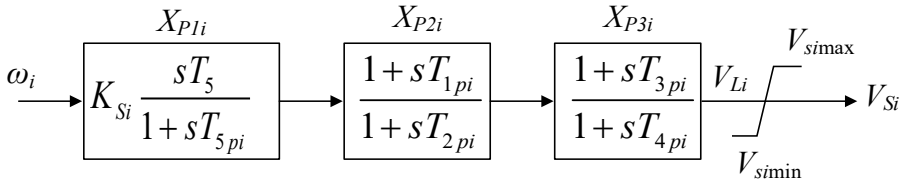

Figure A.2 IEEE standard type PSS1A model.

The linearization of (A.18)-(A.20) results in

$$\begin{bmatrix} \Delta\dot{X}_{P1i} \\ \Delta\dot{X}_{P2i} \\ \Delta\dot{X}_{P3i} \end{bmatrix} = \begin{bmatrix} -\dfrac{1}{T_{5pi}} & 0 & 0 \\ -\dfrac{T_{2pi}-T_{1pi}}{T_{2pi}^2} & -\dfrac{1}{T_{2pi}} & 0 \\ -\dfrac{(T_{4pi}-T_{3pi})T_{1i}}{T_{4pi}^2 T_{2pi}} & \dfrac{T_{4pi}-T_{3pi}}{T_{4pi}^2} & -\dfrac{1}{T_{4pi}} \end{bmatrix} \begin{bmatrix} \Delta X_{P1i} \\ \Delta X_{P2i} \\ \Delta X_{P3i} \end{bmatrix} + \begin{bmatrix} \dfrac{K_{Si}}{T_{5pi}} \\ \dfrac{T_{2pi}-T_{1pi}}{T_{2pi}^2}K_{Si} \\ \dfrac{(T_{4pi}-T_{3pi})T_{1pi}K_{Si}}{T_{4pi}^2 T_{2pi}} \end{bmatrix} \Delta\omega \quad . \tag{A.23}$$

Similarly, the linearization of (A.21) is expressed by

$$\Delta V_{Li} = -\frac{T_{1pi}T_{3pi}}{T_{2pi}T_{4pi}}\Delta X_{P1i} + \frac{T_{3pi}}{T_{4pi}}\Delta X_{P2i} + \Delta X_{P3i} + \frac{T_{1pi}T_{3pi}K_{Si}}{T_{2pi}T_{4pi}}\Delta\omega \quad . \tag{A.24}$$

A.4 Reference frame transformation

Each two-axis model for the SM is expressed in its own *d-q* axis frame that rotates at the machine's rotor speed. In practice, however, a reference frame rotating at synchronous speed (ω_0) is used as a common reference frame for stability analysis [25]. Regarding Figure A.3, the equations for the transformation between the individual machine's (*d-q*) reference frame and the common (*D-Q*) reference are expressed as

$$\begin{bmatrix} V_D \\ V_Q \end{bmatrix} = \begin{bmatrix} \operatorname{sen}\delta & \cos\delta \\ -\cos\delta & \operatorname{sen}\delta \end{bmatrix} \begin{bmatrix} v_d \\ v_q \end{bmatrix} = \boldsymbol{T}(\delta) \begin{bmatrix} v_d \\ v_q \end{bmatrix}, \tag{A.25}$$

where $\boldsymbol{T}$ is a rotation matrix [1].

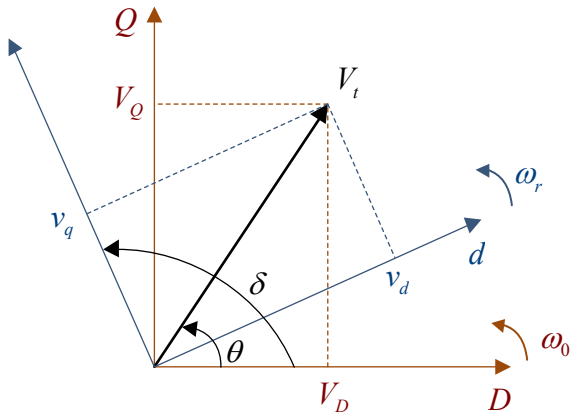

Figure A.3 Reference frame transformation

The linearization of (A.25) around the nominal point of the system results in

$$\begin{bmatrix} \Delta v_d \\ \Delta v_q \end{bmatrix} = \begin{bmatrix} \operatorname{sen}\delta_0 & -\cos\delta_0 \\ \cos\delta_0 & \operatorname{sen}\delta_0 \end{bmatrix} \begin{bmatrix} \Delta V_D \\ \Delta V_Q \end{bmatrix} + \begin{bmatrix} v_{q0} \\ -v_{d0} \end{bmatrix} \Delta\delta \quad . \tag{A.26}$$

Similarly, the equations for the reference transformation can be applied to the currents' equations:

$$\begin{bmatrix} \Delta i_d \\ \Delta i_q \end{bmatrix} = \begin{bmatrix} \operatorname{sen}\delta_0 & -\cos\delta_0 \\ \cos\delta_0 & \operatorname{sen}\delta_0 \end{bmatrix} \begin{bmatrix} \Delta I_D \\ \Delta I_Q \end{bmatrix} + \begin{bmatrix} i_{q0} \\ -i_{d0} \end{bmatrix} \Delta\delta \quad . \tag{A.27}$$

A.5 Classical model for the SM

The classical model is the simplest representation of the SM. This model is also called the constant voltage behind the transient reactance model [76]. The linearized equations of motion of the generator described by the two-axis model are

$$\Delta\dot{\omega}_{ri} = \frac{1}{2H_i}\left(\Delta T_{mi} - \Delta T_{ei} - K_{Di}\Delta\omega_{ri}\right) \tag{A.28}$$

$$\Delta\dot{\delta}_i = \omega_0\Delta\omega_{ri} \quad . \tag{A.29}$$

By using the voltage and current phasors at the terminal of the generator, the constant voltage behind x'_d is computed as

$$E'_0\angle\delta_0 = \left(V_{D0} + jV_{Q0}\right) + jx'_d\left(I_{D0} + jI_{Q0}\right) \quad . \tag{A.30}$$

The classical model can also be obtained formally from the two-axis model by setting $E'_{q0} = E'_0$, $x'_q = x'_d$ and r_a = 0. Thus, the linearized equation for air-gap torque (A.11) is modified as

$$\Delta T_e = E'_{q0}\Delta i_q \quad . \tag{A.31}$$

A.6 SVC model

The TSAT Type-1 model [30] is utilized for modeling the SVC. The block diagram of this model is shown in Figure 2.1 of Chapter 2. The corresponding dynamic equations are

$$\dot{X}_{s1} = -\frac{1}{T_3}X_{s1} + \frac{\left(T_3 - T_1\right)K_{SVC}}{T_3^2}\left(V_{SVC} + V_{Sup} - V_{REF,SVC}\right) \tag{A.32}$$

$$\dot{X}_{s2} = \frac{T_4 - T_2}{T_4^2}X_{s1} - \frac{1}{T_4}X_{s2} + \frac{\left(T_4 - T_2\right)T_1K_{SVC}}{T_4^2T_3}\left(V_{SVC} + V_{Sup} - V_{REF,SVC}\right) \tag{A.33}$$

$$\dot{B}_L = \frac{T_2}{T_4T_5}X_{s1} + \frac{1}{T_5}X_{s2} - \frac{1}{T_5}B_L + \frac{T_1T_2K_{SVC}}{T_3T_4T_5}\left(V_{SVC} + V_{Sup} - V_{REF,SVC}\right) \tag{A.34}$$

$$\text{Limiter: } \begin{cases} B_L < B_{SVC\min} & B_{SVC} = B_{SVC\min} \\ B_L > B_{SVC\max} & B_{SVC} = B_{SVC\max} \\ B_{SVC\min} \le B_L \le B_{SVC\max} & B_{SVC} = B_L \end{cases}, \tag{A.35}$$

where X_{s1}, X_{s2}, and B_L are the state variables; furthermore, Q_C and Q_L specify the capacity rating of the SVC. V_{ref} is the SVC reference voltage, V_{SVC} is the voltage magnitude of the SVC bus, and B_{SVC} is the equivalent admittance of the SVC.

The current injected by the SVC into the network may be defined in terms of the *D*- and *Q*-axis reference frame as

$$\begin{bmatrix} I_{SVC,D} \\ I_{SVC,Q} \end{bmatrix} = \begin{bmatrix} 0 & -B_{SVC} \\ B_{SVC} & 0 \end{bmatrix} \begin{bmatrix} V_{SVC,D} \\ V_{SVC,Q} \end{bmatrix} \quad . \tag{A.36}$$

Linearizing (A.32)-(A.34) around the nominal point of the system leads to

$$\begin{bmatrix} \Delta\dot{X}_{s1} \\ \Delta\dot{X}_{s2} \\ \Delta\dot{B}_L \end{bmatrix} = \begin{bmatrix} -\frac{1}{T_3} & 0 & 0 \\ \frac{T_4 - T_2}{T_4^2} & -\frac{1}{T_4} & 0 \\ \frac{T_2}{T_4 T_5} & \frac{1}{T_5} & -\frac{1}{T_5} \end{bmatrix} \begin{bmatrix} \Delta X_{s1} \\ \Delta X_{s2} \\ \Delta B_L \end{bmatrix} + \begin{bmatrix} \frac{(T_3 - T_1)K_{SVC}}{T_3^2} \\ \frac{(T_4 - T_2)T_1 K_{SVC}}{T_4^2 T_3} \\ \frac{T_1 T_2 K_{SVC}}{T_3 T_4 T_5} \end{bmatrix} \Delta V_{SVC} + \begin{bmatrix} \frac{(T_3 - T_1)K_{SVC}}{T_3^2} \\ \frac{(T_4 - T_2)T_1 K_{SVC}}{T_4^2 T_3} \\ \frac{T_1 T_2 K_{SVC}}{T_3 T_4 T_5} \end{bmatrix} \Delta V_{Sup} \quad . \tag{A.37}$$

Similarly, the linearization of (A.36) results in

$$\begin{bmatrix} \Delta I_{SVC,D} \\ \Delta I_{SVC,Q} \end{bmatrix} = \begin{bmatrix} 0 & -B_{SVC0} \\ B_{SVC0} & 0 \end{bmatrix} \begin{bmatrix} \Delta V_{SVC,D} \\ \Delta V_{SVC,Q} \end{bmatrix} + \begin{bmatrix} -V_{SVC0,Q} \\ V_{SVC0,D} \end{bmatrix} \Delta B_{SVC} \quad . \tag{A.38}$$

A.7 Load model

The constant impedance is a common consideration adopted in most stability analysis approaches [77]. Thus, the linear load is considered in this work.

The shunt admittance representing the load is computed as [25]

$$G_L = \frac{P_{L0}}{V_0^2} \tag{A.39}$$

$$B_L = \frac{Q_{L0}}{V_0^2}, \tag{A.40}$$

where P_{L0} and B_{L0} are the initial values of the active and reactive components of load, respectively; V_0 is the initial value of the bus voltage magnitude.

A.8 Matrices for the state-space representation of the power system

To obtain the state-space representation of the interconnected power system, the EPRI approach or current balance formulation reported in [1] was applied to the linearized models reported above. Thus, the details of the matrices for the state-space representation utilized in Chapter 2 of this work are presented in this section.

Rewriting the state space equations (2.4) and (2.5) as

$$\Delta\dot{\boldsymbol{x}} = \boldsymbol{A}_D\Delta\boldsymbol{x} + \boldsymbol{B}_D\Delta\boldsymbol{v} + \boldsymbol{B}\Delta u$$

$$\Delta\boldsymbol{i} = \boldsymbol{C}_D\Delta\boldsymbol{x} - \boldsymbol{Y}_D\Delta\boldsymbol{v},$$

where $\boldsymbol{A_D}$ and $\boldsymbol{C_D}$ are block diagonal matrices composed of $\boldsymbol{A_i}$ and $\boldsymbol{C_i}$ associated with the individual devices: the n generators and the SVC embedded in the network.

$$\boldsymbol{A_D} = \begin{bmatrix} \boldsymbol{A_1^{G1}} & 0 & 0 & 0 & 0 & 0 & 0 \\ 0 & \ddots & 0 & 0 & 0 & 0 & 0 \\ 0 & 0 & \boldsymbol{A_m^{G1}} & 0 & 0 & 0 & 0 \\ 0 & 0 & 0 & \boldsymbol{A_{m+1}^{G2}} & 0 & 0 & 0 \\ 0 & 0 & 0 & 0 & \ddots & 0 & 0 \\ 0 & 0 & 0 & 0 & 0 & \boldsymbol{A_n^{G2}} & 0 \\ 0 & 0 & 0 & 0 & 0 & 0 & \boldsymbol{A_{n+1}^{SVC}} \end{bmatrix}_{(10m+2n-2m+3)\times(10m+2n-2m+3)} \tag{A.41}$$

$$\boldsymbol{C_D} = \begin{bmatrix} \boldsymbol{C_1^{G1}} & 0 & 0 & 0 & 0 & 0 & 0 \\ 0 & \ddots & 0 & 0 & 0 & 0 & 0 \\ 0 & 0 & \boldsymbol{C_m^{G1}} & 0 & 0 & 0 & 0 \\ 0 & 0 & 0 & \boldsymbol{C_{m+1}^{G2}} & 0 & 0 & 0 \\ 0 & 0 & 0 & 0 & \ddots & 0 & 0 \\ 0 & 0 & 0 & 0 & 0 & \boldsymbol{C_n^{G2}} & 0 \\ 0 & 0 & 0 & 0 & 0 & 0 & \boldsymbol{C_{n+1}^{SVC}} \end{bmatrix}_{2(n+1)\times(10m+2n-2m+3)} . \tag{A.42}$$

Matrices $\boldsymbol{A_i^{G1}}$ and $\boldsymbol{C_i^{G1}}$ associated with the m synchronous machines equipped with the PSS system are given by

$$\boldsymbol{A_i^{G1}} = \begin{bmatrix} A_{Mi(1,1)} & A_{Mi(1,2)} & A_{Mi(1,3)} & A_{Mi(1,4)} & 0 & 0 & 0 & 0 & 0 & 0 \\ 0 & A_{Mi(2,2)} & 0 & 0 & 0 & 0 & 0 & 0 & 0 & 0 \\ 0 & A_{Mi(3,2)} & A_{Mi(3,3)} & A_{Mi(3,4)} & 0 & 0 & 0 & 0 & 0 & 0 \\ 0 & A_{Mi(4,2)} & A_{Mi(4,3)} & A_{Mi(4,4)} & 0 & 0 & 0 & 0 & 0 & 0 \\ 0 & A_{Mi(5,2)} & A_{Mi(5,3)} & A_{Mi(5,4)} & A_{Mi(5,5)} & 0 & 0 & 0 & 0 & 0 \\ A_{Mi(6,1)} & 0 & 0 & 0 & A_{Mi(6,5)} & A_{Mi(6,6)} & 0 & A_{Mi(6,8)} & A_{Mi(6,9)} & A_{Mi(6,10)} \\ A_{Mi(7,1)} & 0 & 0 & 0 & A_{Mi(7,5)} & A_{Mi(7,6)} & A_{Mi(7,7)} & A_{Mi(7,8)} & A_{Mi(7,9)} & A_{Mi(7,10)} \\ A_{Mi(8,1)} & 0 & 0 & 0 & 0 & 0 & 0 & A_{Mi(8,8)} & 0 & 0 \\ A_{Mi(9,1)} & 0 & 0 & 0 & 0 & 0 & 0 & A_{Mi(9,8)} & A_{Mi(9,9)} & 0 \\ A_{Mi(10,1)} & 0 & 0 & 0 & 0 & 0 & 0 & A_{Mi(10,8)} & A_{Mi(10,9)} & A_{Mi(10,10)} \end{bmatrix}_{10\times10} \tag{A.43}$$

$$\boldsymbol{C_i^{G1}} = \left[\begin{array}{c|ccc|cccccc} 0 & \begin{array}{l}\operatorname{sen}\delta_{0i}\left(F_{3i(1,2)} - i_{q0i}\right) \\ +\cos\delta_{0i}\left(F_{3i(2,2)} + i_{d0i}\right)\end{array} & F_{3i(2,3)}\cos\delta_{0i} & \begin{array}{l}F_{3i(2,4)}\cos\delta_{0i} \\ +F_{3i(1,4)}\operatorname{sen}\delta_{0i}\end{array} & 0 & 0 & 0 & 0 & 0 & 0 \\ \hline 0 & \begin{array}{l}\operatorname{sen}\delta_{0i}\left(F_{3i(2,2)} + i_{d0i}\right) \\ -\cos\delta_{0i}\left(F_{3i(1,2)} - i_{q0i}\right)\end{array} & F_{3i(2,3)}\operatorname{sen}\delta_{0i} & \begin{array}{l}F_{3i(2,4)}\cos\delta_{0i} \\ -F_{3i(1,4)}\cos\delta_{0i}\end{array} & 0 & 0 & 0 & 0 & 0 & 0 \end{array}\right]_{2\times10}$$

(A.44)

$$A_{Mi(1,1)} = -K_{Di} / \left(2H_i\right) \tag{A.45}$$

$$A_{Mi(1,2)} = -H_{1i(1,2)} / \left(2H_i\right) \tag{A.46}$$

$$A_{Mi(1,3)} = -H_{1i(1,3)} / \left(2H_i\right) \tag{A.47}$$

$$A_{Mi(1,4)} = -H_{1i(1,4)} / \left(2H_i\right) \tag{A.48}$$

$$A_{Mi(2,2)} = \omega_0 \tag{A.49}$$

$$A_{Mi(3,2)} = -F_{3i(1,2)} \left(x_{di} - x'_{di}\right) / T'_{d0i} \tag{A.50}$$

$$A_{Mi(3,3)} = -1 / T'_{d0i} - F_{3i(1,3)} \left(x_{di} - x'_{di}\right) / T'_{d0i} \tag{A.51}$$

$$A_{Mi(3,4)} = 1 / T'_{d0} - F_{3i(1,4)} \left(x_{di} - x'_{di}\right) / T'_{d0} \tag{A.52}$$

$$A_{Mi(4,2)} = F_{3i(2,2)} \left(x_{qi} - x'_{qi}\right) / T'_{q0i} \tag{A.53}$$

$$A_{Mi(4,3)} = F_{3i(2,3)} \left(x_{qi} - x'_{qi}\right) / T'_{q0i} \tag{A.54}$$

$$A_{Mi(4,4)} = F_{3i(2,4)} \left(x_{qi} - x'_{qi}\right) / T'_{q0i} - 1 / T'_{q0i} \tag{A.55}$$

$$A_{Mi(5,2)} = H_{1i(2,2)} / T_{Ri} \tag{A.56}$$

$$A_{Mi(5,3)} = H_{1i(2,3)} / T_{Ri} \tag{A.57}$$

$$A_{Mi(5,4)} = H_{1i(2,4)} / T_{Ri} \tag{A.58}$$

$$A_{Mi(5,5)} = -1 / T_{Ri} \tag{A.59}$$

$$A_{Mi(6,1)} = K_{Si} T_{1i} T_{3i} \left(T_{Bi} - T_{Ci}\right) / \left(T_{2i} T_{4i} T_{Bi}^2\right) \tag{A.60}$$

$$A_{Mi(6,5)} = -\left(T_{Bi} - T_{Ci}\right) / T_{Bi}^2 \tag{A.61}$$

$$A_{Mi(6,6)} = -1 / T_{Bi} \tag{A.62}$$

$$A_{Mi(6,8)} = -T_{1i} T_{3i} \left(T_{Bi} - T_{Ci}\right) / \left(T_{2i} T_{4i} T_B^2\right) \tag{A.63}$$

$$A_{Mi(6,9)} = T_{3i} \left(T_{Bi} - T_{Ci}\right) / \left(T_{4i} T_{Bi}^2\right) \tag{A.64}$$

$$A_{Mi(6,10)} = \left(T_{Bi} - T_{Ci}\right) / T_{Bi}^2 \tag{A.65}$$

$$A_{Mi(7,1)} = K_{Ai} K_{Si} T_{1i} T_{3i} T_{Ci} / \left(T_{2i} T_{4i} T_{Ai} T_{Bi}\right) \tag{A.66}$$

$$A_{Mi(7,5)} = -K_{Ai}T_{Ci} / \left(T_{Ai}T_{Bi}\right) \tag{A.67}$$

$$A_{Mi(7,6)} = K_{Ai} / T_{Ai} \tag{A.68}$$

$$A_{Mi(7,7)} = -1 / T_{Ai} \tag{A.69}$$

$$A_{Mi(7,8)} = -K_{Ai}T_{1i}T_{3i}T_{Ci} / \left(T_{2i}T_{4i}T_{Ai}T_{Bi}\right) \tag{A.70}$$

$$A_{Mi(7,9)} = K_{Ai}T_{3i}T_{Ci} / \left(T_{4i}T_{Ai}T_{Bi}\right) \tag{A.71}$$

$$A_{Mi(7,10)} = K_{Ai}T_{Ci} / \left(T_{Ai}T_{Bi}\right) \tag{A.72}$$

$$A_{Mi(8,1)} = K_{Si} / T_{5i} \tag{A.73}$$

$$A_{Mi(8,8)} = -1 / T_{5i} \tag{A.74}$$

$$A_{Mi(9,1)} = -K_{Si}\left(T_{1i} - T_{2i}\right) / T_{2i}^2 \tag{A.75}$$

$$A_{Mi(9,8)} = \left(T_{1i} - T_{2i}\right) / T_{2i}^2 \tag{A.76}$$

$$A_{Mi(9,9)} = -1 / T_{2i} \tag{A.77}$$

$$A_{Mi(10,1)} = -K_{Si}T_{1i}\left(T_{3i} - T_{4i}\right) / \left(T_{2i}T_{4i}^2\right) \tag{A.78}$$

$$A_{Mi(10,8)} = T_{1i}\left(T_{3i} - T_{4i}\right) / \left(T_{2i}T_{4i}^2\right) \tag{A.79}$$

$$A_{Mi(10,9)} = -\left(T_{3i} - T_{4i}\right) / T_{4i}^2 \tag{A.80}$$

$$C_{Mi(1,2)} = \operatorname{sen}\delta_{0i}\left(F_{3i(1,2)} - i_{q0i}\right) + \cos\delta_{0i}\left(F_{3i(2,2)} + i_{d0i}\right) \tag{A.81}$$

$$C_{Mi(1,3)} = F_{3i(2,3)}\cos\delta_{0i} + F_{3i(1,3)}\operatorname{sen}\delta_{0i} \tag{A.82}$$

$$C_{Mi(1,4)} = F_{3i(2,4)}\cos\delta_{0i} + F_{3i(1,4)}\operatorname{sen}\delta_{0i} \tag{A.83}$$

$$C_{Mi(2,2)} = \operatorname{sen}\delta_{0i}\left(F_{3i(2,2)} + i_{d0i}\right) - \cos\delta_{0i}\left(F_{3i(1,2)} - i_{q0i}\right) \tag{A.84}$$

$$C_{Mi(2,3)} = F_{3i(2,3)}\operatorname{sen}\delta_{0i} - F_{3i(1,3)}\cos\delta_{0i} \tag{A.85}$$

$$C_{Mi(2,4)} = F_{3i(2,4)}\cos\delta_{0i} - F_{3i(1,4)}\cos\delta_{0i} \quad . \tag{A.86}$$

The auxiliary variables Y_{eq}, F_{3i}, F_{4i}, H_{1i} and H_{2i} are defined as

$$Y_{eqi(1,1)} = -r_a / \left(r_a{}^2 + x'_d x'_q\right) \tag{A.87}$$

$$Y_{eqi(1,2)} = -x'_q / \left(r_a{}^2 + x'_d x'_q\right) \tag{A.88}$$

$$Y_{eqi(2,1)} = x'_d / \left({r_a}^2 + x'_d x'_q \right) \tag{A.89}$$

$$Y_{eqi(2,2)} = -r_a / \left({r_a}^2 + x'_d x'_q \right) \tag{A.90}$$

$$F_{3i(1,2)} = Y_{eqi(1,1)} v_{q0i} - Y_{eqi(1,2)} v_{d0i} \tag{A.91}$$

$$F_{3i(1,3)} = Y_{eqi(1,2)} \tag{A.92}$$

$$F_{3i(1,4)} = Y_{eqi(1,1)} \tag{A.93}$$

$$F_{3i(2,2)} = Y_{eqi(2,1)} v_{q0i} - Y_{eqi(2,2)} v_{d0i} \tag{A.94}$$

$$F_{3i(2,3)} = Y_{eqi(2,2)} \tag{A.95}$$

$$F_{3i(2,4)} = Y_{eqi(2,1)} \tag{A.96}$$

$$F_{4i(1,1)} = -Y_{eq(1,2)} \cos \delta_{0i} - Y_{eqi(1,1)} \operatorname{sen} \delta_{0i} \tag{A.97}$$

$$F_{4i(1,2)} = Y_{eqi(1,1)} \cos \delta_{0i} - Y_{eqi(1,2)} \operatorname{sen} \delta_{0i} \tag{A.98}$$

$$F_{4i(2,1)} = -Y_{eqi(2,2)} \cos \delta_{0i} - Y_{eqi(2,1)} \operatorname{sen} \delta_{0i} \tag{A.99}$$

$$F_{4i(2,2)} = Y_{eqi(2,1)} \cos \delta_{0i} - Y_{eqi(2,2)} \operatorname{sen} \delta_{0i} \tag{A.100}$$

$$H_{1i(1,2)} = F_{3i(1,2)} \left(E'_{d0i} - i_{q0i} \left(x'_{di} - x'_{qi} \right) \right) + F_{3i(2,2)} \left(E'_{q0i} - i_{d0i} \left(x'_{di} - x'_{qi} \right) \right) \tag{A.101}$$

$$H_{1i(2,2)} = -F_{3i(1,2)} \left(r_{ai} v_{d0i} + v_{q0i} x'_{di} \right) / V_{t0} - F_{3i(2,2)} \left(r_{ai} v_{q0i} - v_{d0i} x'_{qi} \right) / V_{t0} \tag{A.102}$$

$$H_{1i(1,3)} = i_{q0i} + F_{3i(1,3)} \left(E'_{d0i} - i_{q0i} \left(x'_{di} - x'_{qi} \right) \right) + F_{3i(2,3)} \left(E'_{q0i} - i_{d0i} \left(x'_{di} - x'_{qi} \right) \right) \tag{A.103}$$

$$H_{1i(2,3)} = v_{q0i} / V_{t0} - F_{3i(1,3)} \left(r_{ai} v_{d0i} + v_{q0i} x'_{di} \right) / V_{t0} - F_{3i(2,3)} \left(r_{ai} v_{q0i} - v_{d0i} x'_{qi} \right) / V_{t0} \tag{A.104}$$

$$H_{1i(1,4)} = i_{doi} + F_{3i(1,4)} \left(E'_{d0i} - i_{q0i} \left(x'_{di} - x'_{qi} \right) \right) + F_{3i(2,4)} \left(E'_{q0i} - i_{d0i} \left(x'_{di} - x'_{qi} \right) \right) \tag{A.105}$$

$$H_{1i(2,4)} = v_{d0i} / V_{t0} - F_{3i(1,4)} \left(r_{ai} v_{d0i} + v_{q0i} x'_{di} \right) / V_{t0} - F_{3i(2,4)} \left(r_{ai} v_{q0i} - v_{d0i} x'_{qi} \right) / V_{t0} \tag{A.106}$$

$$H_{2i(1,1)} = F_{4i(1,1)} \left(E'_{d0i} - i_{q0i} \left(x'_{di} - x'_{qi} \right) \right) + F_{4i(2,1)} \left(E'_{qi} - i_{d0i} \left(x'_{di} - x'_{qi} \right) \right) \tag{A.107}$$

$$H_{2i(1,2)} = F_{4i(1,2)} \left(E'_{d0i} - i_{q0i} \left(x'_{di} - x'_{qi} \right) \right) + F_{4i(2,2)} \left(E'_{q0i} - i_{d0i} \left(x'_{di} - x'_{qi} \right) \right) \tag{A.108}$$

$$H_{2i(2,1)} = -F_{4i(1,1)} \left(r_{ai} v_{d0i} + v_{q0i} x'_{di} \right) / V_{t0} - F_{4i(2,1)} \left(r_a v_{q0i} - v_{d0i} x'_{qi} \right) / V_{t0} \tag{A.109}$$

$$H_{2i(2,2)} = -F_{4i(1,2)} \left(r_{ai} v_{d0i} + v_{q0i} x'_{di} \right) / V_{t0} - F_{4i(2,2)} \left(r_{ai} v_{q0i} - v_{d0i} x'_{qi} \right) / V_{t0} \ . \tag{A.110}$$

The state matrix $\boldsymbol{A_i^{G2}}$ of the (*n-m*) generators represented by the classical model and the matrix $\boldsymbol{C_i^{G2}}$ are defined as

$$\boldsymbol{A_i^{G2}} = \begin{bmatrix} -\dfrac{K_{Di}}{2H_i} & \dfrac{E'_{q0}\left(Y_{eqi(2,2)}v_{d0i} - Y_{eqi(2,1)}v_{q0i}\right)}{2H_i} \\ 0 & \omega_0 \end{bmatrix}_{2\times 2} \tag{A.111}$$

$$\boldsymbol{C_i^{G2}} = \left[\begin{array}{c|c} 0 & \begin{array}{l} \operatorname{sen}\delta_{0i}\left(F_{3i(1,2)} - i_{q0i}\right) \\ +\cos\delta_{0i}\left(F_{3i(2,2)} + i_{d0i}\right) \end{array} \\ \hdashline 0 & \begin{array}{l} \operatorname{sen}\delta_{0i}\left(F_{3i(2,2)} + i_{d0i}\right) \\ -\cos\delta_{0i}\left(F_{3i(1,2)} - i_{q0i}\right) \end{array} \end{array}\right]_{2\times 2} . \tag{A.112}$$

Matrices $\boldsymbol{A_i^{SVC}}$ and $\boldsymbol{C_i^{SVC}}$ linked to the SVC are computed as

$$\boldsymbol{A_i^{SVC}} = \begin{bmatrix} -\dfrac{1}{T_3} & 0 & 0 \\ \dfrac{T_4 - T_2}{T_4^2} & -\dfrac{1}{T_4} & 0 \\ \dfrac{T_2}{T_4 T_5} & \dfrac{1}{T_5} & -\dfrac{1}{T_5} \end{bmatrix}_{2\times 2} \tag{A.113}$$

$$\boldsymbol{C_i^{SVC}} = \begin{bmatrix} 0 & 0 & -V_{SVC0,Q} \\ 0 & 0 & V_{SVC0,D} \end{bmatrix}_{2\times 3} . \tag{A.114}$$

$\boldsymbol{B_D}$ and $\boldsymbol{Y_D}$ are block matrices composed of the $\boldsymbol{B_i}$ and $\boldsymbol{Y_i}$ associated with the incremental bus voltages of the individual devices:

$$\boldsymbol{B_D} = \begin{bmatrix} \boldsymbol{B_1^{G1}} \\ \vdots \\ \boldsymbol{B_m^{G1}} \\ \boldsymbol{B_{m+1}^{G2}} \\ \vdots \\ \boldsymbol{B_n^{G2}} \\ \boldsymbol{B_{n+1}^{SVC}} \end{bmatrix}_{(10m+2n-2m+3)\times(2)} \tag{A.115}$$

$$\boldsymbol{Y_D} = \begin{bmatrix} \boldsymbol{Y_1^{G1}} \\ \vdots \\ \boldsymbol{Y_m^{G1}} \\ \boldsymbol{Y_{m+1}^{G2}} \\ \vdots \\ \boldsymbol{Y_n^{G2}} \\ \boldsymbol{Y_n^{SVC}} \end{bmatrix}_{2(n+1)\times(2)} . \tag{A.116}$$

The matrices $\boldsymbol{B_i^{G1}}$ and $\boldsymbol{Y_i^{G1}}$ associated with the i^{th} synchronous machine equipped with the PSS system are defined by

$$\boldsymbol{B_i^{G1}} = \begin{bmatrix} -\dfrac{H_{2i(1,1)}}{2H_i} & -\dfrac{H_{2i(1,2)}}{2H_i} \\ 0 & 0 \\ -\dfrac{F_{4i(1,1)}\left(x_d - x'_d\right)}{T'_{d0i}} & -\dfrac{F_{4i(1,2)}\left(x_d - x'_d\right)}{T'_{d0i}} \\ \dfrac{F_{4i(2,1)}\left(x_q - x'_q\right)}{T'_{q0i}} & \dfrac{F_{4i(2,2)}\left(x_q - x'_q\right)}{T'_{q0i}} \\ \dfrac{H_{2i(2,1)}}{T_R} & \dfrac{H_{2i(2,2)}}{T_R} \\ 0 & 0 \\ 0 & 0 \\ 0 & 0 \\ 0 & 0 \\ 0 & 0 \end{bmatrix}_{10\times 2} \tag{A.117}$$

$$\boldsymbol{Y_i^{G1}} = \begin{bmatrix} -F_{4i(2,1)}\cos\delta_{0i} - F_{4i(1,1)}\,\text{sen}\,\delta_{0i} & -F_{4i(2,2)}\cos\delta_{0i} - F_{4i(1,2)}\,\text{sen}\,\delta_{0i} \\ F_{4i(1,1)}\cos\delta_{0i} - F_{4i(2,1)}\,\text{sen}\,\delta_{0i} & F_{4i(1,2)}\cos\delta_{0i} - F_{4i(2,2)}\,\text{sen}\,\delta_{0i} \end{bmatrix}_{2\times 2}. \quad \text{(A.118)}$$

The matrices $\boldsymbol{B_i^{G2}}$ and $\boldsymbol{Y_i^{G2}}$ linked with the generator represented by the classical model are computed as

$$\boldsymbol{B_i^{G2}} = \begin{bmatrix} \dfrac{\left(-Y_{eqi(2,2)}\cos\delta_{0i} - Y_{eqi(2,1)}\,\text{sen}\,\delta_{0i}\right)E'_{q0}}{2H_i} & \dfrac{\left(Y_{eqi(2,1)}\cos\delta_{0i} - Y_{eqi(2,2)}\,\text{sen}\,\delta_{0i}\right)E'_{q0}}{2H_i} \\ 0 & 0 \end{bmatrix}_{2\times 2} \quad \text{(A.119)}$$

$$\boldsymbol{Y_i^{G2}} = \begin{bmatrix} -F_{4i(2,1)}\cos\delta_{0i} - F_{4i(1,1)}\,\text{sen}\,\delta_{0i} & -F_{4i(2,2)}\cos\delta_{0i} - F_{4i(1,2)}\,\text{sen}\,\delta_{0i} \\ F_{4i(1,1)}\cos\delta_{0i} - F_{4i(2,1)}\,\text{sen}\,\delta_{0i} & F_{4i(1,2)}\cos\delta_{0i} - F_{4i(2,2)}\,\text{sen}\,\delta_{0i} \end{bmatrix}_{2\times 2}. \quad \text{(A.120)}$$

The matrices $\boldsymbol{B_i^{SVC}}$ and $\boldsymbol{Y_i^{SVC}}$ linked to the SVC are computed as

$$\boldsymbol{B_i^{SVC}} = \begin{bmatrix} \dfrac{\left(T_3 - T_1\right)K_{SVC}V_{SVC,D0}}{T_3^2 V_{SVC0}} & \dfrac{\left(T_3 - T_1\right)K_{SVC}V_{SVC,Q0}}{T_3^2 V_{SVC0}} \\ \dfrac{\left(T_4 - T_2\right)T_1 K_{SVC}V_{SVC,D0}}{T_4^2 T_3 V_{SVC0}} & \dfrac{\left(T_4 - T_2\right)T_1 K_{SVC}V_{SVC,Q0}}{T_4^2 T_3 V_{SVC0}} \\ \dfrac{T_1 T_2 K_{SVC}V_{SVC,D0}}{T_3 T_4 T_5 V_{SVC0}} & \dfrac{T_1 T_2 K_{SVC}V_{SVC,Q0}}{T_3 T_4 T_5 V_{SVC0}} \end{bmatrix}_{3\times 2} \quad \text{(A.121)}$$

$$\boldsymbol{Y_i^{SVC}} = \begin{bmatrix} 0 & -B_{SVC0} \\ B_{SVC0} & 0 \end{bmatrix}_{2\times 2}. \quad \text{(A.122)}$$

The input matrix of the system is defined as

$$\boldsymbol{B} = \begin{bmatrix} 0 \\ \vdots \\ \dfrac{(T_3 - T_1)K_{SVC}}{T_3^2} \\ \dfrac{(T_4 - T_2)T_1 K_{SVC}}{T_4^2 T_3} \\ \dfrac{T_1 T_2 K_{SVC}}{T_3 T_4 T_5} \end{bmatrix}_{(10m+2n-2m+3)\times(1)} . \tag{A.123}$$

Appendix B
Mathematical representation of synchronized measurements

B.1 Transmission lines

The transmission lines are represented by the π-model with parameters that correspond to the positive sequence equivalent circuit. A transmission line with a primitive series impedance $g + j\,b$ and total line charging susceptances $j\,2b$ is represented by the equivalent circuit shown in Figure B.1.

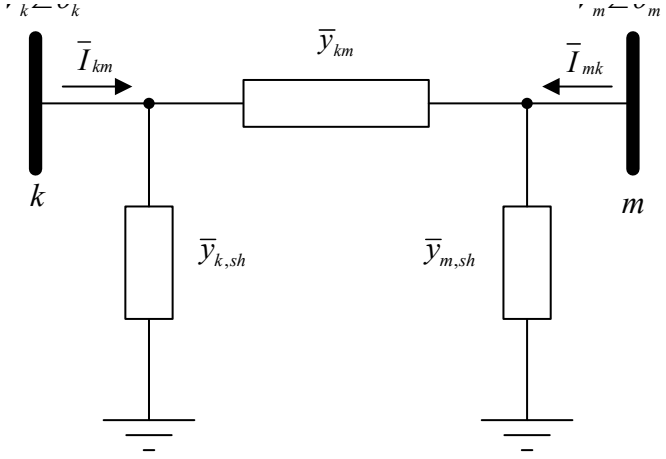

Figure B.1 Transmission line π-model

The current flowing from *k* to *m* is given by

$$\begin{aligned}\bar{I}_{km} &= \bar{V}_k \bar{y}_{k,sh} + \left(\bar{V}_k - \bar{V}_m\right)\bar{y}_{km} \\ &= \bar{V}_k \left(\bar{y}_{km} + \bar{y}_{k,sh}\right) - \bar{V}_m \bar{y}_{km}\end{aligned}, \tag{B.1}$$

where

$$\bar{y}_{km} = g_{km} + jb_{km} \tag{B.2}$$

$$\bar{y}_{k,sh} = g_{k,sh} + jb_{k,sh} \tag{B.3}$$

$$\bar{y}_{m,sh} = g_{m,sh} + jb_{m,sh}\,. \tag{B.4}$$

The rectangular components of the phasor associated with the branch current flowing from node *k* to node *m* can be derived as

$$\begin{aligned}I_{brach,r} &= V_k \left(\left(g_{km} + g_{k,sh}\right)\cos\theta_k - \left(b_{km} + b_{k,sh}\right)\sin\theta_k\right) \\ &\quad -V_m \left(g_{km}\cos\theta_m - b_{km}\sin\theta_m\right) \\ &= V_k \left(G_{kk}\cos\theta_k - B_{kk}\sin\theta_m\right) + V_m \left(G_{km}\cos\theta_m - B_{km}\sin\theta_m\right)\end{aligned} \tag{B.5}$$

$$\begin{aligned}I_{brach,i} &= V_k \left(\left(g_{km} + g_{k,sh}\right)\sin\theta_k + \left(b_{km} + b_{k,sh}\right)\cos\theta_k\right) \\ &\quad -V_m \left(g_{km}\sin\theta_m + b_{km}\cos\theta_m\right) \\ &= V_k \left(G_{kk}\sin\theta_k + B_{kk}\cos\theta_k\right) + V_m \left(G_{km}\sin\theta_m + B_{km}\cos\theta_m\right)\end{aligned}\,. \tag{B.6}$$

The Jacobian elements of the estimated current to be included in the matrix ***H*** are obtained as

$$\frac{\partial I_{brach,r}}{\partial \theta_k} = -V_k \left(G_{kk}\sin\theta_k + B_{kk}\cos\theta_k\right) \tag{B.7}$$

$$\frac{\partial I_{brach,r}}{\partial \theta_m} = -V_m \left(G_{km}\sin\theta_m + B_{km}\cos\theta_m\right) \tag{B.8}$$

$$V_k \frac{\partial I_{brach,r}}{\partial V_k} = V_k \left(G_{kk}\cos\theta_k - B_{kk}\sin\theta_k\right) \tag{B.9}$$

$$V_m \frac{\partial I_{brach,r}}{\partial V_m} = V_m \left(G_{km}\cos\theta_m - B_{km}\sin\theta_m\right) \tag{B.10}$$

$$\frac{\partial I_{brach,i}}{\partial \theta_k} = V_k \left(G_{kk} \cos\theta_k - B_{kk} \sin\theta_k \right) \tag{B.11}$$

$$\frac{\partial I_{brach,i}}{\partial \theta_m} = V_m \left(G_{km} \cos\theta_m - B_{km} \sin\theta_m \right) \tag{B.12}$$

$$V_k \frac{\partial I_{brach,i}}{\partial V_k} = V_k \left(G_{kk} \sin\theta_k + B_{kk} \cos\theta_k \right) \tag{B.13}$$

$$V_m \frac{\partial I_{brach,i}}{\partial V_m} = V_m \left(G_{km} \sin\theta_m + B_{km} \cos\theta_m \right). \tag{B.14}$$

B.2 Two winding transformer

The two-winding transformer is represented by the model reported in [78] and [79]. The physical representation of this component, as wells as its schematic equivalent circuit are shown in Figure B.2 (a) and in Figure B.2 (b). The magnetizing branch of the transformer, which under saturated conditions becomes nonlinear, is included in the model to account for the core losses.

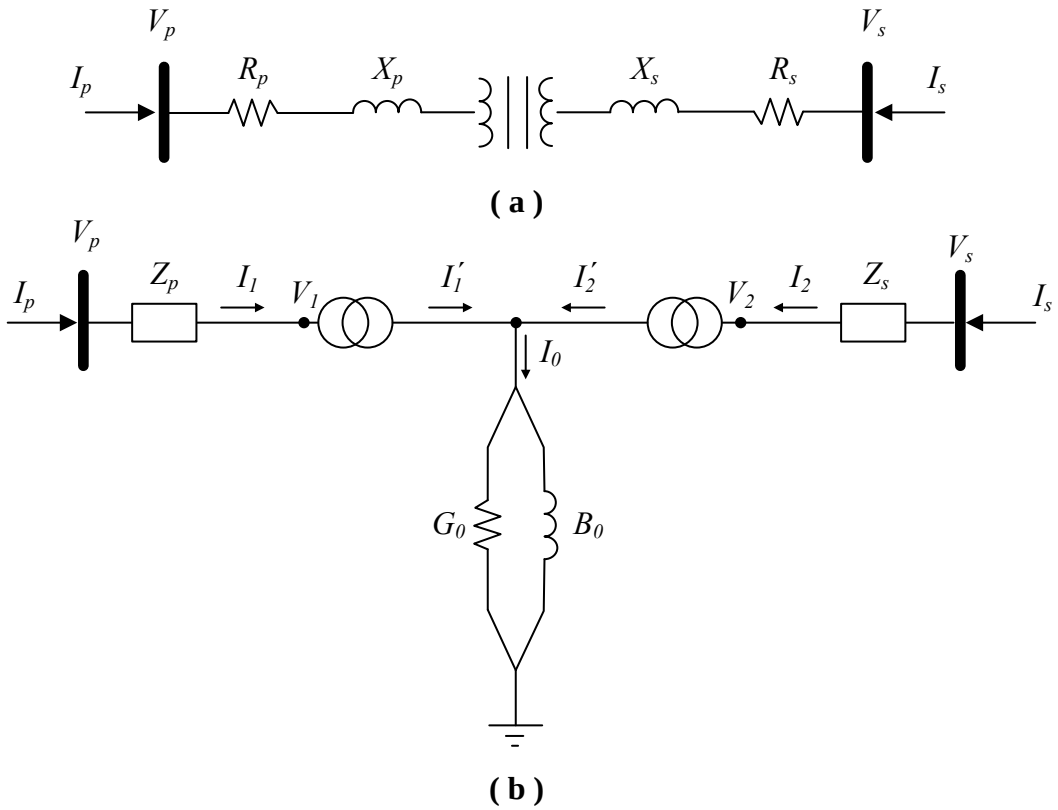

Figure B.2 Two-winding transformer [78]

The currents' injection can be written as

$$\begin{bmatrix} I_p \\ I_s \end{bmatrix} = \left(\begin{bmatrix} G_{pp} & G_{ps} \\ G_{sp} & G_{ss} \end{bmatrix} + j \begin{bmatrix} B_{pp} & B_{ps} \\ B_{sp} & B_{ss} \end{bmatrix} \right) \begin{bmatrix} V_p \\ V_s \end{bmatrix}, \tag{B.15}$$

where

$$G_{pp} = \frac{F_1 \left(U_v^2 + R_1 \right) + F_2 R_2}{A_2} \tag{B.16}$$

$$B_{pp} = \frac{F_1 R_2 - F_2 \left(U_v^2 + R_1 \right)}{A_2} \tag{B.17}$$

$$G_{ss} = \frac{F_1 \left(T_v^2 + R_3 \right) + F_2 R_4}{A_2} \tag{B.18}$$

$$B_{ss} = \frac{F_1 R_4 - F_2 \left(T_v^2 + R_3 \right)}{A_2} \tag{B.19}$$

$$G_{ps} = \frac{-T_v U_v \left(F_1 \cos\phi_1 + F_2 \sin\phi_1 \right)}{A_2} \tag{B.20}$$

$$B_{ps} = \frac{T_v U_v \left(F_2 \cos\phi_1 - F_1 \sin\phi_1 \right)}{A_2} \tag{B.21}$$

$$G_{sp} = \frac{-T_v U_v \left(F_1 \cos\phi_2 + F_2 \sin\phi_2 \right)}{A_2} \tag{B.22}$$

$$B_{sp} = \frac{T_v U_v \left(F_2 \cos\phi_2 - F_1 \sin\phi_2 \right)}{A_2} \tag{B.23}$$

$$F_1 = T_v^2 R_s + U_v^2 R_p + R_{eq} \tag{B.24}$$

$$F_2 = T_v^2 X_s + U_v^2 X_p + X_{eq} \tag{B.25}$$

$$A_2 = F_1^2 + F_2^2 \tag{B.26}$$

$$R_{eq} = \left(R_p R_s - X_p X_s \right) G_0 - \left(R_p X_s - R_s X_p \right) B_0 \tag{B.27}$$

$$X_{eq} = \left(R_p R_s - X_p X_s \right) B_0 + \left(R_p X_s - R_s X_p \right) G_0 \tag{B.28}$$

$$R_1 = R_s G_0 - X_s B_0 \tag{B.29}$$

$$R_2 = R_s B_0 + X_s G_0 \tag{B.30}$$

$$R_3 = R_p G_0 - X_p B_0 \tag{B.31}$$

$$R_4 = R_p B_0 + X_p G_0 \tag{B.32}$$

$$\phi_1 = \phi_{tv} - \phi_{uv} \tag{B.33}$$

$$\phi_2 = \phi_{uv} - \phi_{tv} . \tag{B.34}$$

The rectangular components of current flow may be derived as

$$I_{ps,r} = V_p \left(G_{pp} \cos\theta_p - B_{pp} \sin\theta_p \right) + V_s \left(G_{ps} \cos\theta_s - B_{ps} \sin\theta_s \right) \tag{B.35}$$

$$I_{ps,i} = V_p \left(G_{pp} \sin\theta_p + B_{pp} \cos\theta_p \right) + V_s \left(G_{ps} \sin\theta_s + B_{ps} \cos\theta_s \right) \tag{B.36}$$

$$I_{sp,r} = V_s\left(G_{ss}\cos\theta_s - B_{ss}\sin\theta_s\right) + V_p\left(G_{sp}\sin\theta_p - B_{sp}\cos\theta_p\right) \tag{B.37}$$

$$I_{sp,i} = V_s\left(G_{ss}\sin\theta_s + B_{ss}\cos\theta_s\right) + V_p\left(G_{sp}\sin\theta_p + B_{sp}\cos\theta_p\right). \tag{B.38}$$

The partial derivatives of current flow equations from *p* to *s* with respect to voltage phase and magnitude are

$$\frac{\partial I_{ps,r}}{\partial\theta_p} = -V_p\left(G_{pp}\sin\theta_p + B_{pp}\cos\theta_p\right) \tag{B.39}$$

$$\frac{\partial I_{ps,r}}{\partial\theta_s} = -V_s\left(G_{ps}\sin\theta_s + B_{ps}\cos\theta_s\right) \tag{B.40}$$

$$\frac{\partial I_{ps,r}}{\partial V_p} = G_{pp}\cos\theta_p - B_{pp}\sin\theta_p \tag{B.41}$$

$$\frac{\partial I_{ps,r}}{\partial V_s} = G_{ps}\cos\theta_s - B_{ps}\sin\theta_s \tag{B.42}$$

$$\frac{\partial I_{ps,i}}{\partial\theta_p} = V_p\left(G_{pp}\cos\theta_p - B_{pp}\sin\theta_p\right) \tag{B.43}$$

$$\frac{\partial I_{ps,i}}{\partial\theta_s} = V_s\left(G_{ps}\cos\theta_s - B_{ps}\sin\theta_s\right) \tag{B.44}$$

$$\frac{\partial I_{ps,i}}{\partial V_p} = G_{pp}\sin\theta_p + B_{pp}\cos\theta_p \tag{B.45}$$

$$\frac{\partial I_{ps,i}}{\partial V_s} = G_{ps}\sin\theta_s + B_{ps}\cos\theta_s. \tag{B.46}$$

The partial derivatives of current flow equations from *s* to *p* with respect to voltage phase and magnitude are

$$\frac{\partial I_{sp,r}}{\partial\theta_p} = V_p\left(-G_{sp}\sin\theta_p - B_{sp}\cos\theta_p\right) \tag{B.47}$$

$$\frac{\partial I_{sp,r}}{\partial\theta_s} = V_s\left(G_{ss}\sin\theta_s - B_{ss}\cos\theta_s\right) \tag{B.48}$$

$$\frac{\partial I_{sp,r}}{\partial V_p} = G_{sp}\cos\theta_p - B_{sp}\sin\theta_p \tag{B.49}$$

$$\frac{\partial I_{sp,r}}{\partial V_s} = G_{ss}\cos\theta_s - B_{ss}\sin\theta_s \tag{B.50}$$

$$\frac{\partial I_{sp,i}}{\partial \theta_p} = V_p\left(G_{sp}\cos\theta_p - B_{sp}\sin\theta_p\right) \tag{B.51}$$

$$\frac{\partial I_{sp,i}}{\partial \theta_s} = V_s\left(G_{ss}\cos\theta_s - B_{ss}\sin\theta_s\right) \tag{B.52}$$

$$\frac{\partial I_{sp,i}}{\partial V_p} = G_{sp}\sin\theta_p + B_{sp}\cos\theta_p \tag{B.53}$$

$$\frac{\partial I_{sp,i}}{\partial V_s} = G_{ss}\sin\theta_s + B_{ss}\cos\theta_s\,. \tag{B.54}$$

Bibliography

[1] M. A. Pai, D. P. Sen Gupta, and K. R. Padiyar, *Small Signal Analysis of Power Systems*. Harrow, U.K.: Alpha Science International. Narosa series in power and energy systems, 2004.

[2] D. N. Kosterev, C. W. Taylor, and W. A. Mittelstadt, "Model validation for the August 10, 1996 WSCC system outage," *IEEE Trans. Power Syst.*, vol. 14, no. 3, pp. 967–979, 1999.

[3] G. Rogers, *Power System Oscillations*. Boston, MA: Springer USA, 2000.

[4] CIGRE, "Analysis and Control of Power System Oscillations." Task Force 07 of Advisory Group 01 of Study Committee 38, Final Report, 1996.

[5] A. R. Messina, *Inter-area oscillations in power systems : a nonlinear and nonstationary perspective*. Springer, 2009.

[6] D. Molina, G. K. Venayagamoorthy, J. Liang, and R. G. Harley, "Intelligent Local Area Signals Based Damping of Power System Oscillations Using Virtual Generators and Approximate Dynamic Programming," *IEEE Trans. Smart Grid*, vol. 4, no. 1, pp. 498–508, Mar. 2013.

[7] M. Garmroodi, D. J. Hill, J. Ma, and G. Verbic, "Impact of wind generation variability on small signal stability of power systems," in *2014 Australasian Universities Power Engineering Conference (AUPEC)*, 2014, pp. 1–6.

[8] B. C. Pal and B. Chaudhuri, *Robust control in power systems*. Springer Science+Business Media, Inc, 2010.

[9] J. H. Chow, J. J. Sanchez-Gasca, H. Ren, and S. Wang, "Power system damping controller design-using multiple input signals," *IEEE Control Syst. Mag.*, vol. 20, no. 4, pp. 82–90, 2000.

[10] B. Naduvathuparambil, M. C. Valenti, and A. Feliachi, "Communication delays in wide area measurement systems," in *Proceedings of the Thirty-Fourth Southeastern Symposium on System Theory (Cat. No.02EX540)*, 2002, pp. 118–122.

[11] M. S. Almas and L. Vanfretti, "Impact of time-synchronization signal loss on PMU-

based WAMPAC applications," in *2016 IEEE Power and Energy Society General Meeting (PESGM)*, 2016, pp. 1–5.

[12] J. Quintero and V. Venkatasubramanian, "A Real-Time Wide-Area Control Framework for Mitigating Small-Signal Instability in Large Electric Power Systems," in *Proceedings of the 38th Annual Hawaii International Conference on System Sciences*, 2005, pp. 1–10.

[13] M. R. A. Paternina, J. M. Ramirez, and A. Z. Méndez, "Real-time implementation of the digital Taylor–Fourier transform for identifying low frequency oscillations," *Electr. Power Syst. Res.*, vol. 140, pp. 846–853, Nov. 2016.

[14] I. L. Ortega-Rivera, C. R. Fuerte-Esquivel, C. Angeles Camacho, G. T. Heydt, and V. Vittal, "A dynamic state estimator for the development of a control signal for power system damping enhancement," in *2017 IEEE Power & Energy Society Innovative Smart Grid Technologies Conference (ISGT)*, 2017, pp. 1–5.

[15] E. Ghahremani and I. Kamwa, "Local and Wide-Area PMU-Based Decentralized Dynamic State Estimation in Multi-Machine Power Systems," *IEEE Trans. Power Syst.*, vol. 31, no. 1, pp. 547–562, Jan. 2016.

[16] A. K. Singh and B. C. Pal, "Decentralized Control of Oscillatory Dynamics in Power Systems Using an Extended LQR," *IEEE Trans. Power Syst.*, vol. 31, no. 3, pp. 1715–1728, May 2016.

[17] E. Handschin, N. Schnurr, and W. H. Wellssow, "Damping potential of FACTS devices in the European power system," in *IEEE Power Engineering Society General Meeting (IEEE Cat. No.03CH37491)*, 2003, pp. 2355–2360.

[18] R. Mohan Mathur and R. K. Varma, "Thyristor-based FACTS Controllers for Electrical Transmission Systems," *IEEE Series on Power Engineering*. US, 2002.

[19] E. Acha, C. R. Fuerte-Esquivel, H. Ambriz-Pérez, and C. Angeles-Camacho, *FACTS: Modelling and Simulation in Power Networks*. Chichester, UK: John Wiley & Sons, Ltd, 2004.

[20] F. Aboytes, G. Arroyo, and G. Villa, "Application of Static Var Compensators in Longitudinal Power Systems," *IEEE Trans. Power Appar. Syst.*, vol. PAS-102, no. 10, pp. 3460–3466, Oct. 1983.

[21] N. Mithulananthan, C. A. Cañizares, and J. Reeve, "Hopf bifurcation control in power system using power system stabilizers and static var compensator," in *Proc. North American Power Symposium*, 1999, pp. 155 – 163.

[22] K. Meub, "Pioneering smart grid technology solves decades old problematic power grid phenomenon," *Sandia Lab News, Sandia National Laboratories*, vol. 1, no. 1. Sandia National Laboratories, pp. 9–9, 2018.

[23] B. Pierre *et al.*, "Supervisory system for a wide area damping controller using PDCI modulation and real-time PMU feedback," in *2016 IEEE Power and Energy Society General Meeting (PESGM)*, 2016, pp. 1–5.

[24] S. Zhang and V. Vittal, "Design of Wide-Area Power System Damping Controllers Resilient to Communication Failures," *IEEE Trans. Power Syst.*, vol. 28, no. 4, pp. 4292–4300, Nov. 2013.

[25] P. Kundur, "Power system stability and control," *McGraw-Hill*. pp. 45–138, 1994.

[26] "Definition and Classification of Power System Stability IEEE/CIGRE Joint Task Force on Stability Terms and Definitions," *IEEE Trans. Power Syst.*, vol. 19, no. 3, pp. 1387–1401, Aug. 2004.

[27] N. Martins, *Impact of interactions among power system controls*. CIGRE Special Publication 38.02.16. Technical Brochure 166, 2000.

[28] I. Report, "Excitation System Models for Power System Stability Studies," *IEEE Trans. Power Appar. Syst.*, vol. PAS-100, no. 2, pp. 494–509, Feb. 1981.

[29] I. S. 421.5-2005, *IEEE recommended practice for excitation system models for power system stability studies*. New York: Institute of Electrical and Electronic Engineers, Inc., 2005.

[30] Powertech, *Transient Stability Analysis Tool (TSAT) User Manual*. Powertech Labs. Surrey, BC, Canada, 2015.

[31] V. Vittal, "Transient stability test systems for direct stability methods," *IEEE Trans. Power Syst.*, vol. 7, no. 1, pp. 37–43, 1992.

[32] S. Zhang and V. Vittal, "Wide-Area Control Resiliency Using Redundant Communication Paths," *IEEE Trans. Power Syst.*, vol. 29, no. 5, pp. 2189–2199, Sep. 2014.

[33] S. Zhang, "Improved power grid resiliency through interactive system control," Ph.D. dissertation, Arizona State Univ., Tempe, AZ, 2014.

[34] Powertech, *Small Signal Analysis Tool (SSAT) User Manual*. Powertech Labs. Surrey, BC, Canada, 2015.

[35] B. Gao, G. K. Morison, and P. Kundur, "Voltage stability evaluation using modal analysis," *IEEE Trans. Power Syst.*, vol. 7, no. 4, pp. 1529–1542, 1992.

[36] Y. Zhang, "Design of wide-area damping control systems for power system low-frequency inter-area oscillations," Ph.D. Dissertation, Washington State University, 2007.

[37] E. V. Larsen and J. H. Chow, "SVC control design concepts for system dynamic

performance," in *IEEE Tutorial Course: Application of SVS for System Dynamic Performance*, 1987, pp. 36–53.

[38] Y. Chompoobutrgool, L. Vanfretti, and M. Ghandhari, "Survey on power system stabilizers control and their prospective applications for power system damping using Synchrophasor-based wide-area systems," *Eur. Trans. Electr. Power*, vol. 21, no. 8, pp. 2098–2111, 2011.

[39] B. Chaudhuri and B. C. Pal, "Robust Damping of Multiple Swing Modes Employing Global Stabilizing Signals With a TCSC," *IEEE Trans. Power Syst.*, vol. 19, no. 1, pp. 499–506, Feb. 2004.

[40] L. D. Philipp, A. Mahmood, and B. L. Philipp, "An improved refinable rational approximation to the ideal time delay," *IEEE Trans. Circuits Syst. I Fundam. Theory Appl.*, vol. 46, no. 5, pp. 637–640, May 1999.

[41] H. Chen, L. Zhang, J. Mo, and K. E. Martin, "Synchrophasor-based real-time state estimation and situational awareness system for power system operation," *J. Mod. Power Syst. Clean Energy*, vol. 4, no. 3, pp. 370–382, Jul. 2016.

[42] S. C. Savulescu, *Real-Time Stability Assessment in Modern Power System Control Centers*. IEEE Press Wiley, 2009.

[43] A. G. mez Expósito, A. J. Conejo, and C. Cañizares, *Electric energy systems : analysis and operation*. CRC Press, 2009.

[44] E. Al-Shaer and M. A. Rahman, *Security and Resiliency Analytics for Smart Grids*, vol. 67. Cham: Springer International Publishing, 2016.

[45] M. Asprou, S. Chakrabarti, and E. Kyriakides, "A Two-Stage State Estimator for Dynamic Monitoring of Power Systems," *IEEE Syst. J.*, vol. 11, no. 3, pp. 1767–1776, Sep. 2017.

[46] M. K. Celik and A. Abur, "A robust WLAV state estimator using transformations," *IEEE Trans. Power Syst.*, vol. 7, no. 1, pp. 106–113, 1992.

[47] G. N. Korres and N. M. Manousakis, "State estimation and bad data processing for systems including PMU and SCADA measurements," *Electr. Power Syst. Res.*, vol. 81, no. 7, pp. 1514–1524, Jul. 2011.

[48] V. Murugesan, Y. Chakhchoukh, V. Vittal, G. T. Heydt, N. Logic, and S. Sturgill, "PMU Data Buffering for Power System State Estimators," *IEEE Power Energy Technol. Syst. J.*, vol. 2, no. 3, pp. 94–102, Sep. 2015.

[49] B. A. Alcaide-Moreno, C. R. Fuerte-Esquivel, M. Glavic, and T. Van Cutsem, "Electric Power Network State Tracking From Multirate Measurements," *IEEE Trans. Instrum. Meas.*, vol. 67, no. 1, pp. 33–44, Jan. 2018.

[50] M. Glavic and T. Van Cutsem, “Reconstructing and tracking network state from a limited number of synchrophasor measurements,” *IEEE Trans. Power Syst.*, vol. 28, no. 2, pp. 1921–1929, May 2013.

[51] A. Debs and R. Larson, “A Dynamic Estimator for Tracking the State of a Power System,” *IEEE Trans. Power Appar. Syst.*, vol. PAS-89, no. 7, pp. 1670–1678, Sep. 1970.

[52] A. M. Leite da Silva, M. B. Do Coutto Filho, and J. F. De Queiroz, “State forecasting in electric power systems,” *IEE Proc. Gener. Transm. Distrib.*, vol. 130, no. 5, pp. 237–244, 1983.

[53] G. Valverde and V. Terzija, “Unscented Kalman filter for power system dynamic state estimation,” *IET Gener. Transm. Distrib.*, vol. 5, no. 1, p. 29, 2011.

[54] A. Abur and A. Gómez Expósito, *Power system state estimation : theory and implementation*. Marcel Dekker, 2004.

[55] H. Karimipour and V. Dinavahi, “Extended Kalman Filter-Based Parallel Dynamic State Estimation,” *IEEE Trans. Smart Grid*, vol. 6, no. 3, pp. 1539–1549, May 2015.

[56] A. G. Phadke and B. Kasztenny, “Synchronized Phasor and Frequency Measurement Under Transient Conditions,” *IEEE Trans. Power Deliv.*, vol. 24, no. 1, pp. 89–95, Jan. 2009.

[57] S. Chakrabarti, E. Kyriakides, Tianshu Bi, Deyu Cai, and V. Terzija, “Measurements get together,” *IEEE Power Energy Mag.*, vol. 7, no. 1, pp. 41–49, Jan. 2009.

[58] D. Simon, *Optimal state estimation : Kalman, H [infinity] and nonlinear approaches*. Wiley-Interscience, 2006.

[59] A. Monticelli, *State estimation in electric power systems : a generalized approach*. Kluwer Academic Publishers, 1999.

[60] A. Monticelli, “Electric power system state estimation,” *Proc. IEEE*, vol. 88, no. 2, pp. 262–282, Feb. 2000.

[61] Liuxi Zhang and A. Abur, “Impact of tuning on bad data detection of PMU measurements,” in *IEEE PES Innovative Smart Grid Technologies*, 2012, pp. 1–5.

[62] S. Wang, J. Zhao, Z. Huang, and R. Diao, “Assessing Gaussian Assumption of PMU Measurement Error Using Field Data,” *IEEE Trans. Power Deliv.*, pp. 1–1, 2017.

[63] K. Nishiya, J. Hasegawa, and T. Koike, “Dynamic state estimation including anomaly detection and identification for power systems,” *IEE Proc. Gener. Transm. Distrib.*, vol. 129, no. 5, pp. 192–198, 1982.

[64] P. Rousseaux, T. Van Cutsem, and T. E. Dy Liacco, “Whither dynamic state

estimation?," *Int. J. Electr. Power Energy Syst.*, vol. 12, no. 2, pp. 104–116, Apr. 1990.

[65] M. Brown Do Coutto Filho and J. C. S. de Souza, "Forecasting-Aided State Estimation—Part I: Panorama," *IEEE Trans. Power Syst.*, vol. 24, no. 4, pp. 1667–1677, Nov. 2009.

[66] A. Jain and N. R. Shivakumar, "Power system tracking and dynamic state estimation," in *2009 IEEE/PES Power Systems Conference and Exposition*, 2009, pp. 1–8.

[67] Jaewon Chang, G. N. Taranto, and J. H. Chow, "Dynamic state estimation in power system using a gain-scheduled nonlinear observer," in *Proceedings of International Conference on Control Applications*, pp. 221–226.

[68] A. Farzanehrafat and N. R. Watson, "Review of power quality state estimation," in *20th Australasian Universities Power Engineering Conference (AU- PEC)*, 2010.

[69] J. Qi, K. Sun, J. Wang, and H. Liu, "Dynamic State Estimation for Multi-Machine Power System by Unscented Kalman Filter With Enhanced Numerical Stability," *IEEE Trans. Smart Grid*, vol. 9, no. 2, pp. 1184–1196, Mar. 2018.

[70] A. K. Singh and B. C. Pal, "Decentralized Dynamic State Estimation in Power Systems Using Unscented Transformation," *IEEE Trans. Power Syst.*, vol. 29, no. 2, pp. 794–804, Mar. 2014.

[71] L. Zhang, A. Bose, A. Jampala, V. Madani, and J. Giri, "Design, Testing, and Implementation of a Linear State Estimator in a Real Power System," *IEEE Trans. Smart Grid*, vol. 8, no. 4, pp. 1782–1789, Jul. 2017.

[72] A. G. Phadke and J. S. Thorp, *Synchronized Phasor Measurements and their Applications*. New York: Springer, 2008.

[73] Powertech, *User-defined Model Manual for Transient Security Assessement Tool*. Powertech Labs. Surrey, BC, Canada, 2015.

[74] A. Román Messina and M. A. Avila Rosales, "Analysis of inter-area damping enhancement by static var compensators in longitudinal power systems," *Control Eng. Pract.*, vol. 5, no. 1, pp. 117–122, Jan. 1997.

[75] R. Castellanos B., J. G. Calderón G., D. Olguin S., H. Sarmiento U., and A. R. Messina, "Use of power system stabilizers for damping inter-area oscillations in the south systems of the Mexican electrical grid," *Electr. Power Syst. Res.*, vol. 76, no. 4, pp. 169–179, Jan. 2006.

[76] P. W. Sauer and M. A. Pai, *Power System Dynamics and Stability*. Prentice Hall, 1998.

[77] Z. Dong and P. Zhang, *Emerging Techniques in Power System Analysis*. Berlin, Heidelberg: Springer Berlin Heidelberg, 2010.

[78] B. A. Alcaide-Moreno, “State estimation of electric power systems using SCADA and PMU measurements,” Ph.D. dissertation, Universidad Michoacana de San Nicolás de Hidalgo, Morelia, Michoacan, México, 2016.

[79] C. R. Fuerte-Esquivel, E. Acha, S. G. Tan, and J. J. Rico, “Efficient object oriented power systems software for the analysis of large-scale networks containing FACTS-controlled branches,” *IEEE Trans. Power Syst.*, vol. 13, no. 2, pp. 464–472, May 1998.